1990

Prediction of steady and unsteady flow and heat transfer over a cylinder in crossflow using a space-time marching algorithm

Brett William Batson
Iowa State University

Order Number 9100478

Prediction of steady and unsteady flow and heat transfer over a cylinder in crossflow using a space-time marching algorithm

Batson, Brett William, Ph.D.

Iowa State University, 1990

U·M·I
300 N. Zeeb Rd.
Ann Arbor, MI 48106

Prediction of steady and unsteady flow and heat transfer over a cylinder in crossflow using a space-time marching algorithm

by

Brett William Batson

A Dissertation Submitted to the
Graduate Faculty in Partial Fulfillment of the
Requirements for the Degree of
DOCTOR OF PHILOSOPHY

Major: Mechanical Engineering

Approved:

Signature was redacted for privacy.

In Charge of Major Work

Signature was redacted for privacy.

For the Major Department

Signature was redacted for privacy.

For the Graduate College

Iowa State University
Ames, Iowa
1990

TABLE OF CONTENTS

LIST OF TABLES

LIST OF FIGURES

ACKNOWLEDGEMENTS

This project was supported by NASA through the Lewis Research Center in Cleveland, Ohio, grant number NGT 16-002-802. I would like to thank all of those there who assisted me in any way in this work.

Thanks go to Dr. Richard H. Pletcher, my major professor, for his time and assistance. To the other members of my graduate committee, Dr. Theodore H. Okiishi, Dr. Bruce R. Munson, Dr. Joseph M. Prusa, and Dr. Robert J. Lambert, I owe a debt of gratitude. Although Dr. Cook was not officially a member of my committee, I would like to thank him for substituting for another member during my final defence. All of the above have become friends, more than committee members.

I extend special thanks to the other graduate students in the CFD group. I appreciate their help and support greatly.

Finally, I wish to express my deepest gratitude to my family for their support, love, understanding and, especially, for their patience.

NOMENCLATURE

Roman Symbols

a	Coefficients on viscous terms
A	Coefficients on viscous terms
b	Backward difference weight factor for the hybrid terms
c	Accoustic velocity
C	Coefficients on transverse flux terms
C	Coefficients used in pressure Poisson backsweep
c_p	Specific heat at constant pressure
C_f	Skin-friction coefficient
C_p	Pressure coefficient; $\left(\frac{p-p_r}{\frac{1}{2}\rho_r u_r^2}\right)$
C_1, C_2	Sutherland coefficients
e	Internal energy
$\overline{E}$, $\overline{F}$	Flux vectors
E_t	Total energy per unit volume
f	Forward difference weight factor for the hybrid terms
h	Enthalpy
J	Determinant of the Jacobian matrix
k	Thermal conductivity
L	Reference length
M	Mach number; $\left(\frac{u_r}{c_r}\right)$
n	Frequency
Nu	Nusselt number; $\left(\frac{\partial T}{\partial y}\right)$
p	Pressure
p^+	Pressure correction
$\overline{p}$	Pressure resulting from the Poisson solution

Pr	Prandtl number; $\left(\frac{\mu c_p}{k}\right)$
$\bar{q}$	Vector of unknowns
Q	Heat flux
r	Radius
R	Ideal gas constant
Re	Reynolds number; $\left(\frac{\rho_r u_r L_R}{\mu_r}\right)$
S	Thermal variable; $\left(\frac{T-T_{surf}}{T_r-T_{surf}}\right)$
S_p	Source term in the pressure Poisson equation
St	Stanton number; $\left(\frac{Nu}{PrRe}\right)$
t	Time
T	Temperature
u	x component of velocity
U	ξ direction contravariant velocity
v	y component of velocity
V	η direction contravariant velocity
x	First coordinate direction
y	Second coordinate direction

Greek Symbols

α	Multiplier in pressure Poisson equation
γ	Ratio of specific heats
Γ	Thermal variable used in Blasius problem
δ	Error in pressure compared to the converged pressure
δ	Central difference operator
Δ	Incremental change
Δ	First derivative forward difference operator
ϵ	Pressure error used in Poisson solver
η	Transformed coordinate
θ	Angle, in degrees, around cylinder measured from front stagnation point
Θ	$c_p S + \frac{u^2+v^2}{2(T_r-T_{surf})}$
λ	Coefficient on thermal diffusion terms

Λ	Coefficient on thermal diffusion terms
μ	Viscosity
ξ	Transformed coordinate
ρ	Density
τ	Viscous stress tensor
τ_w	Wall shear stress
Φ	Viscous dissipation
ω	Relaxation parameter used in pressure Poisson step
ω	Vorticity (using dimensionless variables); $\left(-\frac{\partial u}{\partial y}+\frac{\partial v}{\partial x}\right)$

Subscripts

d	Based on diameter
e	East
max	Maximum
min	Minimum
n	North
r	Free stream
R	Reference
s	South
$surf$	Body surface
t	Total
w	West
x	Based on distance, x
x	Partial derivative with respect to x
y	Partial derivative with respect to y
ξ	Partial derivative with respect to ξ
η	Partial derivative with respect to η

Superscripts

c	Cross
m	Global sweep iteration count

s	Streamwise
t	Transverse
T	Transpose
$\tilde{}$	Dimensional
$\hat{}$	Updated through Newton iterations
∞	Converged

CHAPTER 1. INTRODUCTION

Problem Statement

Many fluid flows occurring in engineering applications and nature are very complex. Some flows are also complicated by the addition of heat transfer. Despite the complexity, it is important that engineers gain an understanding of these flows.

A vast array of products presently designed by engineers involve or include the flow of fluids or heat transfer, or both. Airplanes, automobiles, bicycles, engines, heat exchangers, refrigerators, and turbines are a few such products. In order to improve existing designs of any of these, or to develop new ones, it is necessary to gain a better understanding of the fluid mechanics and heat transfer associated with these applications.

Fluid flow is described mathematically by the laws of conservation of momentum, mass, and energy. These laws have been understood for some time. However, the complicated nature of the equations and boundary conditions limits analytical solutions to simplified sets of these equations over simple geometries. With the advent of the electronic digital computer, solutions of the full set of equations over complicated geometries have become possible.

The solution of the governing equations on a digital computer is accomplished by approximating them with sets of discrete equations. These equations are then solved

on a sufficient number of points within the domain of interest to adequately resolve the details of the flow. Several factors should be considered when choosing the exact form of these discrete equations and the procedure used to solve them. Among them are accuracy, robustness, and computational efficiency. Simplifying assumptions are judged for their validity in the flow regime considered. One of the more important aspects of the overall scheme is the application of boundary conditions. These should be kept as simple and accurate as possible.

Often the equations which are discretized are a set of nonlinear partial differential equations. The equations which govern the flow of a Newtonian fluid are called, collectively, the Navier-Stokes equations (Anderson et al. 1984). The character of these equations varies with the particular flow regime considered. They are a mixed set of hyperbolic-parabolic equations for unsteady, compressible flow, and parabolic-elliptic for unsteady, incompressible flow. For steady flow they are hyperbolic at supersonic speeds, parabolic at the sonic point, and elliptic at subsonic speeds.

Various methods have been proposed to numerically solve the Navier-Stokes equations. Although most have strong points, it is not clear which of the algorithms is superior. There remains sufficient motivation for the development and refinement of advanced methods of solution — including new methods deviating radically from the usual ones such as finite-difference, finite element, and spectral methods.

The present work deals with a procedure employing iterative, spatial sweeps. Solvers of this type are called space-marching methods. Such methods have proven to be efficient and accurate for steady flows. The intent of this study has been to extend the range of applicability of this procedure to unsteady flows with heat transfer. Since this extension involves marching in both space and time, confusion

due to terminology can occur. An effort has been made to avoid the use of the word 'marching' without modifiers. For the space marching procedure, the term, 'space' is used to clarify the meaning. The modifiers, 'time' or 'temporal' are used to denote the procedure of advancing the temporal solution.

Below is a brief overview of work which has been performed by other researchers on various space-marching algorithms. Following that are a few comments on the present procedure. Since the bulk of the calculations for this project were for flow over a right-circular cylinder, a review of work done in that arena is provided. Lastly, a brief discussion of the motivation for this project is given.

Review of Previous Work on Space-Marching Methods

The first space-marching schemes utilized the boundary-layer equations. These equations are strictly parabolic, and thus are solved using one pass. Some limitations of this procedure are the lack of streamwise diffusion, transverse pressure gradients, and the inability to calculate streamwise pressure gradients in external flows.

To overcome some of the shortcomings of the boundary-layer equations, the parabolized Navier-Stokes (PNS) equations are sometimes applied (see e.g., Patankar and Spalding 1972). This method is a once-through procedure for solution of problems that may include transverse pressure gradients and secondary flows. The parabolization of the Navier-Stokes equations is accomplished by dropping the streamwise diffusion terms, evaluating streamwise convective terms using only upstream information, and, for subsonic flows, the streamwise pressure gradient is imposed as a fixed source term.

The next level of complexity for subsonic flows are simplified forms of the gov-

erning equations which include some elliptic information. These are referred to as 'reduced' by Rubin and Reddy (1983) and partially-parabolized Navier-Stokes equations (PPNS) (Anderson et al. 1984). Multiple passes are required to resolve the elliptic effect. In these equations, some of the diffusion terms are neglected. More details of the dropped terms are given below.

A few researchers have included the full set of Navier-Stokes equations, using multiple passes to compute both the streamwise pressure gradient and the streamwise diffusion terms.

Simplified forms of the Navier-Stokes equations

The reduced Navier-Stokes and partially parabolized Navier-Stokes (PPNS) equations include those forms which neglect some streamwise influence. For this reason, both forms represent simplified or reduced versions of the equations. However, the term 'reduced' has been used in the literature (see e.g., Rubin and Reddy 1983) and will be used here to represent the set of equations in which the streamwise diffusion is dropped from the x-momentum equation, and all diffusion is eliminated from the y- and z-momentum equations. The PPNS equations, on the other hand, are characterized by only the lack of streamwise diffusion in all momentum equations. The streamwise pressure gradient is computed in both of these. Multiple passes are required to resolve this term. These are, by far, the most common elliptic equations which have been space marched.

Segregated methods Methods which solve the governing equations independently of one another were some of the first schemes utilized. Pratrap and Spalding

(1976) followed this procedure to solve the momentum equations and estimate the pressure at each marching station during the global sweep. Moore and Moore (1979) and Chilukuri and Pletcher (1980) utilized a global Poisson equation to evaluate the entire pressure field between the regular space-marching sweeps.

These methods represent a significant improvement from the truly parabolic, single-pass space-marching methods. However, the lack of coupling between the velocity and pressure solutions reduces the convergence rate for flows with substantial pressure gradients.

Coupled methods A study of space-marching with a reduced form of the steady, incompressible Navier-Stokes equations was carried out by Rubin and Reddy (1983). In their formulation, the streamwise diffusion was dropped in the ξ-momentum equation, and all diffusion was eliminated from the η-momentum equation. A special pressure equation was solved with boundary conditions at the top and outflow boundaries only. They discuss in some depth the questions of stability and consistency. Several differencing schemes are compared and judged on their respective virtues. Brown (1983) used a method similar to the above to study flow separation.

In the works mentioned above, both Rubin and Reddy (1983) and Brown (1983) solved the coupled continuity and momentum equations simultaneously to resolve the velocity and pressure fields. They used a staggered grid to prevent the decoupling of the velocity and pressure.

Liu and Pletcher (1986) used a coupled, space-marching procedure to solve the compressible Navier-Stokes equations on a regular grid.

Ramakrishnan and Rubin (1986) extended the space-marching algorithm of Ru-

bin and Reddy (1983) to unsteady flows. The results they show are for the reduced Navier-Stokes equations, although they state that the method should be extendable to the full equations. Their comments on stability seem to be limited to the reduced set of equations. An important point for the present study is that they found that fine grids for large Reynolds number flows do not produce a steady solution.

Himansu and Rubin (1987) employed a multigrid method to accelerate convergence in their space-marching scheme.

Full Navier-Stokes equations

A successful attempt to increase convergence rates in steady cases was made by Bentson and Vradis (1987). They solved both the partially parabolized and the full Navier-Stokes equations in incompressible form using a space marching scheme on a staggered grid. A pressure-Poisson equation was solved using an iterative, reverse sweep. This update occurred after each global sweep. They found that 5 – 10 iterations of the Poisson-solver were required. As a further aid to convergence, they integrated the streamwise momentum equation along the grid lines which lie parallel to the stream lines. They did this from down-stream to up-stream. This step was only performed approximately every 5 global sweeps. These additional computations were found to improve the rate of convergence for all flows, but especially for internal flows.

Most of the space-marching schemes discussed above, for both reduced and full Navier-Stokes, employed a staggered grid. A deliberate departure from that tradition was made by TenPas and Pletcher (1987). They used a regular grid to solve the full Navier-Stokes equations (although the option of using the PPNS equations was

coded).

The scheme was strictly for steady flows, and the compressible form of the equations was used. Incompressible flows were resolvable since density had been eliminated using the ideal gas law. The equations (x-momentum, y-momentum and continuity) were solved in primitive variable form. The block system that was solved was for $[u, v, p]^T$. Two-dimensional cases were reported. A three-dimensional version was later produced and tested (TenPas 1990).

The results shown in both of these reports were largely for internal flow. The flow over a symmetric cylinder, using an H-grid was the lone external flow case. The internal-flow results tended to be accurate on moderately-course grids, and the convergence rate was found to be quite attractive. The external-flow case was found to be more difficult. Multigriding was required to start the solution, and resolution about the stagnation points was found to be rather poor.

Upwind relaxation methods Another set of algorithms should be mentioned because a form of them appear as essentially space-marching. These methods have been given the name upwind relaxation methods. A form of flux-splitting is used in these methods, resulting in a block-pentadiagonal matrix. In all of the references included below, the equations were solved in conservation law form, using conservation law variables. One group (Napolitano and Walters 1986) also solved the incompressible form using vorticity-stream function equations.

Thomas and Walters (1985) used this procedure to calculate steady flows using an unsteady formulation. They used the flux-splitting method developed by Van Leer (1982) for their upwind differencing. Line Gauss-Seidel relaxation is applied to

the block system, with the option of using either ξ or η lines. Of course only when the ξ lines were used exclusively, and the procedure was carried out from upstream to downstream did it become a space-marching method such as the others described above. Couette flow, compressible flow over a flat plate, and shock-boundary-layer interaction were studied.

Further studies were made by Napolitano and Walters (1986). Incompressible weakly separated channel flow and incompressible driven cavity solutions were presented. Compressible flows included shock-boundary-layer interaction and turbulent flow in the terminal shock region of an inlet/diffuser. For this first compressible case, comparison was made between marching in the streamwise direction only and alternating down- and up-stream sweeps. Convergence was slightly better for the streamwise-only marching case.

Taylor et al. (1989) extended the above algorithm to include sub-iterations at each time level. They restricted their work to steady flows as well. Vertical line Gauss-Seidel iteration was used exclusively, but for subsonic flows they swept the spatial domain both backward and forward. They experienced a problem with diagonal dominance in the subsonic flat plate flow. Under-relaxation was required to restore stability.

Present Space Marching Method

Improved methods of solution are always welcome. Better accuracy, efficiency and stability are continually pursued. The work found in this report builds on that of TenPas (1990). The extensions of that work are toward better resolution of the front stagnation point on a cylinder, heat transfer results, and unsteady flows. To

this end, the code by TenPas (1990) was modified to run on a C-grid, with which resolution in the upstream stagnation region was improved, and the full energy equation was added. A time loop, which contains the original space-marching iterations, was added. The sub-iterations at each time level were performed using the original space-marching method. It is believed that this is the first time a C-grid has been used with a space-marching procedure.

The full two-dimensional Navier-Stokes equations were solved on a 'regular' (not staggered) grid with the present procedure. The unsteady version of this scheme is similar to Ramakrishnan and Rubin (1986) except that they solved the reduced form of the equations on a staggered grid.

Two types of grids were used. For the flat plate, a Cartesian H-grid was used. The C-grid was used for the flow over a right circular cylinder. Heat transfer was calculated for various flows.

The algorithm used in this study differs from the upwind relaxation methods described above in several ways. In the present scheme, the solution at each marching station was obtained by Gauss-elimination rather than an iterative scheme. The streamwise pressure gradient was always forward differenced — although for higher Mach numbers it is believed this would have to be modified — finally, no provision for marching in any direction other than streamwise was included.

Flow Over a Right Circular Cylinder

The study of flow (with and without heat transfer) over blunt bodies has been pursued, both experimentally and numerically, for some years. The results of such studies can be used to improve the design of aircraft, missiles, torpedoes, and turbine

blading, as well as many other products. When the physical region of interest is near the front stagnation point, cylinders and spheres can be used as representative blunt bodies. This is due to the fact that, in this region, the details of the flow are nearly the same regardless of the overall geometry, as long as the body is blunt. This can greatly simplify the geometry and allow comparison of results with the data of many other researchers.

In the present study, crossflow over a cylinder was used as a model of the flow over a two-dimensional blunt body. The physical phenomena of the flow over a cylinder can be very complicated. Separation — sometimes several counter-rotating vortices — is common. Unsteadiness is inherent to the flow above a certain Reynolds number. Turbulent flow in some or all of the separated regions occurs at higher Reynolds numbers. Following is a more detailed description of these regimes.

For a Reynolds number less than about seven, the laminar boundary layer remains everywhere attached to the cylinder. For higher Reynolds numbers, the flow separates at some point on the cylinder and reattaches downstream of the rear stagnation point. This creates a region of recirculating flow behind the cylinder. The length of this recirculation zone varies approximately linearly with Reynolds number as long as the flow is steady. The upper limit of steady flow is at a Reynolds number of about 40. Above that point, the separation bubble begins to oscillate with a definite frequency. Vortices begin to shed alternately from either side of the cylinder. This is the well-known von Kármán vortex street. At the lower end of the Reynolds number scale, the flow remains entirely laminar. Turbulence begins to appear at higher Reynolds numbers.

Achenbach (1968) proposed three Reynolds number ranges for characterizing the

various flow regimes. In the subcritical range ($Re < 2\times10^5$), the boundary layer is laminar up to the separation point. In the critical range ($2\times10^5 < Re < 1.5\times10^6$) the boundary layer remains laminar up to separation, but becomes turbulent soon after separating. This turbulent bubble reattaches as a turbulent boundary layer which then separates again downstream. At yet higher Reynolds numbers (the supercritical range), the transition point occurs upstream of the separation point.

The frequency of the vortex shedding is described using the dimensionless parameter, Strouhal number

$$\mathcal{F} = \frac{nd}{u_r}$$

where n is the dimensional frequency. The Strouhal number ranges from 0.2 (subcritical) to 0.25 (supercritical). Because of the self-excited nature of this phenomenon, anything that inhibits the interaction of the separation bubbles can change the characteristics of the wake flow. To eliminate the unsteadiness, some researchers have inserted a splitter plate on the plane of symmetry, downstream of the cylinder.

Review of experimental studies

A substantial amount of experimental work aimed at cylinders in crossflow with heat transfer has been performed over the years. Krall and Eckert (1973) studied various low Reynolds number flows. They concentrated on a uniform heat flux boundary condition. Zukauskas and Ziugzda (1985) have shown that, for the local Nusselt number in the vicinity of the stagnation point, whether constant heat flux or uniform temperature boundary conditions are used is unimportant since the results coincide.

Earlier, Eckert and Soehngen (1952) had studied the case of a reasonably uniform

temperature boundary condition. They heated the cylinder before beginning their measurements and allowed it to cool naturally. They believed that this cooling had negligible effect on their results. In both of these studies, Eckert and his coworkers intended, not necessarily to prove or point out something in particular, but rather to add to the data base of results which are scarce — local Nusselt numbers for low Reynolds number flows.

Acrivos et al. (1965) presented low Reynolds number flow heat transfer results also for the case of constant heat flux. Despite the fact that the maximum Reynolds number that they ran was about 225, they claimed that the intent of the work was to study flows in the limit of vanishing viscosity. In order to model the conditions for which the laminar thermal boundary layer theory is valid, they used an oil tunnel for which the Prandtl number was in excess of 1000. They point out that the heat transfer results were particularly sensitive to the blockage factor. Unfortunately, they believed that their results were affected by the level of blockage in their test apparatus. The results shown by them may be off by ten to twenty percent. From a qualitative standpoint, however, they show that, for high Reynolds numbers, the Nusselt number in the reversed flow region is independent of variation in Reynolds number. In the region of attached flow, it should vary such that $\frac{Nu_d}{Pr^{1/3}}$ is proportional to Re_d. They also compare the results of cylinders with splitter plates to those without.

These researchers also developed a theoretical model of the flow in the separated region of bluff bodies at high Reynolds numbers. It consisted of separate equations for the inner (close to the body) and outer (far from the body) regions. For the region nearest the body they proposed the following set

$$\overline{u}\frac{\partial \overline{u}}{\partial x} + \overline{v}\frac{\partial \overline{u}}{\partial y} = -\frac{1}{2}\frac{\partial \overline{p}}{\partial x} + \Delta^2 \overline{u}$$

$$\overline{u}\frac{\partial \overline{v}}{\partial x} + \overline{v}\frac{\partial \overline{v}}{\partial y} = -\frac{1}{2}\frac{\partial \overline{p}}{\partial y} + \Delta^2 \overline{v}$$

$$\frac{\partial \overline{u}}{\partial x} + \frac{\partial \overline{v}}{\partial y} = 0$$

where the variables with the overbars are defined as:

$$\overline{u} = uRe, \quad \overline{v} = vRe, \quad \overline{p} = pRe,$$

For the bulk of the bubble, or far field (except near the body)

$$u\frac{\partial u}{\partial \hat{x}} + \hat{v}\frac{\partial u}{\partial y} = -\frac{1}{2}\frac{\partial p}{\partial \hat{x}} + \frac{\partial^2 u}{\partial y^2}$$

and

$$\frac{\partial p}{\partial y} = 0$$

where

$$\hat{v} = -\int_0^y \frac{\partial u}{\partial \hat{x}} dy, \quad \hat{x} = \frac{x}{Re}$$

Unfortunately, they were unable to develop a theory which linked the two regions.

A follow-up study was performed by Acrivos et al. (1968). In this new study they extended their experiments to other body shapes. These included a half-cylinder, wedges, and a flat plate at angles of attack. They believe that the new results verified their theoretical model from the previous work.

A study which included an electrochemical technique to measure velocity gradients on the wall was performed by Dimopoulos and Hanratty (1968). They report results for cylinders with and without a splitter plate. Flows with Reynolds numbers between 60 and 360 were studied. They show that the technique is valid, that the apparatus does not require calibration, and is easy to fabricate.

A study of the flow over an impulsively started cylinder was conducted by Bouard and Coutanceau (1980). They studied a range of Reynolds numbers from 40 to 10,000.

The results shown were extensive, including unsteady recirculation bubble lengths, velocity profiles on the line of symmetry behind the cylinder, and the value and location of the maximum negative velocity on that line. Their data are very useful for comparison to numerical results.

Zukauskas and Ziugzda (1985) have compiled a book on the subject of flow and heat transfer over cylinders in crossflow. For further study, reference should be made to this extensive work.

There is a tendency for this work to branch off to more complex flows. Heat transfer with varying levels of free stream turbulence is one example. However, more results of fundamental nature are still needed. The data base is particularly lacking in local Nusselt number information for flows of low Reynolds number.

Review of numerical studies

Numerical solutions of the Navier-Stokes equations for flow past a cylinder have a rather long history, beginning well before the invention of computers. The earliest formulation was presented by Thom (1933) in which he solved arithmetically the viscous flow equations in two dimensions using the method of of successive approximations. He studied flows at Reynolds numbers of 10 and 20.

Solution of the governing equations using the computer is a relatively recent advancement. Because of limited computer resources in early years, a simplified set of equations known as the boundary-layer equations were popular. The flows resolvable using these equations are limited due to the assumptions used to derive them. Geometries with large flow curvature (and, therefore, substantial transverse pressure gradient) and flows with large separation regions are not usually well suited

to solution with the boundary-layer equations.

With more powerful computers came the ability to solve more complete sets of the governing equations. This allowed more complicated flows to be calculated. Thus, when the solution of the full equations became possible, realistic calculations of the flow over a cylinder also became a reality.

Steady flow A study of the flow over a cylinder, using the stream-function vorticity-transport equations was carried out by Son and Hanratty (1969). They intended to extend the range of reliable, steady data to higher Reynolds numbers. Results for Reynolds numbers of 40, 200, and 500 were presented. They used a time-marching method and reported some transient data. Some of their steady data are compared to the experimental results of Dimopoulos and Hanratty (1968). Their findings were similar to those reported by others, in that the steady flow solution was not the same as the time-averaged solution of the actual unsteady flow.

Dennis and Chang (1970) applied a stream-function vorticity-transport algorithm to the steady, incompressible flow over a circular cylinder. They too hoped to extend the Reynolds number range for reliable data. They limited the Reynolds number to the range $5 \leq Re \leq 100$. Their findings confirm earlier results which show a linear relationship between the separation bubble length and Reynolds number.

An exceptionally complete paper was published by Fornberg (1980). He included not only his own numerical results, but also a survey of those of a large number of other researchers. The upper Reynolds number limit was 300. All of his results were for steady, symmetric flow.

Noticing a shortage of data for turbulent flow over cylinders, Majumdar and

Rodi (1985) determined to contribute to that area. They used a variation of the TEACH (Gosman and Pun 1974) type of algorithm, with a k-ϵ turbulence model. Results for Reynolds numbers of 40, 10^5, 1.4×10^5, and 3.6×10^6 were shown. For the higher Reynolds numbers, the flow would be unsteady. A steady solver was used on a symmetric grid. Because of this, the results in the separated region tended to be off somewhat.

For incompressible flows, Kwak et al. (1984) used a pseudo-compressibility method to solve for steady flows. It was an implicit, approximately factored scheme which did not require a Poisson equation for the pressure. However, higher order smoothing terms were required for stability. They solved for the flow over a cylinder using a full O-grid at a Reynolds number of 40 as one test case. Since this work did not concentrate on the flow over a cylinder, the results shown were not extensive.

A comparison between an explicit upwind method and the alternating direction implicit (ADI) scheme (both for the stream-function vorticity-transport equations) was done by Borthwick (1986). Results for a range of Reynolds numbers between 40 and 400 were reported. He found that such a large amount of artificial viscosity was produced by the explicit scheme as to prohibit vortex shedding at all Reynolds numbers. A special case was attempted to explore this problem by letting $Re = 40,000$. Even in this extreme case, no vortices were shed. The ADI method, however proved to be quite reliable in resolving the vortex sheet.

Chun and Boehm (1989) used a stream-function vorticity approach to calculate flow over a right-circular cylinder with heat transfer. Central differences were used when the cell Reynolds number was less than two, and a variation of the hybrid representation (which they refer to as the power-law scheme) for greater cell Reynolds

numbers. They resolved only half of the flow domain, using a symmetric boundary. They say that their treatment of this symmetric boundary could closely approximate time-averaged behavior in the wake region. This has been disproved by Karniadakis and Triantafyllou (1989) who time-averaged the flow field over a cycle and found that, for a Reynolds number of 100, the average separation bubble length was substantially smaller than indicated by the corresponding steady calculation. Since heat transfer was not considered by Karniadakis and Triantafyllou (1989), it is unclear as to how this affects the Nusselt number distribution.

Paolino et al. (1986) used an explicit finite-control-volume approach to calculate the flow with heat transfer about a cylinder. Their results were for high Reynolds numbers (3000 and 70,800). When they compared their numerical heat transfer results with those from experiments, they appeared to match poorly downstream of the separation point. On the front portion of the cylinder, the agreement was quite good. Although they state that the local Nusselt number should have relative maxima at stagnation points, their results show a drop in Nusselt number close to the leading edge stagnation point. This phenomenon has been observed in boundary layer solutions and was found in the present work as well.

Unsteady flow The unsteady nature of flows can be due to several driving forces. One would be a time variation in body forces (such as gravitational and electromagnetic forces). Another is unsteady boundary conditions. The unsteadiness may be an initial step change, or continuous changes with time. Still another driving force is the inherent unsteadiness such as in vortex shedding behind a body in cross-flow. The free stream conditions may be steady in this case. In this work, only the

case of unsteady boundary conditions (impulsively started cylinder) was successfully computed.

Several researchers have studied the case of a cylinder, started with either uniform or potential flow conditions initially. Loc (1980) used a stream-function vorticity-transport formulation to resolve this type of flow. A fourth order scheme for the stream-function, and a second order method for the vorticity-transport equation was reportedly used. Reynolds numbers of 300, 550, and 1000 were discussed.

Loc was able to resolve secondary vortices that other researchers had missed. He used the photographs of Coutanceau and Bouard (1980) for comparison.

Loc and Bouard (1985) performed further studies using the same scheme. They concentrated on Reynolds numbers of 3×10^3 and 9.5×10^3 for this new study. More and finer details of the flow were resolved.

More recently, a study of the same type of flow was done by Chamberlain (1987). The major difference between his work and that of the studies reported above, was the solution method. The stream-function vorticity-transport equations were again solved, but the Poisson equation for the stream function was dealt with using a fast direct method based on the fast Fourier transform. The vorticity-transport equation was solved using an ADI scheme.

In a paper expounding the advantages of their fractional-step method, Rosenfeld et al. (1988) reported results for flow start-up over a cylinder at a Reynolds number of 40. Finite volumes on a staggered grid were used to ensure conservation of mass. The momentum equations were solved in flux-variable form for the velocities. The resulting velocity field was not, in general, divergence-free. Pressure was computed using a Poisson solver and corresponded to a divergence-free velocity field. The

velocities were then corrected to satisfy the continuity equation. For flow over a cylinder, a full O-grid was used. The outer boundary conditions were rather severe, allowing no mass to cross. They believe that, at large times, this boundary condition adversely affected their results.

This survey is not intended to be complete. Many other researchers have produced excellent results using a variety of methods. The research mentioned in this review is meant only to point out a portion of the work that has been done in the area of flows about right circular cylinders — both experimental and numerical.

Motivation for the Present Work

Turbomachinery design has become a very exacting science. Designers put forth efforts to gain a fraction of a percent of efficiency. Therefore, knowledge of the intricate details of the fluid flow and heat transfer is becoming increasingly important. These details include (but are not necessarily restricted to) transition, turbulence, separation, and unsteadiness. Perhaps even more important is the interaction of these phenomena. Research is currently being performed to gain knowledge in these areas.

Experiments by Vanfossen and Simoneau (1985) have been conducted to study the relationship between free stream turbulence and heat transfer. Specifically, they were interested in investigating the mechanism which increases heat transfer in the stagnation region of a turbine blade.

This work was extended by O'Brien et al. (1986). They studied the effect of rotor wakes passing over a downstream blade row. The particular area of interest was heat transfer in the stagnation region. Both the rotating and stationary blade

rows were made up of cylinders. Splitter plates were placed behind the stators to eliminate the effect of shedding vortices.

The present work was intended to contribute to the above body of research. One of the long term goals of this project was to develop the numerical procedures needed to simulate the effect of free stream unsteadiness on stagnation region heat transfer. This problem is very complex, and becomes more so when the Reynolds number is large. Before advancing to this application, it is important to carefully verify various features of the basic numerical scheme. The majority of this dissertation was devoted to the latter task. To this end, heat transfer results for steady flow over a cylinder were calculated. This was extended to unsteady flow over an impulsively started cylinder. To the author's knowledge, these are the first such heat transfer results reported for the latter unsteady flow.

An attempt was also made to advance to flows with vortex shedding. This requires that the flow field be evaluated over the entire cylinder (a symmetric boundary condition is not allowed). Although the reasons remain under investigation, the present method has not been able to resolve this phenomenon.

CHAPTER 2. GOVERNING EQUATIONS

In this chapter, a mathematical model for unsteady, laminar, subsonic flow is presented. First, the nondimensionalization is described, then the flow geometry is set forth. Next, the set of fundamental conservation laws that describe the motion of a homogeneous fluid are stated. The constitutive relations, equation of state and transport property formulas that close the model are given. Reductions of the general mathematical model that are valid for specific flow regimes are discussed, and the optional simplifications in the model to reduce the computational requirements are described. The transformation of the governing equations to the computational domain is presented in the final section of the chapter.

The variables in the equations presented here will be dimensionless. The use of dimensionless variables removes the restrictions of a particular system of units and reduces computer round-off error by normalizing the variables. Dimensions are canceled from the dimensional equations by multiplying or dividing the variables by dimensional reference constants. The reference quantities and the corresponding dimensionless variables are defined in the following manner (dimensional quantities are indicated by a tilde, free stream properties are subscripted r, surface quantities with *surf*, and reference values are denoted by the subscript R):

$$t = \frac{\tilde{t}}{\left(\frac{L_R}{u_r}\right)} \qquad x = \frac{\tilde{x}}{L_R} \qquad y = \frac{\tilde{y}}{L_R} \qquad \rho = \frac{\tilde{\rho}}{\rho_r}$$

$$u = \frac{\tilde{u}}{u_r} \qquad v = \frac{\tilde{v}}{u_r} \qquad p = \frac{\tilde{p}}{\rho_r U_r^2} \qquad S = \frac{T - T_{surf}}{T_r - T_{surf}}$$

$$T = \frac{\tilde{T}}{T_r} \qquad \mu = \frac{\tilde{\mu}}{\mu_R} \qquad C_1 = \frac{\tilde{C}_1}{\tilde{C}_1} \qquad C_2 = \frac{\tilde{C}_2}{T_r}$$

$$R = \frac{R}{\left(\frac{u_r^2}{T_r}\right)} \qquad c_p = \frac{\tilde{c}_p T_r}{u_r^2} \qquad k = \frac{\tilde{k}}{k_R} \qquad \gamma = \frac{\tilde{c}_p}{\tilde{c}_v}$$

$$\mu_R = \mu_r Re \qquad k_R = \frac{k_r Re\, Pr}{c_p}$$

Here, L_R is a flow field characteristic length, x and y are the Cartesian coordinates, u and v are the respective Cartesian velocity components, p is the static pressure, S is the thermal variable used in the energy equation; T is the static temperature, ρ is the density, μ is the dynamic viscosity, k is the thermal conductivity, C_1 and C_2 are the Sutherland constants, R is the gas constant, γ is the specific heat ratio, and c_p is the constant pressure specific heat. The reference properties, μ_R and k_R were chosen so that the dimensionless equations appeared identical to the dimensional ones. The Reynolds number, Mach number, and Prandtl number are defined as

$$Re = \frac{\rho_r u_r L_R}{\mu_r} \qquad M = \frac{u_r}{c_r} \qquad Pr = \frac{\tilde{c}_p \mu_r}{k_r}$$

Flow Geometry and Coordinate Systems

The space-marching method is best suited to problems having a principal flow direction. Arbitrary geometry is accommodated by the use of a curvilinear, body-fitted coordinate system created by employing an independent variable transformation. Figure 2.1 depicts a flow domain in physical coordinates, and Figure 2.2 shows the computational domain. The flow domain is bounded by an inlet flow plane upstream, an exit flow plane downstream, a free stream boundary on the top, and symmetry on the bottom (except for the body surface).

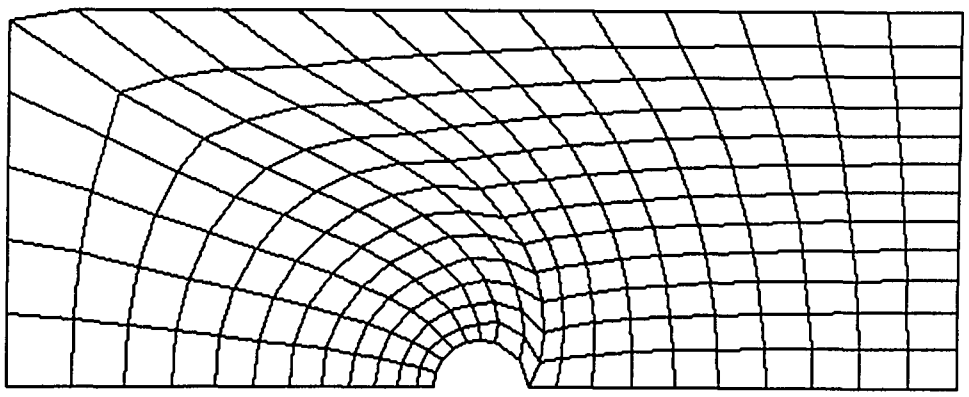

Figure 2.1: Physical space

The body-fitted coordinates are best oriented in an manner that most closely follows the primary flow direction. The space-marching direction (ξ direction) is roughly aligned with the flow direction whenever possible. The constant ξ lines are thus preferably approximately normal to the flow streamlines and are termed

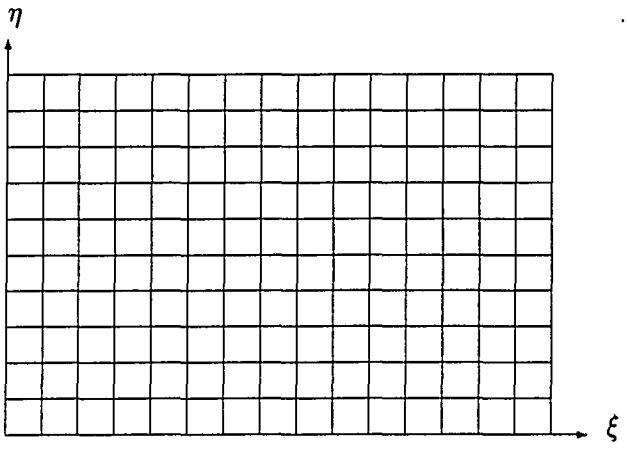

Figure 2.2: Computational space

"marching stations". The upstream boundary is the $\xi = \xi_{min}$ surface for an H-grid but is a segment of the $\eta = \eta_{max}$ line for a C-grid. The downstream boundary is the $\xi = \xi_{max}$ surface for either grid type.

In this work, the term "streamwise" is used to refer to the ξ-direction (along lines of constant η) and the term "transverse" is used to denote the direction along the η lines (constant ξ). It should be kept in mind that these terms do not relate to the flow direction in all regions of all flows due to flow reversal and various grids.

In addition to aligning the space-marching direction with the principal flow direction, the use of body-fitted coordinates has other advantages. The boundaries are defined by surfaces upon which one of the coordinates is constant. Thus the boundary conditions are more easily and more accurately applied. Also the spacing of the coordinate lines may be varied within the flow domain to concentrate grid points in regions where gradients in the flow properties are largest. Meanwhile a uniform

computational grid is maintained. This allows the use of algebraically simple and accurate finite-difference approximations of derivatives.

A generalized independent variable transformation is carried out to generate the body-fitted coordinates, ξ and η as such:

$$\xi = \xi(x, y), \qquad \eta = \eta(x, y)$$

The transformation introduces metric terms into the equations that provide the geometric information needed. Definitions of the metrics and the Jacobian of the transformation are given in Appendix A.

Conservation Laws

The equations representing the conservation of momentum, mass, and energy — collectively referred to as the Navier-Stokes equations (Anderson et al. 1984) — govern the flow of a compressible fluid. These equations are satisfied at every discrete point within the flow field. Ultimately, it is the boundary conditions which are imposed upon the flow which determine the particular solution for a given problem.

Solution methods vary in the form of the equations used to express the conservation laws. The form employed for the present study is a system of nonlinear partial differential equations with the Cartesian velocity components, pressure, and S as the primary dependent variables. The solution vector, $\bar{q}$, is defined as

$$\bar{q} = [u, v, p, S]^T$$

The equations chosen to solve for these unknowns were the continuity equation, the x- and y-momentum equations, and the energy equation. Each of these equations was first transformed using an independent variable transformation before solving.

Governing equations in physical coordinates

For a compressible flow in the absence of body forces, four governing equations are needed to solve for the unknowns presented above. Additional equations are needed to fix the state and to calculate properties such as viscosity, and thermal conductivity.

The two-dimensional Cartesian coordinate form of the momentum equations, the continuity equation, and the energy equation can be expressed in dimensionless vector form as:

$$\frac{\partial \overline{U}}{\partial t} + \frac{\partial \overline{E}}{\partial x} + \frac{\partial \overline{F}}{\partial y} = 0 \tag{2.1}$$

The derivative with respect to time vanishes for steady flow. The vectors in the equation above are

$$\overline{U} = [\rho u, \rho v, \rho, \rho e_t]^T$$

$$\overline{E} = \begin{bmatrix} \rho u^2 + p - \tau_{xx} \\ \rho uv - \tau_{xy} \\ \rho u \\ \rho u h^o + Q_x - \Phi_x \end{bmatrix}$$

$$\overline{F} = \begin{bmatrix} \rho vu & & - & \tau_{xy} \\ \rho v^2 & + \; p & - & \tau_{yy} \\ \rho v & & & \\ \rho v h^o & + \; Q_y & - & \Phi_y \end{bmatrix}$$

The total specific energy of the fluid is defined here as the sum of the internal and kinetic energies

$$e_t = e + \frac{u^2 + v^2}{2}$$

and the total enthalpy is the usual sum of the static enthalpy and the kinetic energy

$$h^o = e + \frac{p}{\rho} + \frac{u^2 + v^2}{2}$$

The viscous terms in the energy equation expand to

$$\begin{aligned} \Phi_x &= u\tau_{xx} + v\tau_{xy} \\ \Phi_y &= u\tau_{xy} + v\tau_{yy} \end{aligned}$$

Equation of state and property evaluation

The fluid is assumed to behave as a perfect gas with constant specific heats. Thus, the thermodynamic properties of the fluid are related through the following equations

$$\rho = \frac{p}{RT} \tag{2.2}$$

$$h = c_p T \tag{2.3}$$

The specific heats are assumed constant and are determined from the gas constant and the ratio of specific heats.

$$c_p = R\frac{\gamma}{\gamma - 1} \tag{2.4}$$

The equation of state (Equation 2.2) is used to eliminate density in the momentum, continuity, and energy equations.

Boundary conditions

The equations of motion for unsteady, compressible flow are hyperbolic-parabolic in character. In the incompressible regime, they become parabolic-elliptic. However, for steady, subsonic flow the governing equations are strictly elliptic. The method used in this study was initially developed to solve the steady form of the equations; the time terms were added later. The solution procedure remains largely unchanged in the unsteady version. The spatial iterations were simply nested inside a new iteration level — the temporal step. The boundary conditions are the same for unsteady flows. Initial conditions take the place of the initial guess used in the steady case.

For subsonic flow, the solution may be affected by conditions at all points on the flow boundaries. However, for moderate and high Reynolds number flows the significant conditions are not the same for all points — upstream conditions influence the flow differently than downstream conditions. In this study it is assumed that the problem is well-posed with prescribed conditions on the inlet boundary (given $[u, v, p, S]$ profiles). Although the upstream pressure can change during a given iteration, the entire pressure field is adjusted after each iteration, by adding a constant

to the pressure at each nodal point, to return it to the specified value. The flow conditions imposed at the exit boundary are that the pressure profile further downstream is uniform (though this value can also vary from iteration to iteration), that streamwise diffusion and dissipation are negligible, and, should the flow be reversed at the final station, it is assumed that the velocity downstream is zero.

The conditions for the side boundaries vary depending on the physical aspects of that specific boundary. On solid walls the no slip and no penetration conditions on velocity are applied. The normal pressure gradient is assumed to be zero. Flow may cross free stream boundaries, but the diffusion terms are assumed to be negligible. The specific treatment of different boundary conditions is presented in greater detail in Chapter 4 in terms of the numerical solution.

Model Closure

The transport terms and fluid properties contained in the fundamental conservation laws must be modeled to complete the mathematical formulation. The relationships given below were selected for the flow regimes of interest in this study. The solution algorithm is not believed to be restricted to these particular formulations, though use of other models would require careful evaluation and testing.

Constitutive relations for laminar flow

For laminar flow of a Newtonian fluid the viscous stresses are modeled by assuming they are proportional to the rate of strain of a fluid element. Using Stokes' hypothesis for the second coefficient of viscosity leads to the following expressions for the viscous stresses in terms of the velocity gradients.

$$\tau_{xx} = \frac{2}{3}\mu\left(2\frac{\partial u}{\partial x} - \frac{\partial v}{\partial y}\right)$$

$$\tau_{yy} = \frac{2}{3}\mu\left(2\frac{\partial v}{\partial y} - \frac{\partial u}{\partial x}\right) \tag{2.5}$$

$$\tau_{xy} = \mu\left(\frac{\partial u}{\partial y} + \frac{\partial v}{\partial x}\right) = \tau_{yx}$$

And the heat flux, given by Fourier's law of heat conduction, is proportional to the gradient of the temperature field.

$$\begin{aligned} Q_x &= -k\frac{\partial T}{\partial x} \\ Q_y &= -k\frac{\partial T}{\partial y} \end{aligned} \tag{2.6}$$

Transport property relationships

In keeping with the perfect gas model above, the transport properties are assumed to vary with temperature while the Prandtl number remains constant. The viscosity is evaluated from the Sutherland formula, and the thermal conductivity is obtained from the definition of the Prandtl number and the viscosity.

$$\mu = C_1 T^{3/2}\frac{(1+C_2)}{(T+C_2)} \tag{2.7}$$

$$k = \frac{c_p \mu}{Pr} \tag{2.8}$$

Reduction of the Governing Equations

The simplification of the equations which has been termed "parabolization" should be mentioned. For flows at moderate and high Peclet number, the effects of streamwise diffusion and dissipation are negligible when compared to the corresponding transverse terms. Computational efficiency is improved by dropping these terms from the set of governing equations. The set of equations which results from incorporating this approximation are known as the partially parabolized Navier-Stokes or PPNS equations (see, for instance Anderson et al. 1984). This option is implemented in the computer code by a switch, set in the input to the program, to bypass calculation of these streamwise terms. In this study, the simplified form was only used to start the computation (first global sweep) and at outflow boundaries (as a form of boundary condition).

Transformation of the Governing Equations

To better facilitate a numerical solution for problems with arbitrary geometry, an independent variable transformation of the governing equations was performed. The change of independent variables to the computational coordinates was accomplished by applying the chain rule to each derivative. The chain rule operators are:

$$\frac{\partial()}{\partial x} = \xi_x \frac{\partial()}{\partial \xi} + \eta_x \frac{\partial()}{\partial \eta}$$

$$\frac{\partial()}{\partial y} = \xi_y \frac{\partial()}{\partial \xi} + \eta_y \frac{\partial()}{\partial \eta}$$

The transformation introduces metric terms into the equations. These metrics provide the geometric information needed.

The equations may be expressed in several forms depending on the sequence in which the chain rule operations are carried out. For example, the so-called chain-rule-conservation-law form (Hindman 1982) of Equation 2.1 is

$$\frac{\partial \overline{U}}{\partial t} + \xi_x \frac{\partial \overline{E}}{\partial \xi} + \xi_y \frac{\partial \overline{F}}{\partial \xi} + \eta_x \frac{\partial \overline{E}}{\partial \eta} + \eta_y \frac{\partial \overline{F}}{\partial \eta} = 0 \tag{2.9}$$

Alternatively, the equations can be cast in the strong-conservation-law form as

$$\frac{\partial \overline{U}}{\partial t} + \frac{\partial \overline{E'}}{\partial \xi} + \frac{\partial \overline{F'}}{\partial \eta} = 0 \tag{2.10}$$

where

$$\overline{E'} = (\xi_x \overline{E} + \xi_y \overline{F})/J$$

$$\overline{F'} = (\eta_x \overline{E} + \eta_y \overline{F})/J$$

For reasons discussed in Chapter 4, the momentum equations are solved in the chain-rule-conservation-law form, while the strong-conservation-law form (specifically the finite volume form) is used for the continuity equation. Another detail of the transformation that should be noted, is that the diffusion terms in both the momentum equations and the energy equation contain derivatives of metrics. The transformation of the diffusion terms is given in Appendix D.

Equations in computational form

The the equations for two-dimensional flow, Equation 2.1, are expressed in the computational coordinates as

$$\frac{\partial \overline{U}}{\partial t} + \xi_x \frac{\partial \overline{E}}{\partial \xi} + \xi_y \frac{\partial \overline{F}}{\partial \xi} + \eta_x \frac{\partial \overline{E}}{\partial \eta} + \eta_y \frac{\partial \overline{F}}{\partial \eta} = 0 \tag{2.11}$$

where, as before:

$$\overline{U} = [\rho u, \rho v, \rho, \rho e_t]^T$$

$$\overline{E} = \begin{bmatrix} \rho u^2 + p - \tau_{xx} \\ \rho uv - \tau_{xy} \\ \rho u \\ \rho u h^o + Q_x - \Phi_x \end{bmatrix}$$

$$\overline{F} = \begin{bmatrix} \rho vu - \tau_{xy} \\ \rho v^2 + p - \tau_{yy} \\ \rho v \\ \rho v h^o + Q_y - \Phi_y \end{bmatrix}$$

and

$$\Phi_x = u\tau_{xx} + v\tau_{xy}$$

$$\Phi_y = u\tau_{xy} + v\tau_{yy}$$

However, the chain rule must be applied to τ and Q

$$\tau_{xx} = \frac{2}{3}\mu\left(2\left(\xi_x\frac{\partial u}{\partial \xi} + \eta_x\frac{\partial u}{\partial \eta}\right) - \left(\xi_y\frac{\partial v}{\partial \xi} + \eta_y\frac{\partial v}{\partial \eta}\right)\right)$$

$$\tau_{yy} = \frac{2}{3}\mu \left(2 \left(\xi_y \frac{\partial v}{\partial \xi} + \eta_y \frac{\partial v}{\partial \eta} \right) - \left(\xi_x \frac{\partial u}{\partial \xi} + \eta_x \frac{\partial u}{\partial \eta} \right) \right)$$

$$\tau_{xy} = \mu \left(\left(\xi_y \frac{\partial u}{\partial \xi} + \eta_y \frac{\partial u}{\partial \eta} \right) + \left(\xi_x \frac{\partial v}{\partial \xi} + \eta_x \frac{\partial v}{\partial \eta} \right) \right) = \tau_{yx}$$

$$Q_x = -k \left(\xi_x \frac{\partial T}{\partial \xi} + \eta_x \frac{\partial T}{\partial \eta} \right)$$

$$Q_y = -k \left(\xi_y \frac{\partial T}{\partial \xi} + \eta_y \frac{\partial T}{\partial \eta} \right)$$

CHAPTER 3. SOLUTION ALGORITHM

The formulation used here is a modification of a scheme originally developed for the solution of the steady equations only. When the time derivative terms were added, no changes were made to the space-marching procedure. At each time step the solution is converged using multiple space-marching sweeps. Therefore, statements made about the space-marching formulation apply to either the steady or unsteady formulation.

In this chapter, the solution procedure for the governing equations is explained. First, the global iteration strategy is examined. Next, the stability restrictions, unique to the steady space-marching formulation, that must be satisfied in order to advance the solution are reviewed. The method used for accelerating the convergence of the pressure field is then described. Finally, the procedure for solving the unsteady formulation is described.

Traditionally, space-marching algorithms have been used for solving parabolic equations. The complete solution being obtained in a single sweep. However, applied to elliptic problems, a single sweep with a space-marching solver can only approximate the solution. In order for downstream conditions to properly influence the flow upstream, multiple passes (iterations) are necessary. The present solution algorithm, diagrammed in Figure 3.1, consists of two distinct procedures that are executed for

each global iteration:

1. The variables, $\bar{q}^m = [u, v, p, S]^T$, are calculated at each station. Starting from an initial marching station (in the upstream region of the flow field), the solution is space-marched in the downstream direction (approximately). This procedure employs an implicit, finite-difference formulation of Equation 2.1. Assumed values for the pressure field are required — a guess for the first pass, and the most recent (calculated) values on subsequent sweeps.

2. The difference between the newly computed pressure field and the assumed pressure field is assessed as a convergence criterion. A single backsweep with a modified Poisson equation solver is executed to improve the estimate of the correct pressure field.

These two procedures are described in greater detail in the sections below. The numerical formulation is presented in the next chapter.

Space-Marching Solution

The goal researchers had in mind when developing space-marching algorithms was to create schemes which would efficiently calculate steady flows with a primary flow direction. By marching in the streamwise direction to the extent possible, information is rapidly passed from upstream to downstream. The following sections explain some of the important aspects of the basic scheme.

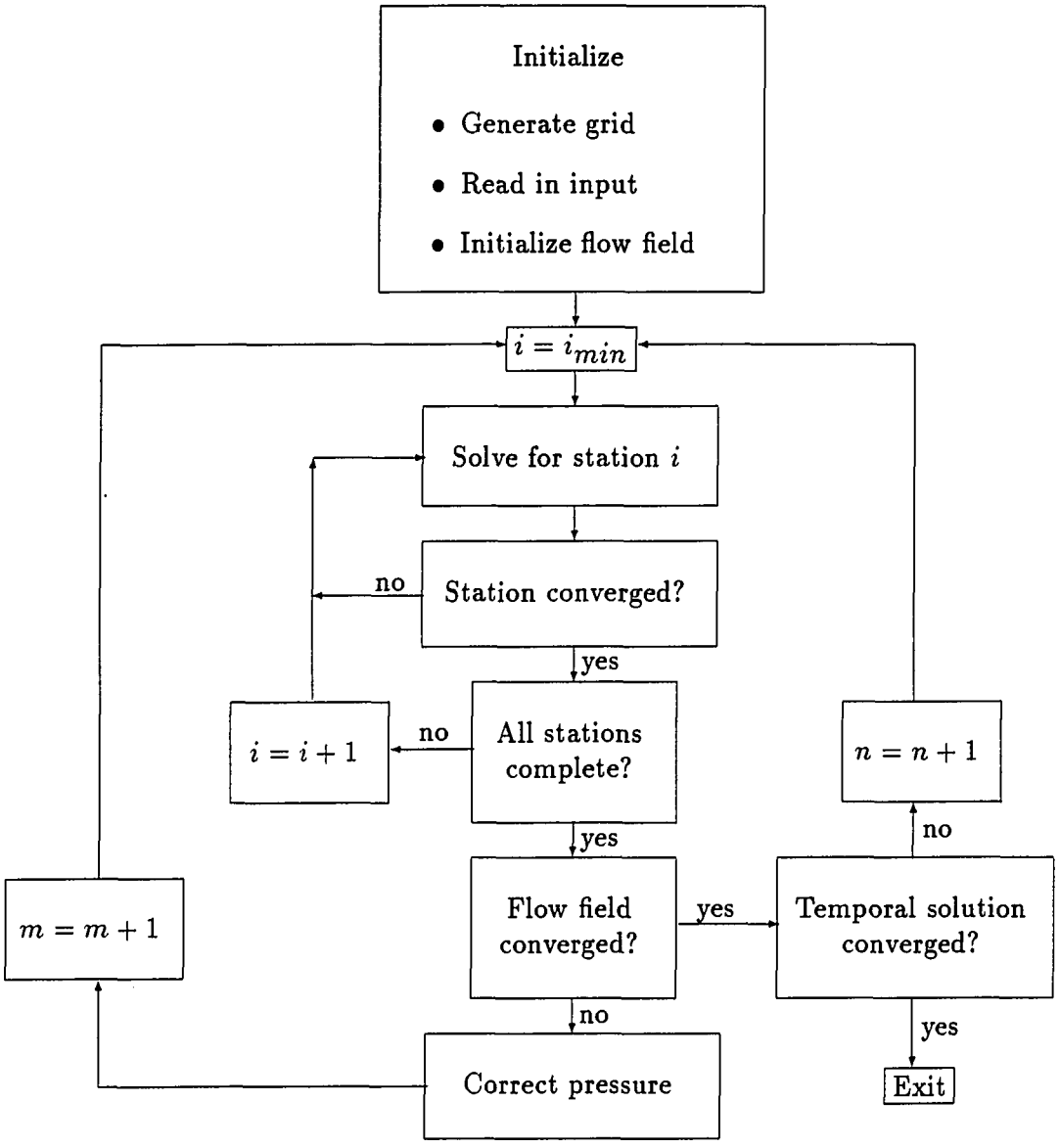

Figure 3.1: Flow chart of algorithm

Coupled, primitive variable formulation

The space-marching procedure is executed by numerically integrating Equation 2.1 by marching in the ξ direction using an implicit, finite-difference method. A flowchart of the procedure is shown in Figure 3.1. The solution is initiated from given flow conditions at the first marching station — the inlet flow boundary for an H-grid, and the line of geometric symmetry running from the body to the inlet flow boundary for a C-grid. At each marching station in turn, a set of four coupled, nonlinear equations is solved for provisional values of the primary flow variables, $\overline{q}^m$. As explained below, the downstream terms in the equations are treated explicitly, using assumed initial values or values obtained from the previous global iteration. Due to the presence of these explicit values, the result of the space-marching solution is only an approximation to the converged solution, depending upon how closely the downstream terms have been approximated. Therefore, repeated sweeps are applied to improve this approximation. The magnitude of change in the solution is used to determine convergence.

Stability of the steady space-marching procedure

For steady, subsonic flow the system of partial differential equations (Equation 2.1) is elliptic in space. It is thus not well-posed as an initial value problem for solution by a single space-marching sweep. However, proper treatment of the streamwise derivative terms allows a stable space-marching calculation to be executed. Linear stability analysis of the frozen coefficient form of Equation 2.1 identifies the stability restrictions on the algorithm. In essence, terms that transmit information from downstream to upstream must be treated as source terms, i.e., fixed values

are used in place of values determined during the marching sweep. The treatment of these direction-dependent terms is described in the following paragraphs.

For subsonic flow, the downstream pressure controls the flow solution through the streamwise pressure gradient terms. The degree to which the streamwise pressure gradient must be restricted is a function of the local Mach number as determined by the Vigneron condition (Vigneron et al. 1978). For the range of Mach numbers considered in this study, the streamwise pressure gradient must be entirely forward differenced. At higher Mach numbers, as the local acoustic velocity is approached, it is desirable to gradually shift the differencing toward the upstream direction. This flow dependent condition reflects the characteristic domain of dependence of the pressure. It should be noted that a flux-splitting type of analysis yields the same results (Rubin 1988).

Downstream velocities and temperatures may also influence the solution through the streamwise convection, diffusion, and dissipation terms. Where the ξ-direction contravarient velocity is positive, the corresponding convection terms are backward-differenced. However, where the flow reverses direction, the streamwise convection terms in the momentum and energy equations must include properties ahead of the current marching station. In practice, the sign of the ξ-direction contravarient velocity is calculated and the ξ-derivatives in the convective terms are differenced appropriately. This type-dependency does not apply to the continuity equation. It is always formulated with fluxes from the previous marching station.

The streamwise diffusion and dissipation terms also involve downstream stations. At moderate and high Peclet numbers, these terms are small compared to the other terms in the respective equations. Therefore, explicit treatment of the downstream

properties in these terms is stable and, except at very low Peclet numbers, has little effect on the convergence rate of the solution.

It should be clear that the complete two-dimensional Navier-Stokes equations are retained. The restrictions are applied only to maintain the numerical stability of the space-marching calculation. The stability restrictions reflect the elliptic nature of the governing equations by requiring that the appropriate information directionality be included in the solution of the local equations. Since the downstream values are unknown, iteration is necessary to converge the initial estimates of these terms, and this process allows downstream boundary conditions to influence the flow solution upstream.

Stability of the unsteady procedure

Rigorous stability (von Neumann) analysis of algorithms which solve the full Navier-Stokes equations is extremely complex. Usually one expects that, for an implicit solution procedure, no stability restrictions should apply.

Since the steady procedure used here is believed to be unconditionally stable, and since the method is implicit, it is believed that there are no stability restrictions (such as those which von Neumann analysis uncovers) on the unsteady algorithm.

Initialization of the space-marching procedure

From the stability considerations discussed above it is clear that estimated values are needed to begin execution of the space-marching procedure. For the first pass, the FLARE approximation (Reyhner and Flügge-Lotz 1968) is used in regions of reversed flow, the streamwise and cross derivatives of the diffusion and dissipation

terms are neglected, and a pressure field is assumed. For successive iterations the downstream velocities are taken to be the "lagged" values from the previous global iteration. Initial flow conditions are required for the unsteady formulation.

Pressure Correction Procedure

Several procedures for accelerating the convergence of the pressure field have been considered. Among them are:

1. Simple under-relaxation of the pressure after each global sweep.

2. Solving a simplified pressure-Poisson equation using a parabolized, marchable solver.

In most cases, most notably the ones employing the C-grid topology in the present work, the solution diverged if neither of these procedures was applied. All of the results shown in this report were obtained using the simplified pressure-Poisson equation. It was found that this additional step was stabilizing, even for unsteady problems.

Motivation for the pressure correction procedure

The pressure field is given special treatment in the algorithm. The reason for the pressure correction procedure is to move information in the direction which is physically correct. In the general case, the flow at any point may be influenced by the conditions at all of the surrounding points. With a space-marching algorithm, the upstream flow conditions needed for the solution across a given station are known and present no difficulties. So attention is focused on the influence of the downstream

terms, which are not known. These must be approximated to advance the space-marching calculation.

As discussed above, for subsonic flow, information is passed from downstream to upstream via the streamwise pressure gradient, the streamwise diffusion and dissipation terms, and the streamwise convective terms in regions of reversed flow. Of these three, for the class of problems dealt with here, the streamwise pressure gradient is believed to be the most significant downstream term in the governing equations; the streamwise viscous stresses are small, and the regions of flow recirculation are limited. Under these conditions the pressure terms exert the greatest influence on the convergence rate.

It follows that if the pressure field is known *a priori*, or if a method is available for determining the pressure, then a single sweep of the space-marching solver will yield an almost-correct solution for all of the flow variables. Almost, because the streamwise diffusion and dissipation terms and the streamwise convective terms in regions of reversed flow are still not known. The pressure correction step in the algorithm permits the introduction of supplemental relationships to more efficiently develop the correct pressure field.

Definition of the pressure correction

The correction scheme used in this project is a modified version of the procedure presented by TenPas (1990). The method used by TenPas was extended to account for a non-orthogonal grid. In the present space-marching formulation, two pressure values are retained at each point during each global iteration: the calculated pressure, p, obtained from the forward, global sweep, and the assumed pressure, $\overline{p}$, resulting

from the pressure-correction step. These provide one of the convergence criteria and are used in the Poisson equation solver described below. As one measure of the error in the solution, the difference, ϵ, between the calculated pressure and the assumed pressure is defined as

$$\epsilon = p^m - \overline{p}^m$$

If $|\epsilon|$ is everywhere less than the specified convergence tolerance, convergence has been achieved. When the flow is unsteady, the time is incremented to the next level. For steady flows, the calculation is terminated. If the maximum absolute value of ϵ exceeds the convergence tolerance, the assumed pressure field is corrected before performing the next space-marching sweep. The pressure correction, p', is applied using the defining equation

$$\overline{p}^{m+1} = \overline{p}^m + p'$$

The actual error in the assumed pressure field, δ, is the difference between the final (converged) pressure and the assumed pressure. Or

$$\delta = p^\infty - \overline{p}^m$$

At convergence, δ, ϵ and p' all approach zero at all points in the field.

The ideal pressure correction is clearly equal to δ. Unfortunately, δ is not easily determined. The methods described below use different assumptions to estimate the pressure correction.

Point relaxation method

The space-marching sweep directly provides a new estimate of the pressure field. The simplest correction method is to under-relax the computed change in pressure

at each node before executing the next space-marching pass. The equation for the pressure correction is simply

$$p' = \omega(p^m - \bar{p}^m) = \omega\epsilon \tag{3.1}$$

Selection of the optimum relaxation factor, ω, is problem dependent.

Regardless of any relaxation factor dependence, a large number of iterations are necessary due to the fact that downstream pressure signals are only passed one station upstream for each global iteration. Thus, as many iterations as there are marching stations must elapse before the downstream boundary pressure is first felt at the initial marching station. During these initial iterations a finite error must exist due to the lack of boundary information in the local solutions. After this initial transient, additional iterations are needed to converge the solution to an acceptable tolerance. Because of these limitations, other methods are preferred. The one used exclusively in this study is described below.

Pressure Poisson equation method

The pressure gradients in the computational space can be isolated by writing the momentum equations in the form:

$$\frac{\partial p}{\partial x} = px = f_1, \qquad \frac{\partial p}{\partial y} = py = f_2 \tag{3.2}$$

The functions on the right-hand sides of Equations 3.2 contain the convective and viscous terms that depend on the velocity field. Taking derivatives, the first of Equation 3.2 with respect to x, and the second with respect to y and summing yields a Poisson equation for the pressure written as

$$pxx + pyy = S_p \tag{3.3}$$

Where

$$S_p = \frac{\partial}{\partial x}(f_1) + \frac{\partial}{\partial y}(f_2)$$

or, by using Equation 3.2,

$$S_p = \frac{\partial}{\partial x}(p_x) + \frac{\partial}{\partial y}(p_y)$$

Since the pressures from the previous global sweep satisfy the momentum equations, these can be used to generate the source term, S_p.

Unfortunately, at any intermediate iteration the space-marched solution is provisional and the value of the source term is known only approximately, so a direct solution for the exact pressure field is not possible. Nonetheless, the converged pressure field must satisfy Equation 3.3, which gives a sound physical basis for estimating the pressure correction.

An alternative form of Equation 3.3 in which the pressure correction explicitly appears is easily developed. The difference between the converged pressure and the assumed pressure values is defined above such that

$$p^{\infty} = \overline{p}^m + \delta$$

The pressure correction can be defined as

$$p^+ = p^{m+1} - \overline{p}^m$$

Assuming the "exact" pressure correction will be obtained implies

$$p^+ = \delta$$

and we attempt to solve for this "exact" correction by expanding the linear Equation 3.3 to include p^+ gives

$$p^+_{xx} + p^+_{yy} = S_{p^+} \tag{3.4}$$

where

$$S_{p+} = \frac{\partial}{\partial x}(px) + \frac{\partial}{\partial y}(py) - \overline{p}_{xx} - \overline{p}_{yy}$$

If a generalized coordinate transformation is used, Equation 3.4 appears like this

$$(\xi_{xx} + \xi_{yy})\frac{\partial p^+}{\partial \xi} + (\eta_{xx} + \eta_{yy})\frac{\partial p^+}{\partial \eta} +$$
$$(\xi_x^2 + \xi_y^2)\frac{\partial^2 p^+}{\partial \xi^2} + (\eta_x^2 + \eta_y^2)\frac{\partial^2 p^+}{\partial \eta^2} + 2(\xi_x\eta_x + \xi_y\eta_y)\frac{\partial^2 p^+}{\partial \xi \partial \eta} = S_{p+} \quad (3.5)$$

where

$$\begin{aligned} S_{p+} &= \xi_x \frac{\partial}{\partial \xi}(\xi_x p_\xi + \eta_x p_\eta) + \eta_x \frac{\partial}{\partial \eta}(\xi_x p_\xi + \eta_x p_\eta) \\ &+ \xi_y \frac{\partial}{\partial \xi}(\xi_y p_\xi + \eta_y p_\eta) + \eta_y \frac{\partial}{\partial \eta}(\xi_y p_\xi + \eta_y p_\eta) \\ &- \left[(\xi_{xx} + \xi_{yy})\frac{\partial \overline{p}}{\partial \xi} + (\eta_{xx} + \eta_{yy})\frac{\partial \overline{p}}{\partial \eta}\right. \\ &+ \left.(\xi_x^2 + \xi_y^2)\frac{\partial^2 \overline{p}}{\partial \xi^2} + (\eta_x^2 + \eta_y^2)\frac{\partial^2 \overline{p}}{\partial \eta^2} + 2(\xi_x\eta_x + \xi_y\eta_y)\frac{\partial^2 \overline{p}}{\partial \xi \partial \eta}\right] \end{aligned}$$

Thus, Equation 3.5 could be solved to estimate the pressure correction. However, solving an elliptic equation at each iteration presents a substantial computational burden.

Another consideration is that in order for the solution of the pressure Poisson equation to be consistent with the converged solution of Equation 2.1, the common terms must be handled in the same manner. In particular, the streamwise pressure gradient must be forward differenced due to the stability restrictions on the space-marching solver.

A forward streamwise difference does not include pressures upstream. It is therefore assumed that the pressure correction at a given node is independent of the errors in the pressure upstream, and that the pressure correction upstream will rectify these

errors. With similar reasoning, the cross derivatives are equated on either side of the equation, and therefore, canceled. With this assumption, a parabolized form of Equation 3.5 is obtained which can be written as

$$(\xi_{xx} + \xi_{yy} + \xi_x^2 + \xi_y^2)p_\xi^+ + \alpha(\eta_{xx} + \eta_{yy})p_\eta^+ + \alpha(\eta_x^2 + \eta_y^2)p_{\eta\eta}^+ = S'_{p+} \qquad (3.6)$$

where

$$\begin{aligned} S'_{p+} &= -(\xi_{xx} + \xi_{yy} + \xi_x^2 + \xi_y^2)\epsilon + \alpha(\eta_{xx} + \eta_{yy})\frac{\partial p}{\partial \eta} \\ &+ \alpha(\eta_x^2 + \eta_y^2)\frac{\partial}{\partial \eta}p_\eta - \alpha(\eta_{xx} + \eta_{yy})\bar{p}_\eta - \alpha(\eta_x^2 + \eta_y^2)\bar{p}_{\eta\eta} \end{aligned} \qquad (3.7)$$

The multiplier, α, is an arbitrary constant used to weight the streamwise and transverse derivatives unequally. For α greater than one, this has the effect of "spreading" the correction in the transverse direction, for instance distributing a spike in pressure throughout the marching station.

The development of Equation 3.6 and 3.7 from Equation 3.4 is presented in finite-difference form in Chapter 4.

Notice that the downstream pressure boundary condition determines the pressure correction at the exit. Equation 3.6 is then integrated in the upstream direction with an implicit finite-difference technique. This backsweep procedure rapidly propagates the downstream boundary information upstream, with much less computational effort than solving an elliptic equation.

As a final step in this pressure correction procedure, a relaxation factor on the estimate is applied such that the actual pressure correction is determined as

$$p' = \omega p^+ \qquad (3.8)$$

and the updated pressure field becomes

$$\bar{p}^{m+1} = \bar{p}^{m} + \omega p^{+} \tag{3.9}$$

The value of ω was set to 0.25 in all cases reported here. Values greater than this caused divergence. This value also seemed to result in the greatest convergence rate.

Extension to Unsteady Flows

As stated earlier, the present formulation originated as a solver for steady flows. For the present study, an unsteady formulation was required. It was believed that the iterative space-marching procedure could be used as a base from which to develop this unsteady solution procedure, the spatial sweeps being applied to converge the solution at each time step.

At each time level the procedure is exactly as described above. Global sweeps for the four unknowns are performed with the pressure correction backsweep applied between each spatial iteration. The solution is checked for convergence after each global iteration is complete until the change is sufficiently small. The time level is then incremented. The solution from the previous time step is used as the initial guess at the new time. The change in the temporal solution is also monitored and can be used to terminate the calculation for problems which evolve to a steady state.

CHAPTER 4. NUMERICAL SOLUTION

The discretization and solution of the resulting algebraic equations for the governing conservation laws are described in this chapter. The computational grid is described. The finite differencing of the momentum, energy, and continuity equations is explained. Various boundary conditions are addressed, and the method of solving the system of equations is described. The global pressure correction procedure is also presented in detail.

Computational Grid

In order to apply the finite-difference methods, the continuous flow field (see Figure 2.1) is divided up into discrete, four-sided cells. The flow variables are approximated at each corner of these cells. The cells are made up of lines of constant ξ, and η which form the body-fitted mesh. The (i,j) indices correspond to the respective constant (ξ,η) mesh lines.

Grid spacing, skewness and aspect ratio directly influence the accuracy, stability and consistency of the finite-difference methods. It is desirable to concentrate nodes in regions of large gradients. The body-fitted mesh provides for this while maintaining uniform spacing in the computational space. The code employs a generalized coordinate transformation which permits a non-orthogonal grid. This allows more

flexibility in grid construction than a strictly orthogonal mesh. Equations solved on highly skewed grids can become ill-conditioned. However, a moderately skewed, non-orthogonal mesh can often give a better node distribution for arbitrary geometries.

Symmetric H- and C-type grid topologies were successfully applied. The space-marching direction (ξ direction) was aligned as much as possible with the primary flow direction in both cases. Grid lines of constant ξ were fitted approximately normal to the primary flow streamlines and are termed "stations". Thus, in the case of an H-grid, the initial marching station $\xi = \xi_{start} = constant$ line coincides with the upstream boundary, whereas for a C-grid, it is the geometric line of symmetry connecting the body surface with the upstream boundary — this is also the stagnation streamline. The $\xi = \xi_{max} = constant$ ($i = i_{max}$ station) surface is always located at the outflow boundary. The η_{max} ($j = j_{max}$) surface defines the side boundary for the H-grid. In the case of the C-grid, it conforms to both the upstream and side boundaries. For either grid type, the line of symmetry coincides with the η_{min} ($j = 1$) line.

Full C-grid calculations were made, but attempts to compute flows that were not symmetric failed. It is also not clear if the present method will work for flows in which the location of the stagnation point is unknown.

There are many techniques for generating the interior mesh points (see, for example, Thompson et al. 1985). The Cartesian H-grids used in this study were generated using the stretching functions found in Anderson et al. (1984) and presented in Appendix B. The C-grids were constructed using GRAPE (Sorenson 1980). To minimize errors in the numerical solution, the following conditions were imposed on the generation of the body-fitted coordinates:

1. Physical boundaries were fit by surfaces upon which one of the computational coordinates was constant.

2. The computational coordinates were scaled to produce a uniform mesh ($\Delta\xi = \Delta\eta = 1$).

3. Orthogonality on body surfaces was achieved as much as was practical. For the flat plate, the grid was Cartesian. The C-grid used for most of the results in this work on the cylinder for steady flow varied up to about 5 degrees from orthogonal on the rear (downstream portion) of the cylinder where orthogonality was most difficult to achieve.

4. Grid skewness and grid aspect ratio were limited, although not formally minimized.

The Cartesian coordinates, (x, y), of the node points do not appear explicitly in the transformed equations. They are used only to evaluate the metric terms. Definitions of the metrics and the Jacobian of the transformation are given in Appendix A. The metrics were calculated using finite-difference expressions. These are also found in Appendix A. In practice, they were calculated and stored as one of the first steps in the program.

Finite-Difference Equations

The algorithm began as a steady, space marching scheme (TenPas and Pletcher 1987). The present work includes the addition of time terms. The original space-marching iterations were used as sub-iterations to converge the solution at each time

step. All values in the equations were evaluated at the new time level. However, the option of strictly space-marching was maintained, and the steady results shown were calculated using this mode of operation.

The fundamental step in the space-marching procedure is to advance the solution of the governing equations from a given station i, to the next station, $i+1$. Described in this section is the formulation of the coupled, implicit, finite-difference equations for the unknown variables, $\bar{q}^m$, at station $i+1$. With the space-marching method, the newly computed profiles of $\bar{q}^m$ at and upstream of station i appear explicitly, and assumed or lagged values of $\bar{q}^{m-1}$ at station $i+2$ and downstream locations are required. The values at station $i+1$ are implicit and are updated using Newton iteration.

As described in Chapter 2, the transformed governing equations may be cast in several forms. The chain-rule conservation-law form is used for the momentum and energy equations, and the strong conservation-law (control-volume) form is used for the continuity equation. The numerical properties of the different forms and the reasons for selecting this combination follow.

The finite-difference representations in the strong conservation-law form may be constructed such that the assembled set of equations is globally conservative. This property holds even on coarse grids, where the derivatives are not accurately approximated. The truncation errors in the equations for adjacent nodes cancel, so that the summation of all of the difference equations is identical to numerical integration over the surface of the entire flow domain. With the chain-rule conservation-law form, products of truncation errors and finite gradients, in general, do not cancel. Global conservation is satisfied within reasonable accuracy, since the truncation errors vanish

for any consistent difference method as the grid is refined.

The geometric considerations associated with these forms have been explored by Hindman (1982). With the strong conservation-law form, the metrics must be evaluated consistently with the particular finite-difference formulation used. Otherwise, numerical source terms arise due to truncation errors in the metrics. There are no such constraints on the metrics for the chain-rule conservation-law form.

Upwind differencing in the momentum and energy equations requires that the finite-difference expressions vary from node to node. With the strong conservation-law form it is time-consuming to adjust the differencing and preserve a globally conservative set of equations since correct representation of the type-dependent terms would require many different evaluations of the metrics. With the use of the chain-rule conservation-law form, constraints on the metric terms are avoided. Although truncation errors can be significant on coarse grids, a global momentum and energy balance is achieved as the grid is refined. No such type-dependent terms appear in the continuity equation. Since the calculation of the metrics is thus simplified, to guarantee conservation of mass on coarse grids independent of truncation errors, the strong conservation-law form is used for the continuity equation. The special requirements imposed on the metric terms produce an algebraic equation that is identical to the finite-volume continuity equation in physical coordinates.

The details of the finite-difference form of the momentum, energy, and continuity equations comprise the following sub-sections. In the marching direction (ξ-direction), the flux terms are strictly upwinded in the momentum and energy equations. For the transverse flux terms, a weighted average between central and upwind is used. The weighting is calculated to maintain stability.

Special consideration was required for the transverse pressure derivatives in the momentum equations. They were forward differenced in all the cases run for this study. The first-order representation of these pressure derivatives appears implicitly. They are corrected to second order explicitly.

The one-sided differences, in both directions, reduce the problem of decoupling every-other node which can occur with central differences.

Momentum equations

The momentum equations in the chain-rule conservation-law form (Equation 2.1) are expanded as finite-differences in the computational domain about the node located at $(i+1, j)$. The differencing method employed for each of the terms within the flux vectors $\overline{E}$ and $\overline{F}$ is described below and summarized in Table 4.1. The finite-difference molecules at node $(i+1, j)$ are shown schematically in Figure 4.1. The open circles represent known values at the present spatial sweep, the solid circles show the nodes which are implicit, and the crosses indicate where lagged values are used. The open circle with the cross within is an explicit point which is updated through the Newton iterations since it would appear outside the coefficient matrix bandwidth. The molecule on the left shows the points used in descretizing the flux and diffusion terms, the one on the right depicts the configuration for the pressure derivatives.

The point of interest is at $(i+1, j)$. The example difference formulas given below are all expanded about that node.

Table 4.1: Summary of the finite-difference representations used in the momentum equations

Derivative	Type	Direction	Order
ξ	pressure	forward	1
η	pressure	forward	1
ξ	diffusion	central	2
η	diffusion	central	2
Cross	diffusion	central	2
ξ	convection	upwind	2
η	convection	hybrid	1-2

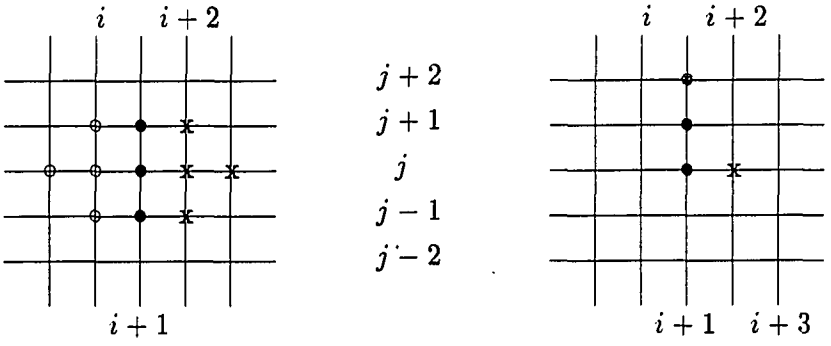

Figure 4.1: Finite-difference molecules

Temporal terms Time terms were added to the original space-marching algorithm. Because only the main diagonal of the coefficient matrix is affected on the implicit side, diagonal-dominance is enhanced. Therefore, a false time parameter may be introduced for steady flow cases. The result is a more stable algorithm.

The finite-difference form of the temporal derivatives in the x- and y-momentum equations, respectively, are as follows

$$\begin{aligned} \frac{\partial \rho u}{\partial t} &= \frac{(\rho u)^{n+1}_{i+1,j} - (\rho u)^{n}_{i+1,j}}{\Delta t} \\ \frac{\partial \rho v}{\partial t} &= \frac{(\rho v)^{n+1}_{i+1,j} - (\rho v)^{n}_{i+1,j}}{\Delta t} \end{aligned} \tag{4.1}$$

Linearization of the implicit (at time $n+1$) terms, is carried out in exactly the same manner as the flux terms in the continuity equation.

$$\begin{aligned} \rho u &= [\hat{\rho}]u + [0]v + [\frac{\hat{u}}{R\hat{T}}]p + [0]S - [\hat{\rho}\hat{u}] \\ \rho v &= [0]u + [\hat{\rho}]v + [\frac{\hat{v}}{R\hat{T}}]p + [0]S - [\hat{\rho}\hat{v}] \end{aligned}$$

The terms with the caret are the linearized coefficients. They are updated through the Newton iteration at each marching station. Contained in Appendix C is a complete list of linearized variables.

Streamwise pressure gradient terms The streamwise pressure gradient is strictly forward-differenced. The results presented in this work were obtained with a first-order representation, although a second-order accurate expression has also been coded. Downstream pressure values are estimated values (denoted with an overbar), resulting from the pressure Poisson correction procedure following the previous global

sweep. The first-order accurate, forward-difference formula at $(i+1,j)$ is

$$p_\xi = \frac{\bar{p}^m_{i+2,j} - p^m_{i+1,j}}{\Delta\xi} \tag{4.2}$$

And the second-order accurate, forward-difference formula is

$$p_\xi = \frac{-\frac{1}{2}\bar{p}^m_{i+3,j} + 2\bar{p}^m_{i+2,j} - \frac{3}{2}p^m_{i+1,j}}{\Delta\xi} \tag{4.3}$$

Transverse pressure gradient terms Central-differencing of the transverse pressure gradient can cause the even and odd node pressures to decouple, resulting in a saw-toothed profile. Instead of adding dissipation to smooth this out, second-order accurate, one-sided differences were used to link the pressures at neighboring nodes. These three-point difference formulas include nodes outside of the bandwidth of a block-tridiagonal solver. Rather than use a pentadiagonal solver, the difference formula was split into an implicit, first-order accurate term plus an explicit, second-order correction. Thus, on convergence the solution is second-order. The direction chosen for the one-sided difference depends upon the side boundary condition. As an example, the second-order accurate (on convergence), forward-difference formula in the η direction for the node located $(i+1,j)$ is

$$p_\eta = \frac{p^m_{i+1,j+1} - p^m_{i+1,j}}{\Delta\eta} - \frac{\hat{p}^m_{i+1,j+2} - 2\hat{p}^m_{i+1,j+1} + \hat{p}^m_{i+1,j}}{2\Delta\eta} \tag{4.4}$$

The values with the carots are updated within the Newton-linearization iterations. In this work, a forward difference was used exclusively.

Viscous stress terms Second-order accurate, central-differences are used to approximate the derivatives in the viscous terms. The chain-rule expansion of the

viscous terms is given in Appendix D. First and second-derivatives of the velocity components appear in these terms, as well as first-derivatives of the metrics and viscosity. The viscosity is determined from the current estimate of the temperature, using Sutherland's law, which allows the viscosity and metrics together to be used as linear coefficients.

The transverse second-derivatives and the associated first-derivatives are treated implicitly. The method may be illustrated with an example term in the η direction of the form,

$$(a^t u_\eta)_\eta = a^t u_{\eta\eta} + a^t_\eta u_\eta \tag{4.5}$$

where the coefficient, a^t, is a function of the metrics and the viscosity. The complete term can be written in implicit form as:

$$(a^t u_\eta)_\eta \approx (A^t + A^t_1)u^m_{i+1,j+1} - 2A^t u^m_{i+1,j} + (A^t - A^t_1)u^m_{i+1,j-1} \tag{4.6}$$

Where the implicit coefficients are evaluated by

$$A^t = \frac{a^t_{i+1,j}}{(\Delta\eta)^2} \qquad A^t_1 = \frac{a^t_{i+1,j+1} - a^t_{i+1,j-1}}{4(\Delta\eta)^2}$$

Equation 4.6 is obtained by expanding the derivatives in Equation 4.5 with central-differences about the location $(i+1, j)$ as:

$$u_{\eta\eta} = \frac{u^m_{i+1,j+1} - 2u^m_{i+1,j} + u^m_{i+1,j-1}}{(\Delta\eta)^2} \tag{4.7}$$

$$a^t_\eta = \frac{a^t_{i+1,j+1} - a^t_{i+1,j-1}}{2\Delta\eta} \tag{4.8}$$

$$u_\eta = \frac{u^m_{i+1,j+1} - u^m_{i+1,j-1}}{2\Delta\eta} \tag{4.9}$$

The streamwise second-derivatives and the associated first-derivatives are handled in much the same way, except known upstream values, lagged downstream values, and implicit values at the marching station are used. An example term of the form

$$(a^s u_\xi)_\xi = a^s u_{\xi\xi} + a^s_\xi u_\xi \tag{4.10}$$

expanded at the node located at $(i+1, j)$ can be written as

$$(a^s u_\xi)_\xi \approx (A^s + A^s_1) u^{m-1}_{i+2,j} - 2A^s u^m_{i+1,j} + (A^s - A^s_1) u^m_{i,j} \tag{4.11}$$

Where central-differences are used for the streamwise derivatives and the implicit coefficients are evaluated by:

$$A^s = \frac{a^s_{i+1,j}}{(\Delta\xi)^2} \qquad A^s_1 = \frac{a^s_{i+2,j} - a^s_{i,j}}{4(\Delta\xi)^2}$$

Example forms of the mixed partial-derivative terms are:

$$(a^c u_\eta)_\xi = a^c u_{\xi\eta} + a_\xi u^c_\eta \tag{4.12}$$

and

$$(a^c u_\xi)_\eta = a^c u_{\xi\eta} + a_\eta u^c_\xi \tag{4.13}$$

The explicit central-difference form of Equations 4.12 is

$$\begin{aligned} (a^c u_\eta)_\xi \;\approx\; & [A^c u^{m-1}_{i+2,j+1} - A^c u^{m-1}_{i+2,j-1} - A^c u^m_{i,j+1} \\ + \; & A^c u^m_{i,j-1} + A^c_1 u^{m-1}_{i+1,j+1} - A^c_1 u^{m-1}_{i+1,j-1}] \end{aligned} \tag{4.14}$$

Where the coefficients are evaluated by:

$$A^c = \frac{a^c_{i+1,j}}{4\Delta\xi\Delta\eta}$$

$$A_1^c = \frac{a^c_{i+2,j} - a^c_{i,j}}{4\Delta\xi\Delta\eta}$$

Equation 4.13 appears similar.

The mixed-derivatives used to expand Equations 4.12 and 4.13 at $(i+1,j)$ are:

$$u_{\xi\eta} = \frac{u^{m-1}_{i+2,j+1} - u^{m-1}_{i+2,j-1} - u^{m}_{i,j+1} + u^{m}_{i,j-1}}{4\Delta\xi\Delta\eta} \tag{4.15}$$

$$a^c_{\xi} = \frac{a^c_{i+2,j} - a^c_{i,j}}{2\Delta\xi} \tag{4.16}$$

$$u_{\eta} = \frac{u^{m-1}_{i+1,j+1} - u^{m-1}_{i+1,j-1}}{2\Delta\eta} \tag{4.17}$$

Streamwise convection terms The differencing direction for the streamwise convective terms is strictly upwind. For accuracy, the second-order upwind method was used, except adjacent to boundaries. In regions of reversed flow the direction of the differencing was reversed, and the convective flux terms at the downstream nodes are lagged. Examples of the second-order accurate difference operators used for the node located at $(i+1,j)$ are:

For $U > 0$:

$$(\rho u^2)_{\xi} = \frac{3(\rho u^2)^m_{i+1,j} - 2(\rho u^2)^m_{i,j} + (\rho u^2)^m_{i-1,j}}{2\Delta\xi} \tag{4.18}$$

For $U < 0$:

$$(\rho u^2)_{\xi} = \frac{-3(\rho u^2)^m_{i+1,j} + 2(\rho u^2)^{m-1}_{i+2,j} - (\rho u^2)^{m-1}_{i+3,j}}{2\Delta\xi} \tag{4.19}$$

Where: $U = (\hat{u}^m\xi_x + \hat{v}^m\xi_y)_{i+1,j}$ and is updated through Newton iteration. Note that the term evaluated at $(i+1,j)$ must be linearized since it is treated implicitly. See Appendix C for details of the linearization.

Transverse convection terms A hybrid differencing scheme is used for the transverse convective terms, formulated with a weighted average of central and upwind differences. Central differences were used whenever feasible. Possible instability was controlled by progressively weighting the differencing in the upwind direction to suppress the appearance of positive, off-diagonal coefficients. The criteria used to set the weighting is explained below. Although in the limit of upwinding, the formal accuracy was reduced to first-order, the type-dependency improves the physical representation of the combined convection-diffusion terms. As an example, the transverse convection terms in the η direction from the x-momentum equation are:

$$(\rho u^2)_\eta \eta_x + (\rho uv)_\eta \eta_y \tag{4.20}$$

The metrics are evaluated at $(i+1, j)$. Approximating the convective derivatives about the location $(i+1, j)$ with the hybrid scheme, and linearizing gives the following implicit terms for the u velocity component:

$$fC_{j+1} u^m_{i+1,j+1} + (b-f) C_j u^m_{i+1,j} - bC_{j-1} u^m_{i+1,j+1} \tag{4.21}$$

The linearized coefficients are evaluated at each node. For purposes of clarity, the frozen coefficient expressions are:

$$C_{j+1} = \frac{\eta_x (\hat{\rho}\hat{u})_{i+1,j+1} + \eta_y (\hat{\rho}\hat{v})_{i+1,j+1}}{\Delta\eta}$$

$$C_j = \frac{\eta_x (\hat{\rho}\hat{u})_{i+1,j} + \eta_y (\hat{\rho}\hat{v})_{i+1,j}}{\Delta\eta}$$

$$C_{j-1} = \frac{\eta_x (\hat{\rho}\hat{u})_{i+1,j-1} + \eta_y (\hat{\rho}\hat{v})_{i+1,j-1}}{\Delta\eta}$$

The forward and backward difference weight factors, f and b, are determined by testing the implicit convective term coefficients against the coefficients of the implicit

viscous terms defined in Equation 4.6. Notice that the viscous coefficients are non-positive, and that for central-differencing the weights, f and b, are both equal to one-half. The conditions that are satisfied are:

For $f = 1/2$: if $[(A^t + A_1^t) + fC_{j+1}] > 0$, then shift toward backward differencing. Thus:

$$f = \frac{-(A^t + A_1^t)}{C_{j+1}}$$

and

$$b = 1 - f$$

For $b = 1/2$: if $[(A^t - A_1^t) - bC_{j-1}] > 0$, then shift toward forward differencing. Thus:

$$b = \frac{(A^t - A_1^t)}{C_{j-1}}$$

and

$$f = 1 - b$$

Otherwise: use central differencing. Thus:

$$f = b = \frac{1}{2}$$

To illustrate the upwind adjustment, the η direction example begun above is continued here. The implicit viscous terms on u in the η direction for the x-momentum equation given in Appendix D are:

$$\eta_x[\mu\eta_x u_{\eta\eta} + (\mu\eta_x)_\eta u_\eta] + \eta_y[\mu\eta_y u_{\eta\eta} + (\mu\eta_y)_\eta u_\eta] \tag{4.22}$$

These terms correspond to the form of Equation 4.5. The implicit coefficients, A^t and A_1^t, are then obtained from Equation 4.6. For the example term of Equation 4.22

the coefficients needed to determine the hybrid weight factors used in example Equation 4.21 are:

$$A^t = \frac{[\mu(\eta_x^2 + \eta_y^2)]_{i+1,j}}{(\Delta\eta)^2} \tag{4.23}$$

$$A_1^t = \frac{\eta_x[(\mu\eta_x)_{i+1,j+1} - (\mu\eta_x)_{i+1,j-1}] + \eta_y[(\mu\eta_y)_{i+1,j+1} - (\mu\eta_y)_{i+1,j-1}]}{4(\Delta\eta)^2} \tag{4.24}$$

Where the metrics are evaluated at $(i+1, j)$, except as indicated otherwise.

Continuity equation

The discretized form of the continuity equation is derived from the strong conservation-law form of the governing equations (Equation 2.10). It is expanded in finite-volume form about the mesh location $(i+1/2, j)$ to give

$$\frac{\rho_e^{n+1} - \rho_e^n}{\Delta t} + \frac{(E_e' - E_w')^{n+1}}{\Delta\xi} + \frac{(F_n' - F_s')^{n+1}}{\Delta\eta} = 0 \tag{4.25}$$

Here the subscripts denote the faces of the resulting control volume as shown in Figure 4.2. Substitution for the fluxes defined for Equation 2.10, and canceling $\Delta\xi = \Delta\eta$ gives

$$\frac{\rho_e^{n+1} - \rho_e^n}{\Delta t} + \frac{(\rho U)_e^{n+1}}{J} - \frac{(\rho U)_w^{n+1}}{J} + \frac{(\rho V)_n^{n+1}}{J} - \frac{(\rho V)_s^{n+1}}{J} = 0 \tag{4.26}$$

where the contravariant velocities are

$$U = \xi_x u + \xi_y v, \qquad V = \eta_x u + \eta_y v$$

To ensure global and local conservation of mass in spite of truncation errors, several conditions are imposed on the set of difference equations. To satisfy global conservation the assembled control volumes must fill the physical space, and the

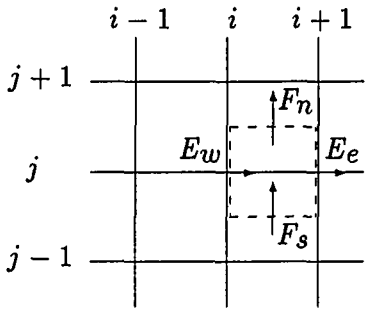

Figure 4.2: Continuity control volume

common fluxes of neighboring cells must be identical. To be locally conservative, the calculated face areas must form closed control volumes. The first condition is easily met by assigning a control volume to each node. The other two conditions restrict the interpolation of the fluxes and the evaluation of the metrics as discussed below. By satisfying these conditions, the transformed difference equation is algebraically equivalent to numerically integrating the finite-volume continuity equation in physical coordinate form.

Temporal term Consistent with the flow equations (continuity and momentum), the thermal variable is lagged in the time derivative term. Density is therefore replaced by $\frac{p}{R\hat{T}}$ and only the pressure appears implicitly. An attempt was made to average the density at the east and west nodal points, but this caused a saw-toothed pressure profile. The solution was to approximate the density in the control volume by that at the east face, as indicated above.

Cell face center-point flux interpolation The east and west face fluxes are obtained directly at the nodes $(i+1,j)$ and (i,j) in the center of these faces. However, the fluxes at the centers of the top and bottom faces must be interpolated. Simple averaging among the four neighboring nodes leads to a central-difference expression that causes even/odd decoupling and produces saw-tooth profiles. To suppress this, the interpolation is done by a Taylor-series expansion biased to one side of the control volume center. Second order accuracy is maintained, but some dissipation error is introduced into the equation. For example, the east face flux terms at the location $(i+1/2, j+1/2)$ are determined from the properties and gradients about the node at $(i+1,j)$ as

$$(\rho u)_n = (\rho u)_{i+1,j} + \left[\frac{\Delta\eta}{2}\frac{\partial \rho u}{\partial \eta}\right]_{i+1,j} - \left[\frac{\Delta\xi}{2}\frac{\partial \rho u}{\partial \xi}\right]_{i+1,j} \tag{4.27}$$

$$(\rho v)_n = (\rho v)_{i+1,j} + \left[\frac{\Delta\eta}{2}\frac{\partial \rho v}{\partial \eta}\right]_{i+1,j} - \left[\frac{\Delta\xi}{2}\frac{\partial \rho v}{\partial \xi}\right]_{i+1,j} \tag{4.28}$$

The derivatives were approximated with one-sided, first-order accurate differences. The streamwise derivative is always backward-differenced. The transverse derivative direction is opposite to that of the transverse pressure gradient in the momentum equations. To maintain a band-width of three, the correction terms are explicit. These explicit terms, indicated below with a caret, are lagged within the nonlinear coefficient loop. As an example, one of the north face terms is

$$(\rho v)_n = (\rho v)^m_{i+1,j} + \frac{(\hat{\rho}\hat{v})_{i+1,j} - (\hat{\rho}\hat{v})_{i+1,j-1}}{2} - \frac{(\hat{\rho}\hat{v})_{i+1,j} - (\hat{\rho}\hat{v})_{i-1,j}}{4}$$

The south face flux at $(i+1/2, j-1/2)$ is determined similarly about the adjacent node at $(i+1, j-1)$. For example, the corresponding south face term is

$$(\rho v)_s = (\rho v)^m_{i+1,j-1} + \frac{(\hat{\rho}\hat{v})_{i+1,j-1} - (\hat{\rho}\hat{v})_{i+1,j-2}}{2} - \frac{(\hat{\rho}\hat{v})_{i+1,j-1} - (\hat{\rho}\hat{v})_{i-1,j-1}}{4}$$

The underlying requirement is that the south face flux from the cell associated with the node $(i+1, j)$ be identical to the north face flux into the neighbor cell assigned to the node $(i+1, j-1)$. This can be verified by careful examination of the indexes in the equations above and by reference to Figure 4.2.

All terms evaluated at the $(i+1)$ marching station, except those which arise from the interpolation are treated implicitly. Since these terms are nonlinear, they must be linearized. Details of the linearization are given in Appendix C.

Control volume face areas The metric terms for each of the flux represent the face areas of the control volume. In order to ensure strict flux conservation the metrics must satisfy the geometric conservation law. Otherwise the control volume would not be closed, and a uniform velocity field would not satisfy the discretized continuity equation. Therefore, the metrics are evaluated for each different face, using the physical coordinates of the corner points of the control volume. This treatment of the metrics exactly fits the projected areas of the physical control volume faces. As an example, the projected area of the east face onto a line parallel to the x axis is given by

$$(\frac{\eta_y}{J})_e = (x_\xi)_e = \frac{(x_{i+1,j+1} + x_{i+1,j}) - (x_{i+1,j} + x_{i+1,j-1})}{2} \tag{4.29}$$

Energy equation

The energy equation was formulated much the same as the momentum equations (see Figure 4.1). The chain-rule-conservation-law form was used. The streamwise flux terms were strictly upwinded. For the transverse flux terms, a hybrid of central and upwind differencing was used to avoid change of sign of off-diagonal terms.

A minor change from the momentum equation formulation was incorporated for the diffusion terms. The product rule for differentiation was not utilized before finite-differencing. Rather, the products of metrics and thermal conductivity were averaged and differenced along with the thermal variable. It was felt that this was more consistent with the spirit of the conservation law. The method used in the momentum equations resulted in a first derivative of velocity. A central difference used on this term has the potential to adversely affect the diagonal dominance of the system. This problem does not appear with the method used for the energy equation.

There is no counterpart of dissipation in the momentum equations. These terms are handled in the same manner as the diffusion terms. For most of the flows of interest in this study, these terms were of little consequence. Therefore, they were treated explicitly.

Thermal variable There are several possible choices of thermal variable. For instance, use of the dimensionless total or static enthalpy, or temperature are valid options. Because the energy equation was cast in chain-rule conservation-law form, it was found necessary to use a thermal variable which was small in regions of large gradients (near the wall). This is explained below.

The problem arose due to the different formulations of the continuity and energy equations. It can be seen that the temporal and convective terms of the energy equation contain all of the elements of the continuity equation multiplied by the thermal variable. These terms should have summed to zero. However, due to the inaccuracies introduced by the chain-rule conservation-law form, the sum was, in fact, finite. This resulted in incorrect temperature fields. Since the inaccuracies were only

significant in the regions of large gradients of the mass flux terms, the choice of a thermal variable which became small in these regions solved the problem.

For this reason, the thermal variable selected was

$$S = \frac{T - T_{surf}}{T_r - T_{surf}}$$

Temporal terms The time derivative that appears in the energy equation is slightly more complicated than those in the other equations, in that it contains more terms. It appears thus:

$$\frac{\partial}{\partial t}\left[\rho\left(c_p S + \frac{u^2+v^2}{2(T_r - T_{surf})} - \frac{p}{\rho(T_r - T_{surf})}\right)\right] \tag{4.30}$$

In practice, density is lagged here between global sweeps, but updated through the Newton iterations. This is because the combination, ρS becomes a function of pressure only, using the ideal gas law. Thus the thermal variable, S would not appear in the time derivative.

The term $(T_r - T_{surf})$ is a constant for all cases considered here. Therefore, only the kinetic energy term requires linearization. This was accomplished as follows:

$$u^2 = [2\hat{u}]u - \hat{u}\hat{u}, \qquad v^2 = [2\hat{v}]v - \hat{v}\hat{v}$$

The differencing of Equation 4.30 is simply

$$\frac{\hat{\rho}^{n+1}_{i+1,j}\left[c_p S^{n+1}_{i+1,j} + \frac{(u^2)^{n+1}_{i+1,j}+(v^2)^{n+1}_{i+1,j}}{2(T_r - T_{surf})} - \frac{p^{n+1}_{i+1,j}}{\hat{\rho}^{n+1}_{i+1,j}(T_r - T_{surf})}\right]}{\Delta t}$$
$$- \frac{\hat{\rho}^{n}_{i+1,j}\left[c_p S^{n}_{i+1,j} + \frac{(u^2)^{n}_{i+1,j}+(v^2)^{n}_{i+1,j}}{2(T_r - T_{surf})} - \frac{p^{n}_{i+1,j}}{\rho^{n}_{i+1,j}(T_r - T_{surf})}\right]}{\Delta t} \tag{4.31}$$

where the linearization of the kinetic term at the newest time is applied, and all linearized coefficients are updated by Newton linearization.

A second-order, three-point version of this derivative is coded as an option.

Thermal diffusion terms As with the viscous stress terms in the momentum equations, second-order accurate, central-differences were used to approximate the derivatives in the thermal diffusion terms. The conductivity is determined from the current estimate of the temperature, using the viscosity and Prandtl number, which allows the conductivity and metrics together to be used as explicit coefficient functions.

The transverse derivatives were treated implicitly. The method may be illustrated with an example term in the η direction. The term appears as $(\lambda S_\eta)_\eta$. The coefficient, λ, is a function of the metrics and the conductivity. The complete term can be written in implicit, finite-difference form as:

$$(\lambda^t S_\eta)_\eta \approx \Lambda^t_{i+1,j+1} S^m_{i+1,j+1} - \Lambda^t_{i+1,j} S^m_{i+1,j} + \Lambda^t_{i+1,j-1} S^m_{i+1,j-1} \tag{4.32}$$

Where the implicit coefficients are evaluated by

$$\begin{aligned} \Lambda^t_{i+1,j+1} &= \frac{\lambda^t_{i+1,j+1} + \lambda^t_{i+1,j}}{2(\Delta\eta)^2} \\ \Lambda^t_{i+1,j} &= \frac{\lambda^t_{i+1,j+1} + 2\lambda^t_{i+1,j} + \lambda^t_{i+1,j-1}}{2(\Delta\eta)^2} \\ \Lambda^t_{i+1,j-1} &= \frac{\lambda^t_{i+1,j} + \lambda^t_{i+1,j-1}}{2(\Delta\eta)^2} \end{aligned} \tag{4.33}$$

Equation 4.33 is obtained by expanding the derivatives of S with central-differences

about the half-node locations $(i+1, j \pm 1)$ as:

$$\begin{aligned}(\lambda^t S_\eta)_{i+1,j+1/2} &= \left[\frac{\lambda^t_{i+1,j+1} + \lambda^t_{i+1,j}}{2}\right] \frac{S^m_{i+1,j+1} - S^m_{i+1,j}}{\Delta\eta} \\ (\lambda^t S_\eta)_{i+1,j-1/2} &= \left[\frac{\lambda^t_{i+1,j} + \lambda^t_{i+1,j-1}}{2}\right] \frac{S^m_{i+1,j} - S^m_{i+1,j-1}}{\Delta\eta}\end{aligned} \tag{4.34}$$

The streamwise derivatives were handled in much the same way, except known upstream values, lagged downstream values, and implicit values at the marching station were used. An example term of the form $(\lambda^s S_\xi)_\xi$ expanded at the node located at $(i+1, j)$ can be written as

$$(\lambda^s S_\xi)_\xi \approx \Lambda^s_{i+2,j} S^m_{i+2,j+1} - \Lambda^s_{i+1,j} S^m_{i+1,j} + \Lambda^s_{i,j} S^m_{i,j} \tag{4.35}$$

Where the coefficients are evaluated by

$$\begin{aligned}\Lambda^s_{i+2,j} &= \frac{\lambda^s_{i+2,j} + \lambda^s_{i+1,j}}{2(\Delta\eta)^2} \\ \Lambda^s_{i+1,j} &= \frac{\lambda^s_{i+2,j} + 2\lambda^s_{i+1,j} + \lambda^s_{i,j}}{2(\Delta\eta)^2} \\ \Lambda^s_{i,j} &= \frac{\lambda^s_{i+1,j} + \lambda^s_{i,j-1}}{2(\Delta\eta)^2}\end{aligned}$$

Example forms of the mixed partial-derivative terms are:

$$(\lambda S_\eta)_\xi \tag{4.36}$$

and

$$(\lambda S_\xi)_\eta \tag{4.37}$$

The explicit central-difference form of Equation 4.36 is

$$(\lambda^c S_\eta)_\xi \approx \Lambda^c_{i+2,j}(S^{m-1}_{i+2,j+1} - S^{m-1}_{i+2,j-1}) - \Lambda^c_{i,j}(S^m_{i,j+1} - S^m_{i,j-1}) \tag{4.38}$$

Where the implicit coefficients are evaluated by:

$$\Lambda^c_{i+2,j} = \frac{\lambda^c_{i+2,j}}{4\Delta\xi\Delta\eta}$$

$$\Lambda^c_{i,j} = \frac{\lambda^c_{i,j}}{4\Delta\xi\Delta\eta}$$

The formula for 4.37 is constructed in identically the same way.

Streamwise convection terms Second-order upwind differencing was used everywhere except adjacent to boundaries. In regions of reversed flow the direction of the differencing was necessarily reversed, and the terms at the downstream nodal points were lagged.

For brevity, let Θ be defined as

$$\Theta = c_p S + \frac{u^2 + v^2}{2(T_r - T_{surf})}$$

Where the thermal variable, S, is defined as

$$S = \frac{T - T_{surf}}{T_r - T_{surf}}$$

An example of the second-order accurate difference operators used for the node located at $(i+1, j)$ is:

For $U > 0$:

$$(\rho u\Theta)_\xi = \frac{3(\rho u\Theta)^m_{i+1,j} - 4(\rho u\Theta)^m_{i,j} + (\rho u\Theta)^m_{i-1,j}}{2\Delta\xi} \tag{4.39}$$

For $U < 0$:

$$(\rho u\Theta)_\xi = \frac{-3(\rho u\Theta)^m_{i+1,j} + 4(\rho u\Theta)^{m-1}_{i+2,j} - (\rho u\Theta)^{m-1}_{i+3,j}}{2\Delta\xi} \tag{4.40}$$

Where: $U = (\hat{u}^m\xi_x + \hat{v}^m\xi_y)_{i+1,j}$ and was updated through Newton iteration. Note that the terms evaluated at $i+1$ must be linearized since they appear implicitly.

Transverse convection terms Hybrid differences were used for the transverse convective terms, in exactly the same manner and for the same reasons as in the momentum equations. Potential instability was controlled by weighting the differencing in the upwind direction to suppress the appearance of positive, off-diagonal coefficients. Formal accuracy was reduced to first-order in the extreme case. As an example, the transverse convection terms in the η direction from the x-momentum equation are:

$$(\rho u\Theta)_\eta \eta_x + (\rho v\Theta)_\eta \eta_y \tag{4.41}$$

The metrics are evaluated at $(i+1, j)$. Representing the coefficients as C, (note that linearization is required within Θ) gives the following implicit terms for the Θ component:

$$fC_{j+1}\Theta^m_{i+1,j+1} + (b-f)C_j\Theta^m_{i+1,j} - bC_{j-1}\Theta^m_{i+1,j+1} \tag{4.42}$$

The linearized coefficients are evaluated at each node. The frozen coefficients on S are

$$\begin{aligned} C_{j+1} &= c_p \frac{\eta_x(\hat{\rho}\hat{u})_{i+1,j+1} + \eta_y(\hat{\rho}\hat{v})_{i+1,j+1}}{\Delta\eta} \\ C_j &= c_p \frac{\eta_x(\hat{\rho}\hat{u})_{i+1,j} + \eta_y(\hat{\rho}\hat{v})_{i+1,j}}{\Delta\eta} \\ C_{j-1} &= c_p \frac{\eta_x(\hat{\rho}\hat{u})_{i+1,j-1} + \eta_y(\hat{\rho}\hat{v})_{i+1,j-1}}{\Delta\eta} \end{aligned}$$

The forward and backward difference weight factors, f and b, are determined by testing the implicit convective term coefficients against the coefficients of the implicit diffusion terms defined in Equation 4.33. Notice that the diffusion coefficients are non-positive, and that for central-differencing the weights, f and b, are both equal to one-half. The conditions that are satisfied are:

For $f = 1/2$: if $[\Lambda^t_{i+1,j+1} + fC_{j+1}] > 0$, then shift toward backward differencing.

Thus:

$$f = \frac{-\Lambda^t_{i+1,j+1}}{C_{j+1}}$$

and

$$b = 1 - f$$

For $b = 1/2$: if $[\Lambda^t_{i+1,j-1} - bC_{j-1}] > 0$, then shift toward forward differencing.

Thus:

$$b = \frac{\Lambda^t_{i+1,j-1}}{C_{j-1}}$$

and

$$f = 1 - b$$

Otherwise: use central differencing. Thus:

$$f = b = \frac{1}{2}$$

To illustrate the upwind adjustment, the η direction example above is continued here. The implicit diffusion terms on S in the η direction are:

$$\eta_x \left(k\eta_x \frac{\partial S}{\partial \eta} \right)_\eta + \eta_y \left(k\eta_y \frac{\partial S}{\partial \eta} \right)_\eta \tag{4.43}$$

These terms correspond to the form of Equation 4.32. The implicit coefficients, Λ^t, are then obtained from Equation 4.33. For the example term of Equation 4.41 the coefficients needed to determine the hybrid weight factors used in example Equation 4.42 are:

$$\Lambda^t_{i+1,j+1} = -\frac{(\eta x)_{i+1,j}}{2\Delta\eta^2}[(k\eta x)_{i+1,j+1} + (k\eta x)_{i+1,j}]$$

$$
\begin{aligned}
&- \frac{(\eta y)_{i+1,j}}{2\Delta\eta^2}[(k\eta y)_{i+1,j+1} + (k\eta y)_{i+1,j}] \\
\Lambda^t_{i+1,j-1} &= -\frac{(\eta x)_{i+1,j}}{2\Delta\eta^2}[(k\eta x)_{i+1,j} + (k\eta x)_{i+1,j-1}] \\
&- \frac{(\eta y)_{i+1,j}}{2\Delta\eta^2}[(k\eta y)_{i+1,j} + (k\eta y)_{i+1,j-1}]
\end{aligned}
\tag{4.44}
$$

Dissipation The fact that a fluid is viscous implies that kinetic energy can be converted to heat through shearing action whenever a velocity gradient is present. For low speed (incompressible) flows, this phenomenon is often negligible. In higher speed flows, however, it may not be trivial.

The description "dissipation terms" as used here includes all terms in the energy equation which involve viscosity. It should be noted that these terms include the so-called "dissipation function" as well as some shear work type terms.

The dissipation terms as shown in Chapter 2 are

$$
\begin{aligned}
\Phi_x &= u\tau_{xx} + v\tau_{xy} \\
\Phi_y &= u\tau_{xy} + v\tau_{yy}
\end{aligned}
\tag{4.45}
$$

The transformed shear stresses were described in Chapter 2. As an example, take the $u\tau_{xx}$ term as shown:

$$
u\tau_{xx} = u\frac{2}{3}\mu\left[2(\xi_x\frac{\partial u}{\partial \xi} + \eta_x\frac{\partial u}{\partial \eta}) - (\xi_y\frac{\partial v}{\partial \xi} + \eta_y\frac{\partial v}{\partial \eta})\right]
$$

The derivatives of u are sufficient to show the discretization. Note that all dissipation terms are explicit. The u derivatives found in $\frac{\partial u\tau_{xx}}{\partial \xi}$ are discretized as

follows

$$\frac{2}{3}\frac{1}{\Delta\xi}\Bigg[2\Bigg((\xi_x\mu u)_{i+1\frac{1}{2},j}\frac{u_{i+2,j}-u_{i+1,j}}{\Delta\xi} - (\xi_x\mu u)_{i+\frac{1}{2},j}\frac{u_{i+1,j}-u_{i,j}}{\Delta\xi}\Bigg) + \Bigg((\eta_x\mu u)_{i+2,j}\frac{u_{i+2,j+1}-u_{i+2,j-1}}{2\Delta\eta} + (\eta_x\mu u)_{i,j}\frac{u_{i,j+1}-u_{i,j-1}}{2\Delta\eta}\Bigg)\Bigg] \tag{4.46}$$

Where the terms evaluated between nodes are arithmetic averages of values at adjacent points.

The other derivatives which comprise the dissipation terms are treated in precisely the same manner.

Numerical Boundary Conditions

Several types of boundary conditions exist in the solution domain, as shown in Figure 4.3. Boundary conditions can specify the value of variables at nodes on the boundaries (Dirichlet boundary condition), derivatives of variables (Neumann boundary condition), or the conservation equations may be solved on the boundaries — occasionally modified to account for information across the boundary. At interior nodes adjacent to boundaries, the finite-difference equations may be restricted so that values at locations outside the domain are not needed. For example adjacent to the inlet boundary on an H-grid, the second-order backward-difference formula is replaced by the first-order method. The reduction in accuracy is not significant, since only those gradients that are negligibly small are affected. The specification of conditions at each of the boundaries and the modifications needed in the equations

at nodes adjacent to these boundaries follows.

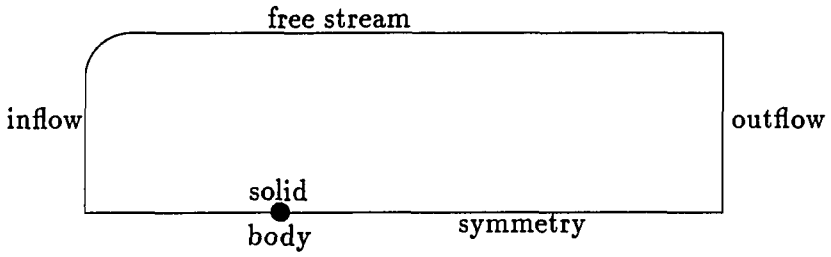

Figure 4.3: Boundary conditions

Upstream boundary conditions

For the upstream boundary, the inlet flow profiles of all the the variables were specified (the pressure is recalculated between iterations; see the section on downstream boundary conditions below). The profiles must be consistent with the desired mass flow, Reynolds number and Mach number. The bulk properties at the inlet, along with the flow field reference length, were used to make the variables dimensionless.

Since the variables were all specified, there is no need to solve the governing equations on the upstream boundary. The equations were solved at the first station inside the boundary. These equations utilize the known conditions at the inlet. Second-order, one-sided differences that would ordinarily use data from two upstream stations were restricted to the first-order method.

For the H-grid, it is notable that the upstream pressure influences the flow so-

lution only through the density, since the streamwise pressure gradient term was forward differenced.

Side boundary conditions

For flow over an isolated body, the side conditions should represent far-field flow. For these isolated bodies, the edge of the grid was located far from the body surface. The streamwise velocity component was explicitly specified equal to the free stream velocity, and the pressure was explicitly specified assuming uniform total pressure. The transverse velocity components were determined implicitly with the specification that the gradient normal to the boundary is zero. The continuity control volumes adjacent to the boundary were extended to reach the boundary.

Solid wall The conditions set on a solid wall were some of the easiest to accommodate. The velocity was set to zero. The pressure on the boundary was calculated such that the pressure gradient normal to the wall, $\frac{\partial p}{\partial n}$, was equal to zero. The temperature on the wall was held constant for all cases reported here — therefore, S was set to zero.

Downstream boundary conditions

The governing equations were solved at the downstream station in the same manner as for interior stations, with the following modifications to the finite-difference equations.

Streamwise and cross derivative diffusion and dissipation terms were assumed to be small compared to the corresponding transverse terms.

For positive streamwise velocity, the streamwise convection terms were unchanged, but if reversed flow was present at the outflow boundary, convection of momentum from downstream was set equal to zero. It was considered important to set the outflow boundary sufficiently downstream of the disturbance so that the flow is not reversed at this boundary. However, during the iteration process, before convergence is achieved, the velocities can often be negative here.

The forward streamwise pressure difference required a known downstream pressure, located one step outside of the grid, which imposes the exit flow pressure field upon the interior flow solution. For flows considered here, this downstream pressure was initially set equal to the free stream pressure. The entire pressure field can be adjusted after each pressure backsweep to maintain a constant inlet pressure. This was accomplished by simply adding a constant value to the pressures at each node point. The value added was calculated such that the inlet pressure would be corrected to the free-stream value. Therefore, the boundary condition for pressure can be considered applied to the upstream boundary. It should be noted that, for the external flows discussed in this work, this correction was negligible.

It is assumed that the downstream boundary is located sufficiently far from any disturbance that the transverse pressure gradients are negligible. Should this not be the case, an appropriate pressure profile must be specified to establish the downstream pressure variation.

Solution of the System of Discretized Equations

To advance the space-marching solution, the finite-difference equations and boundary conditions for all nodes at station $i + 1$ (a line of constant ξ) are assembled into

a system of linearized equations for the primary variables, $\bar{q}^m$. The implicit terms are all located at station $i+1$.

Newton linearization with coupling

The Newton linearization procedure is applied to the nonlinear convective terms in the governing equations. The nonlinear functions are analytically differentiable, allowing the terms to be expanded with the Taylor series about the nodal values from the previous global iteration. Second-order terms are discarded, leaving an expression that is linear in $\bar{q}^m$. Examples of the quasilinearized terms are shown below. The terms with carots are all evaluated using known values. The coefficient on the thermal variable, S in the momentum and continuity equations was zero in all cases for simplicity. This is possible because of the minor effect the temperature has on the flow solution for the cases of interest here.

$$\rho u = \frac{[\hat{p}]u + [0]v + [\hat{u}]p + [0]S - [\hat{u}\hat{p}]}{R\hat{T}} \tag{4.47}$$

$$\rho uv = \frac{[\hat{v}\hat{p}]u + [\hat{u}\hat{p}]v + [\hat{u}\hat{v}]p + [0]S - [2\hat{u}\hat{v}\hat{p}]}{R\hat{T}} \tag{4.48}$$

The linear system is solved using the provisional coefficients. When the solution resulted in a large change in the variables, the quasilinearization was performed about the new values, and the solution was repeated using the updated coefficients. Since the algorithm entails global iteration it was not necessary to converge the nonlinear coefficients to high accuracy during each marching sweep. A table of linearized coefficients is included in Appendix C.

The linear system

The difference equations and boundary conditions at station $i+1$ form a block-tridiagonal system of equations for $\overline{q}^m$. The inclusion of implicit terms in the difference operators given above was restricted to the adjacent nodes in order to preserve the tridiagonal structure. This type of linear system is easily solved by a block elimination procedure, using the routine by Chakravarthy found in Anderson et al. (1984).

Global Pressure Correction Procedure

Methods for correcting the assumed pressure field to accelerate convergence of the global iterations were presented in Chapter 3. The method employing a simple algebraic operation was described in sufficient detail. The finite-difference method of implementing a pressure correction based upon the pressure Poisson equation is described here. The finite-difference form of the transformed Poisson equation will be presented immediately, then manipulations will be performed on that. The assumptions used to parabolize the equation are also presented.

Finite-difference form of the pressure Poisson equation

The momentum equations can be manipulated to describe the pressure field by a Poisson equation in Cartesian coordinates (see Chapter 3). The Laplacian can be transformed to generalized coordinates by introducing the metrics. This looks like

$$(\xi_{xx}+\xi_{yy})\frac{\partial p}{\partial \xi}+(\eta_{xx}+\eta_{yy})\frac{\partial p}{\partial \eta}+(\xi_x^2+\xi_y^2)\frac{\partial^2 p}{\partial \xi^2} \quad +$$

$$(\eta_x^2+\eta_y^2)\frac{\partial^2 p}{\partial \eta^2}+2(\xi_x\eta_x+\xi_y\eta_y)\frac{\partial^2 p}{\partial \xi \partial \eta} \;=\; S_p \qquad (4.49)$$

where the right-hand-side, S_p is constructed from the pressure field which resulted from previous calculations. It is

$$\begin{aligned} S_p &= (\xi_{xx}+\xi_{yy})\frac{\partial \overline{p}}{\partial \xi}+(\eta_{xx}+\eta_{yy})\frac{\partial \overline{p}}{\partial \eta} \\ &+ (\xi_x^2+\xi_y^2)\frac{\partial^2 \overline{p}}{\partial \xi^2}+(\eta_x^2+\eta_y^2)\frac{\partial^2 \overline{p}}{\partial \eta^2}+2(\xi_x\eta_x+\xi_y\eta_y)\frac{\partial^2 \overline{p}}{\partial \xi \partial \eta} \end{aligned}$$

For brevity, the following definitions are made:

$$C_\xi = \xi_{xx}+\xi_{yy}, \qquad C_\eta = \eta_{xx}+\eta_{yy},$$

$$C_{\xi\xi} = \xi_x^2+\xi_y^2, \qquad C_{\eta\eta} = \eta_x^2+\eta_y^2, \qquad C_{\xi\eta} = 2(\xi_x\eta_x+\xi_y\eta_y)$$

The equations can be expressed in more compact form using the differencing operators defined as:

first order -

$$\Delta_\xi(\ )_{i,j} = \frac{(\ )_{i+1,j}-(\ )_{i,j}}{\Delta\xi}$$

and

$$\Delta_\eta(\ )_{i,j} = \frac{(\ )_{i,j+1}-(\ )_{i,j}}{\Delta\eta}$$

second order -

$$\delta_\xi^2(\ )_{i,j} = \frac{(\ )_{i+1,j}-2(\ )_{i,j}+(\ )_{i-1,j}}{\Delta\xi^2}$$

and

$$\delta_\eta^2(\ )_{i,j} = \frac{(\ )_{i,j+1}-2(\ )_{i,j}+(\ )_{i,j-1}}{\Delta\eta^2}$$

Thus Equation 4.49 becomes

$$C_\xi(\bar{p}^m_{i+1,j} - \bar{p}^m_{i,j}) + C_\eta \Delta_\eta \bar{p}^m_{i,j} + C_{\xi\xi}[(\bar{p}^m_{i+1,j} - \bar{p}^m_{i,j}) - (\bar{p}^m_{i,j} - \bar{p}^m_{i-1,j})] \; + \\ C_{\eta\eta}\delta^2_\eta \bar{p}^m_{i,j} + C_{\xi\eta}[(\bar{p}^m_{i+1,j+1} - \bar{p}^m_{i-1,j+1}) - (\bar{p}^m_{i+1,j-1} - \bar{p}^m_{i-1,j-1})] \; = \; S_p \tag{4.50}$$

Where S_p is calculated thus

$$S_p = C_\xi(\bar{p}^{m-1}_{i+1,j} - p^m_{i,j}) + C_\eta \Delta_\eta p^m_{i,j} + C_{\xi\xi}[(\bar{p}^{m-1}_{i+1,j} - p^m_{i,j}) - (\bar{p}^{m-1}_{i,j} - p^m_{i-1,j})] \\ + C_{\eta\eta}\delta^2_\eta p^m_{i,j} + C_{\xi\eta}[(\bar{p}^{m-1}_{i+1,j+1} - p^m_{i-1,j+1}) - (\bar{p}^{m-1}_{i+1,j-1} - p^m_{i-1,j-1})] \tag{4.51}$$

In order for the global iteration cycle to converge, the finite-difference form of this equation must be consistent with the finite-difference form of the momentum equations. This restricts the streamwise derivatives only, since the transverse direction is implicit. Thus $\frac{\partial p}{\partial \xi}$ is forward differenced using a first order, two point difference. The second derivative, $\frac{\partial^2 p}{\partial \xi^2}$ can be considered as $\frac{\partial p_\xi}{\partial \xi}$ and is differenced

$$\frac{\frac{p_{i+1,j} - p_{i,j}}{\Delta\xi} - \frac{p_{i,j} - p_{i-1,j}}{\Delta\xi}}{\Delta\xi}$$

Here the difference for $(p_\xi)_{i+\frac{1}{2},j}$ is consistent with the momentum equations.

Three levels of updated pressures appear in the pressure update equation. An overbar is used to denote the pressure resulting from a pressure backsweep, $\bar{p}^{m-1}$ and $\bar{p}^m$. The superscript indicates the iteration level. The pressure from the previous forward global sweep has only the superscript, $m-1$. Differences in pressure which are used in the equations and actually solved for are defined below.

From Equations 4.50 and 4.51, the "error" in p can be solved for by subtracting

$\bar{p}^{m-1}$ from each of the pressures. To facilitate this, let

$$p^+ = \bar{p}^{m+1} - \bar{p}^m \quad , \qquad \epsilon = p^m - \bar{p}^m$$

Using these definitions in Equation 4.50 and 4.51 results in

$$\begin{aligned} C_\xi(p^+_{i+1,j} - p^+_{i,j}) + C_\eta \Delta_\eta p^+_{i,j} + C_{\xi\xi}[(p^+_{i+1,j} - p^+_{i,j}) - (p^+_{i,j} - p^+_{i-1,j})] \; + \\ C_{\eta\eta}\delta^2_\eta p^+_{i,j} + C_{\xi\eta}[(p^+_{i+1,j+1} - p^+_{i-1,j+1}) - (p^+_{i+1,j-1} - p^+_{i-1,j-1})] \; = \; S_{p+} \end{aligned} \tag{4.52}$$

Where

$$\begin{aligned} S_{p+} \; &= \; -C_\xi \epsilon_{i,j} + C_\eta \Delta_\eta \epsilon_{i,j} - C_{\xi\xi}[\epsilon_{i,j} - \epsilon_{i-1,j}] \\ &+ \; C_{\eta\eta}\delta^2_\eta \epsilon_{i,j} - C_{\xi\eta}[\epsilon_{i-1,j+1} - \epsilon_{i-1,j-1}] \end{aligned}$$

A "stretching" factor is introduced to emphasize the η derivatives over the ξ derivatives. This facilitates "spreading" spikes and errors in the transverse direction. It takes the form of a multiplier, α (greater than one) on the η derivative terms on both sides of the equation. The purpose was to enhance the convergence rate. So

$$\begin{aligned} C_\xi(p^+_{i+1,j} - p^+_{i,j}) + \alpha C_\eta \Delta_\eta p^+_{i,j} + C_{\xi\xi}[(p^+_{i+1,j} - p^+_{i,j}) - (p^+_{i,j} - p^+_{i-1,j})] \; + \\ \alpha C_{\eta\eta}\delta^2_\eta p^+_{i,j} + C_{\xi\eta}[(p^+_{i+1,j+1} - p^+_{i-1,j+1}) - (p^+_{i+1,j-1} - p^+_{i-1,j-1})] \; = \; S_{p+} \end{aligned} \tag{4.53}$$

and

$$\begin{aligned} S_{p+} \; &= \; -C_\xi \epsilon_{i,j} + \alpha C_\eta \Delta_\eta \epsilon_{i,j} - C_{\xi\xi}[\epsilon_{i,j} - \epsilon_{i-1,j}] \\ &+ \; \alpha C_{\eta\eta}\delta^2_\eta \epsilon_{i,j} - C_{\xi\eta}[\epsilon_{i-1,j+1} - \epsilon_{i-1,j-1}] \end{aligned}$$

Various values of α were employed. For the flat plate cases, a value of 100 – 200 was found to be most efficient. For the cylinder, values exceeding 10 tended to cause problems early in the calculation. After some measure of convergence was achieved, or several time steps had been completed, the value could be raised to approximately 100 with an improvement in convergence rate. In no cases was the solution dependent on the value of α.

Parabolizing assumptions As it stands, Equation 4.53 would require an elliptic solver. It is desired to develop a procedure which will quickly carry pressure information from regions downstream to regions upstream with a minimum of computational effort. It is therefore prudent to make assumptions which will allow this to be done in a parabolic manner. The following assumptions were made to allow for this.

$$\bar{p}^m_{i,j} - \bar{p}^m_{i-1,j} = \bar{p}^{m-1}_{i,j} - p^m_{i-1,j}$$
$$\bar{p}^m_{i+1,j+1} - \bar{p}^m_{i-1,j+1} = \bar{p}^{m-1}_{i+1,j+1} - p^m_{i-1,j+1}$$
$$\bar{p}^m_{i+1,j-1} - \bar{p}^m_{i-1,j-1} = \bar{p}^{m-1}_{i+1,j-1} - p^m_{i-1,j-1}$$

or

$$p^+_{i,j} - p^+_{i-1,j} = \epsilon_{i-1,j}$$
$$p^+_{i+1,j+1} - p^+_{i-1,j+1} = \epsilon_{i-1,j+1}$$
$$p^+_{i+1,j-1} - p^+_{i-1,j-1} = \epsilon_{i-1,j-1}$$

These assumptions are not completely arbitrary. They are based on the observation that pressures at a given node are not directly affected by pressures upstream.

Equation 4.53 is now simplified to

$$C_\xi(p^+_{i+1,j} - p^+_{i,j}) + \alpha C_\eta \Delta_\eta p^+_{i,j}$$
$$+ C_{\xi\xi}[(p^+_{i+1,j} - p^+_{i,j})] + \alpha C_{\eta\eta}\delta^2_\eta p^+_{i,j} = S_{p+} \qquad (4.54)$$

and S_{p+} becomes

$$S_{p+} = -C_{\xi}\epsilon_{i,j} + \alpha C_{\eta}\Delta_{\eta}\epsilon_{i,j} - C_{\xi\xi}\epsilon_{i,j} + \alpha C_{\eta\eta}\delta_{\eta}^{2}\epsilon_{i,j}$$

It should be apparent now that only values at and downstream of the station (i, j) are required, not upstream. Thus, this equation can be marched from the downstream boundary to the initial marching station (upstream boundary for an H-grid; the line of geometric symmetry in front of the body for a C-grid).

The pressures on the out-flow boundary are not corrected. The solution advances upstream using a scalar tridiagonal matrix solver at each station. The pressure information is thus rapidly transmitted in this direction.

To maintain a constant upstream pressure value, the pressure field can be adjusted by adding a constant to the pressure at each node point. The pressure gradients are maintained with this method, and the inlet pressure can be specified.

CHAPTER 5. RESULTS

Here some representative results obtained from the space-time marching scheme are presented. Wherever possible, empirical and theoretical results are used for comparison purposes. In some instances, most notably the low Reynolds number cases, experimental data were not available and thus comparisons were made with the numerical results obtained by others. New heat transfer results are presented for the case of the impulsively started cylinder.

Semi-infinite Flat Plate

A simple example was used first to verify the program. Flow over a semi-infinite flat plate is well understood from boundary-layer theory and thus makes a good test run.

Steady flow

A 53×41 H-grid with 28 marching stations upstream of the leading edge was used. Nodes were clustered in regions where high gradients were expected. Algebraic stretching functions found in Anderson et al. (1984) were utilized to accomplish this (see Appendix B for details). To determine the stretching parameter, which dictates the level of clustering in the boundary-layer, the procedure below was followed.

1. The theoretical, laminar boundary-layer thickness was calculated at the outflow boundary.

2. A given number of points were specified (commonly, 20) to reside in this thickness.

3. Newton-Raphson iteration was carried out to solve for the stretching parameter.

A Reynolds number of 100,000, based on the portion of the plate within the computational domain, was used. The Prandtl number was specified as 0.7. Cases with Mach numbers from 0.05 to 0.4 were run successfully. Results shown here are for a Mach number of 0.05.

The plots of Figure 5.1 are representative of the results obtained. The skin friction plotted here is defined as

$$C_f = \frac{\tau_w}{\frac{1}{2}\rho u_\tau^2}$$

where

$$\tau_w = \mu \frac{\partial u}{\partial y}\Big)_w$$

The Nusselt number is the local value, based on the x location along the plate.

The very slight discrepancies in the leading edge region are to be expected since boundary-layer theory does not include leading-edge effects. Also, the present results may have been affected by too few grid points in the viscous region very near the leading edge. The divergence of the plots near the trailing edge is somewhat disconcerting. The solution is apparently affected adversely by the treatment of the boundary conditions. The results overall help to verify that the code is sound.

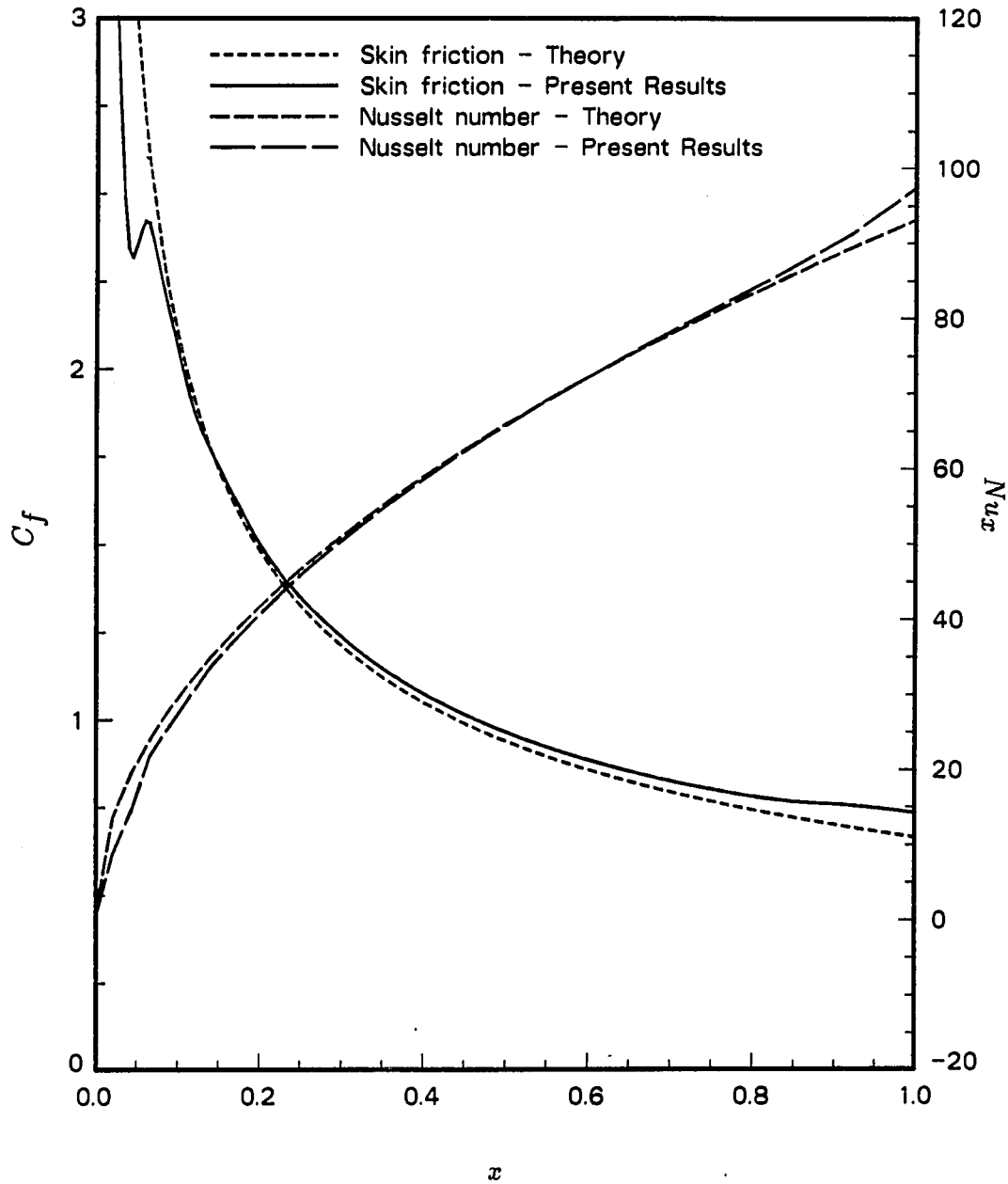

Figure 5.1: Skin friction and local Nusselt number on a flat plate

The velocity and temperature profiles at various locations on the plate are presented in Figures 5.2 and 5.3. In Figure 5.2 the velocity is seen to develop from a very slug-like profile to the characteristic Blasius shape. The Blasius solution is plotted for the largest x location for comparison. The temperature profiles of Figure 5.3 show the growth and development of the thermal boundary-layer. The temperature profile corresponding to the Blasius solution plotted in Figure 5.3 was obtained through numerical integration of the nonlinear ordinary differential Blasius equation along with the corresponding energy equation

$$2\frac{d^3f}{d\eta^3} + f\frac{d^2f}{d\eta^2} = 0$$

$$2\frac{d^2\Gamma}{d\eta^2} + Prf\frac{d\Gamma}{d\eta} = 0$$

with the boundary conditions

$$f(0) = 0, \quad f'(0) = 0, \quad f'(\infty) = 1, \quad \Gamma(0) = 1, \quad \Gamma(\infty) = 0$$

In the above equations, $f' = \frac{u}{u_r}$, $\Gamma = \frac{T-T_r}{T_{surf}-T_r}$, $\eta = y\sqrt{\frac{x}{Re}}$, and the primes indicate differentiation with respect to η.

The calculation ofsteady flow over a flat plate was performed very efficiently by the space-marching scheme. The convergence rate was exceptionally rapid for this case. Only about 20 iterations were required to meet the convergence criterion of $|\epsilon| \leq 10^{-6}$. Approximately 1.6 milliseconds were required per grid point per iteration on a Cray X-MP.

Unsteady flow

The impulsively started flat plate has been presented as a test case for the boundary-layer equations by several researchers (see e.g., Hall 1968, Kwon 1987).

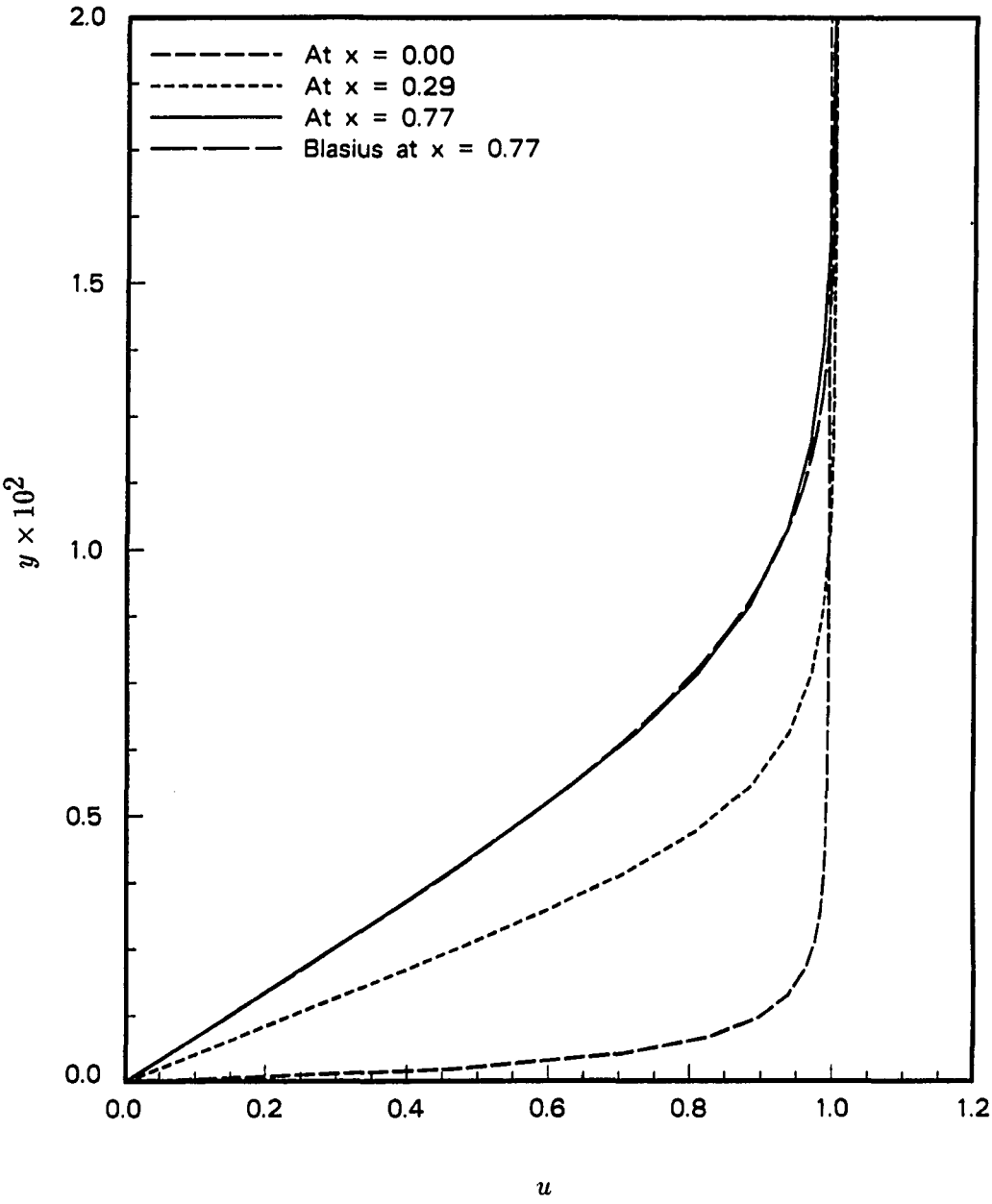

Figure 5.2: Velocity profiles for various locations on a flat plate

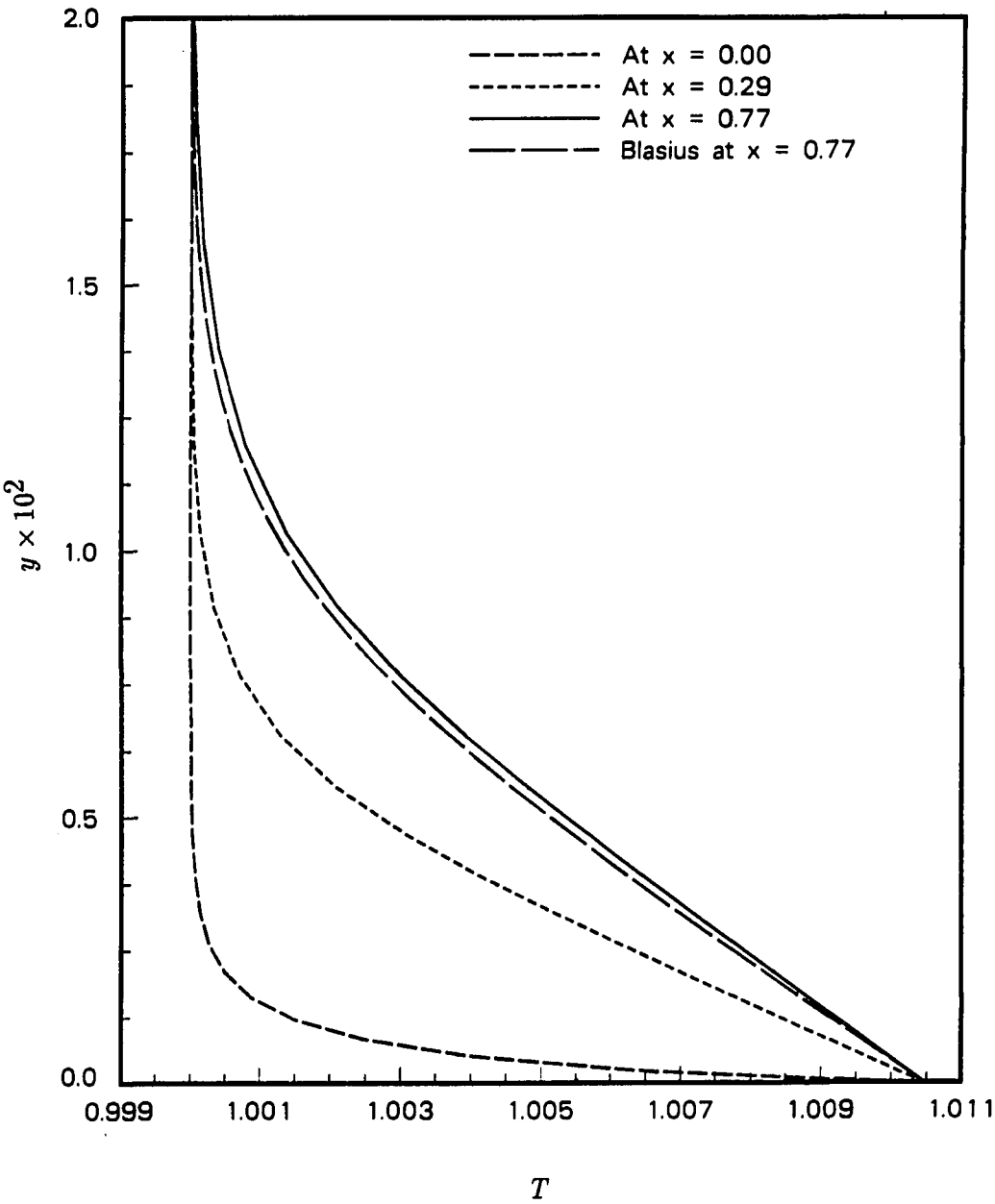

Figure 5.3: Temperature profiles for various locations on a flat plate

This case was computed here to validate the time-marching capabilities.

A 63×64 H-grid was used. Upstream of the leading edge were 28 points. The Cartesian grid was modified to cluster points in regions where large gradients were expected.

A dimensionless time step, $\frac{\tilde{t}}{L_r/u_r}$, of 0.02 was employed. The initial conditions specified represented uniform flow.

As for the steady case, a Reynolds number of 100,000 was used here. The flow was incompressible with a Mach number of 0.1. The Prandtl number was set to 0.7.

Shown in Figure 5.4 are both flow and thermal results. The abscissa is a dimensionless time based on a particular x-location on the plate, $\frac{\tilde{t}}{\tilde{x}/u_r}$. The values on the ordinate were made dimensionless using the same x location. The skin friction plotted here is defined as

$$C_f = \frac{\tau_w}{\rho u_r^2}$$

so that the steady state value, of $C_f\sqrt{Re}$ according to theory, is 0.332. The Reynolds number which is used to normalize each of the ordinate values is based on freestream conditions and the x location on the plate. The numerical results of Ramin (1990) and Watkins (1975) also appear on this plot. Both of these researchers solved the boundary-layer equations in their work.

The results are quite acceptable. It is believed, however, that better accuracy could be achieved through grid refinement.

The present method efficiently handled this case as well. Only one or two subiterations were required at each time step.

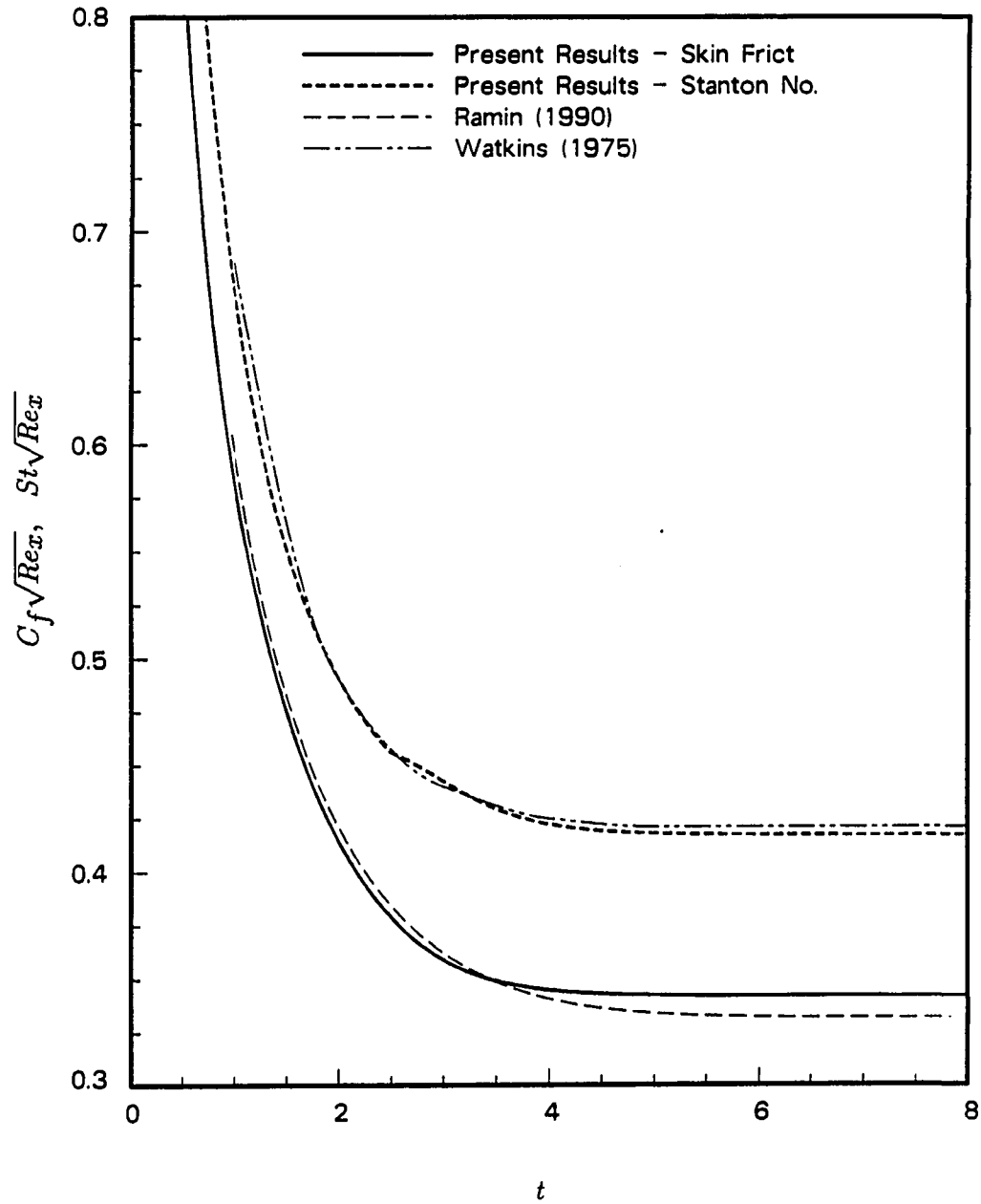

Figure 5.4: Skin friction and Stanton number at a point on an impulsively started flat plate

Right-Circular Cylinder

As a representative blunt body, the right-circular cylinder was chosen. In real flow situations, the Reynolds number limit for steady flow for this geometry is about forty. For Reynolds numbers higher than this, vortices begin to be shed in a periodic (in time) fashion, resulting in an unsteady flow. Numerically however, steady flows can be calculated for much higher Reynolds numbers using the steady equations. While there has been much flow data presented for this geometry over the years (see e.g., Son and Hanratty 1969, Fornberg 1980) there is a noticeable shortage of heat transfer data for low Reynolds numbers.

Steady flow

Most of the results shown in this section are for a Reynolds number (based on diameter) of 40. Results for other Reynolds numbers are also mentioned. The Mach and Prandtl numbers were set to 0.05 and 0.7, respectively, in all cases. The C-grid extended 20 diameters upstream, downstream and to the side of the cylinder. It contained 70 marching stations and 52 points in the transverse direction. Approximately 170 iterations were required to achieve convergence.

Shown in Figures 5.5 – 5.13 are comparisons of the present results with some of the available data from the literature.

The skin friction, shown in Figure 5.5 is defined as:

$$C_f = \frac{\tau_w}{\rho u_\tau^2}$$

where τ_w is the normal derivative of the tangential velocity. As seen in this figure, the present results compare well with theory and boundary-layer results in the stagnation

region. The theory (Cebeci and Bradshaw 1984) is not intended to be valid for locations far from the stagnation point. It says

$$C_f = 3.486\theta$$

where θ is in radians.

Boundary-layer theory is not valid past the point of separation and, for skin friction, characteristically over-predicts the values past the actual maximum. Chen and Pletcher (1990) used a coupled strongly implicit procedure to compute the skin friction shown. The experimental results tend to be a bit sporadic in the first twenty degrees but overall compare well. It should be noted that these data by Acrivos et al. (1968) are for a variety of Reynolds numbers ranging between 61 and 150 inclusive (using a splitter plate to maintain steady flow). They scaled their results with Reynolds number as in Figure 5.5 and found them to be independent of the Reynolds number.

To validate the present scheme further, surface vorticities for flows of higher Reynolds numbers are shown in Figures 5.6 and 5.7. The vorticity is defined using dimensionless velocities and lengths

$$\omega = -\frac{\partial u}{\partial y} + \frac{\partial v}{\partial x}$$

The same grid as used for the $Re = 40$ calculation was used here also. For the Reynolds number of 100 case, 285 iterations were required; 520 were needed to converge the solution for the Reynolds number of 200 case. The data of Dimopoulos and Hanratty (1968) are the only experimental results shown. They used an electrochemical technique to measure the velocity gradients on the cylinder surface. Their results were for flow over a cylinder with a splitter plate at a Reynolds number of 210 (circles

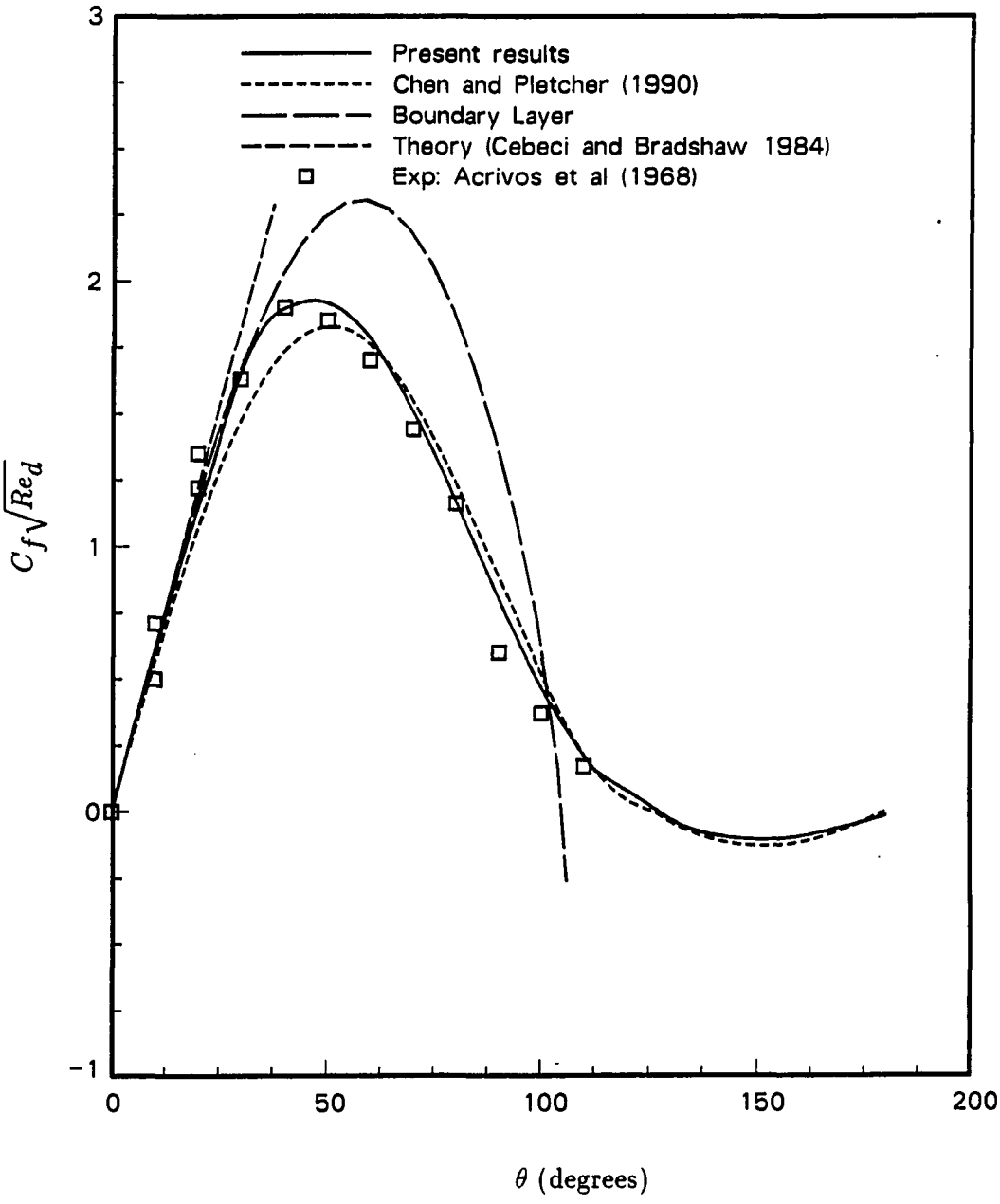

Figure 5.5: Skin friction on a right circular cylinder at $Re = 40$

in Figure 5.7) and over a cylinder with no splitter plate at a Reynolds number of 219 (triangles). The present results appear to agree better with the numerical results of Son and Haratty (1969). The results of Fornberg (1980) were computed numerically as well. All of the numerical results were calculated assuming symmetric flow.

Son and Hanratty (1969) explained the difference between their numerical results and the experimental results of Dimopoulos and Hanratty (1968) as being due to unsteadiness. They said that the splitter plate appeared not to have stabilized the wake completely. This appears to be a valid argument, considering that the trend of adding the splitter plate was to reduce the vorticity on the front half of the cylinder, while maintaining approximately the same values in the wake region. So it is expected that the trend would continue as the wake is further stabilized as it is in the numerical results.

From the results shown in Figure 5.7, it appears that vorticity in the separated region is well predicted using a symmetric flow field and a steady solver. The heat transfer results shown later do not exhibit this tolerance.

The pressure coefficient is shown in Figure 5.8. Some scatter of the data is seen here too. The present results tend to follow the same trends as the others.

A comparison of more flow results is shown in Figure 5.9. The abscissa is the distance (made dimensionless with the radius) from the cylinder center. The ordinate is the velocity on the line of symmetry. The results of Majumdar and Rodi (1985) and Nieuwstadt and Keller (1973) are calculated. Coutanceau and Bouard (1977) used a photographic technique in which they were able to measure the length of the traces made by particles during the time of exposure. In an attempt to improve this profile, a refined grid (100×64) with improved resolution in the wake was created.

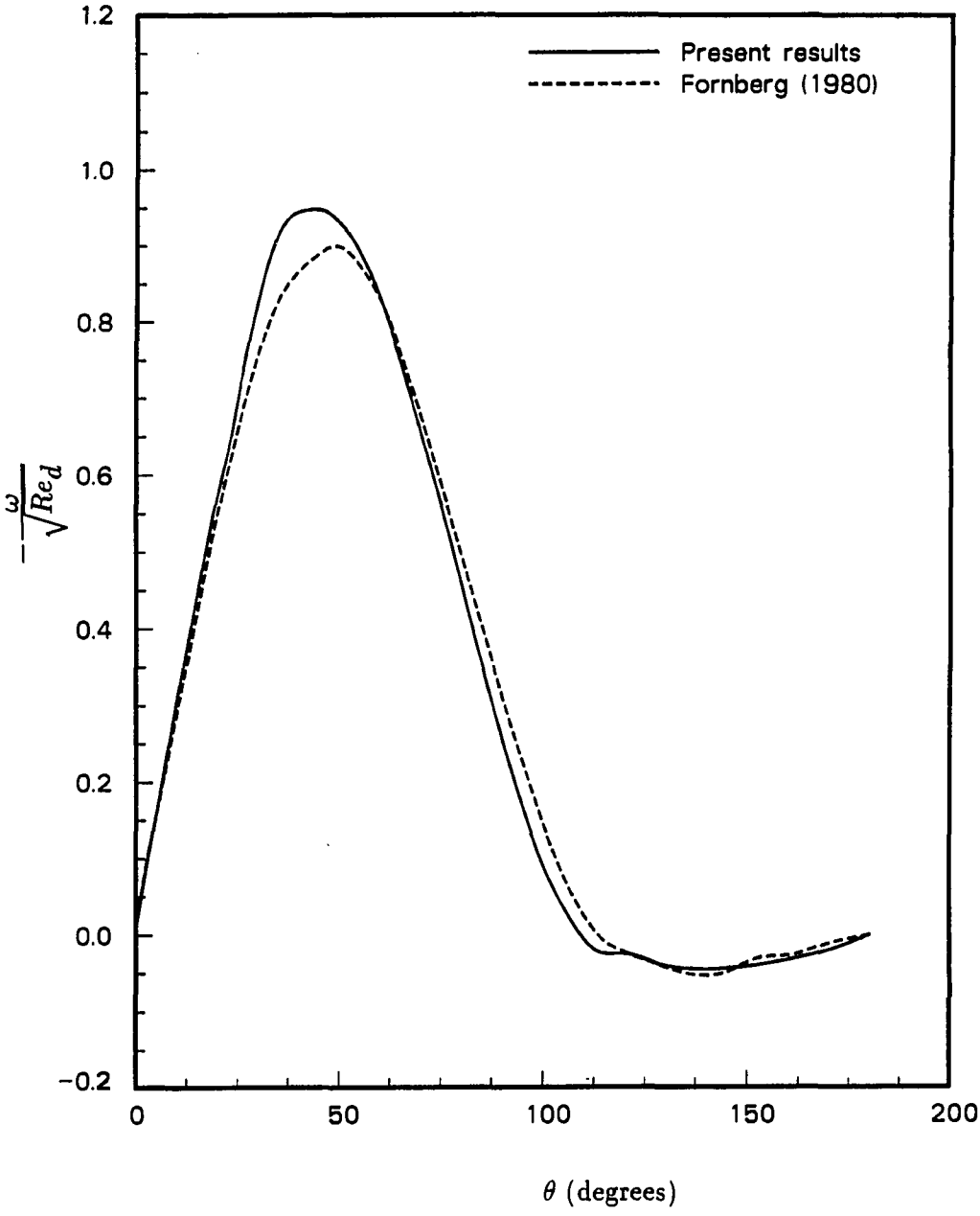

Figure 5.6: Vorticity on the surface of a cylinder at $Re = 100$

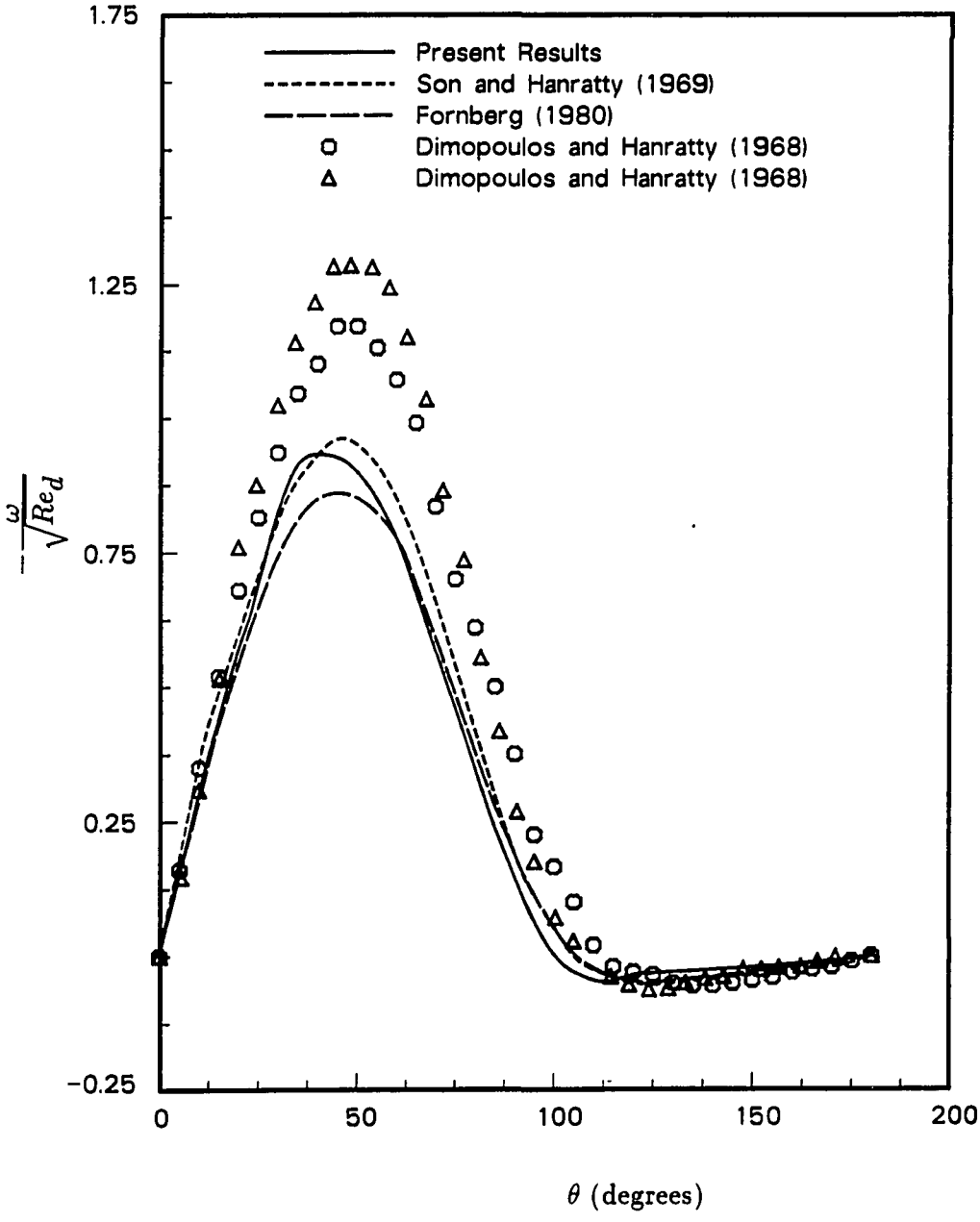

Figure 5.7: Vorticity on the surface of a cylinder at $Re = 200$

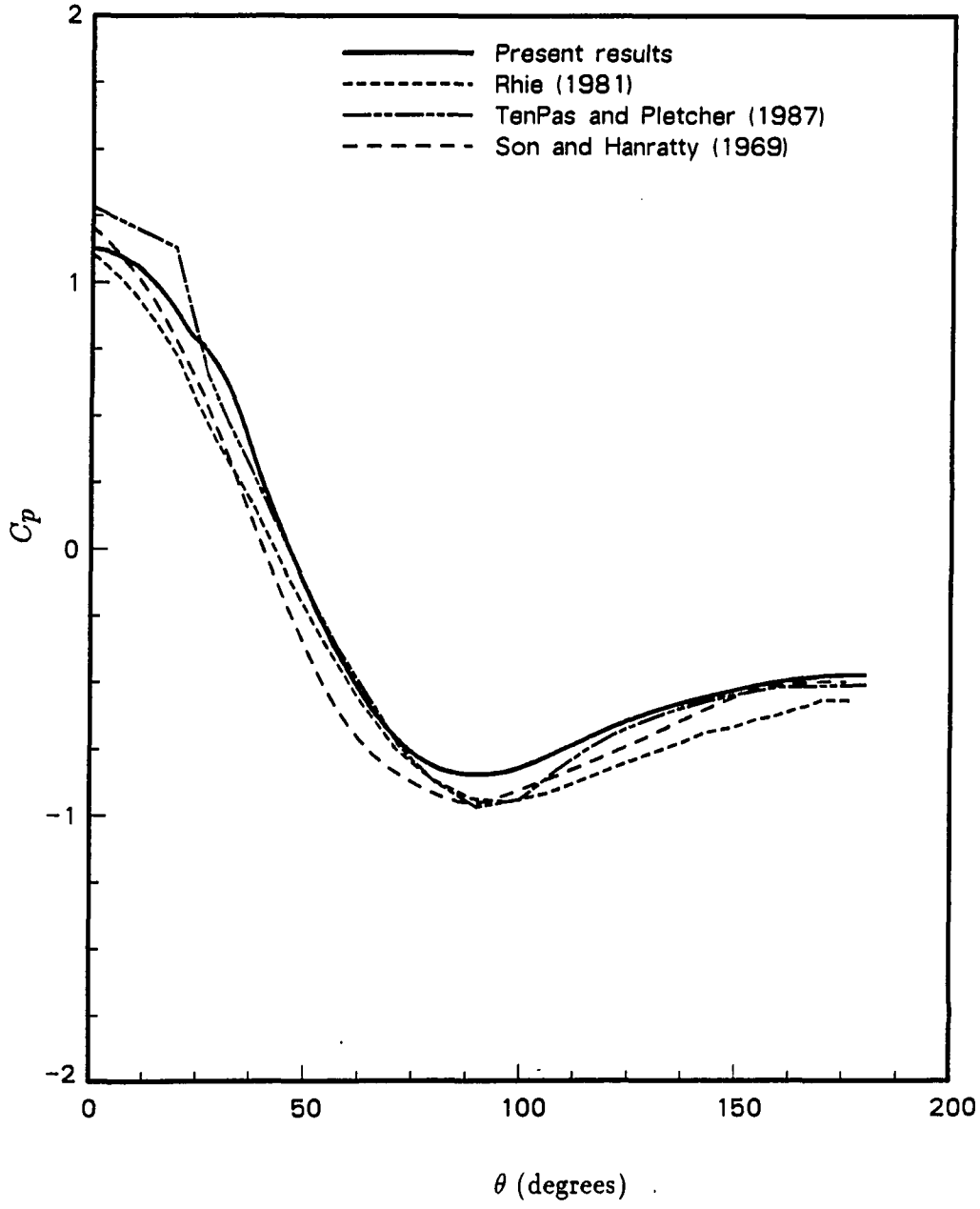

Figure 5.8: Pressure coefficient over a right circular cylinder at $Re = 40$

The results shown here exhibit some of the most obvious response to grid refinement (more on grid refinement is discussed below with regard to Table 5.1 and Figures 5.14 - 5.16).

Nusselt number results are compared with theory and experiment in Figure 5.10. The work of Eckert and Soehngen (1952) is for a Reynolds number of 23. Frössling's well-known theory is for the front portion of the cylinder only. The same should be said of the boundary-layer theory. The results from the present work lie in between. Although Chun and Boehm (1989) solved the full Navier-Stokes equations, their results tend to lie close to the boundary-layer solution. It should be noted that the plot for Chun and Boehm (1989) is for a Reynolds number of 50. The slight decrease in Nusselt number at the stagnation point shows up to some degree in many numerical and experimental plots. It is perhaps a bit more pronounced in the present work than in most.

The Nusselt number was averaged over the body surface for comparison of average Nu vs. Re correlations. The results can be seen in Figure 5.11. For very low Reynolds numbers the space-marching scheme tends to over predict, but not excessively. However, at more moderate Reynolds numbers the agreement is excellent.

Figures 5.12 and 5.13 are for higher Reynolds number flows. Both figures show a comparison between the numerical results of Karniadakis et al. (1986) and the present results. Figure 5.12 is for a Reynolds number of 100, while Figure 5.13 is for a Reynolds number of 200. The comparison is not particularly good, but is especially poor in the separated region. This is because Karniadakis et al. (1986) solved the entire flow domain and, therefore, vortices were shed. The present work had no provision for this type of unsteadiness.

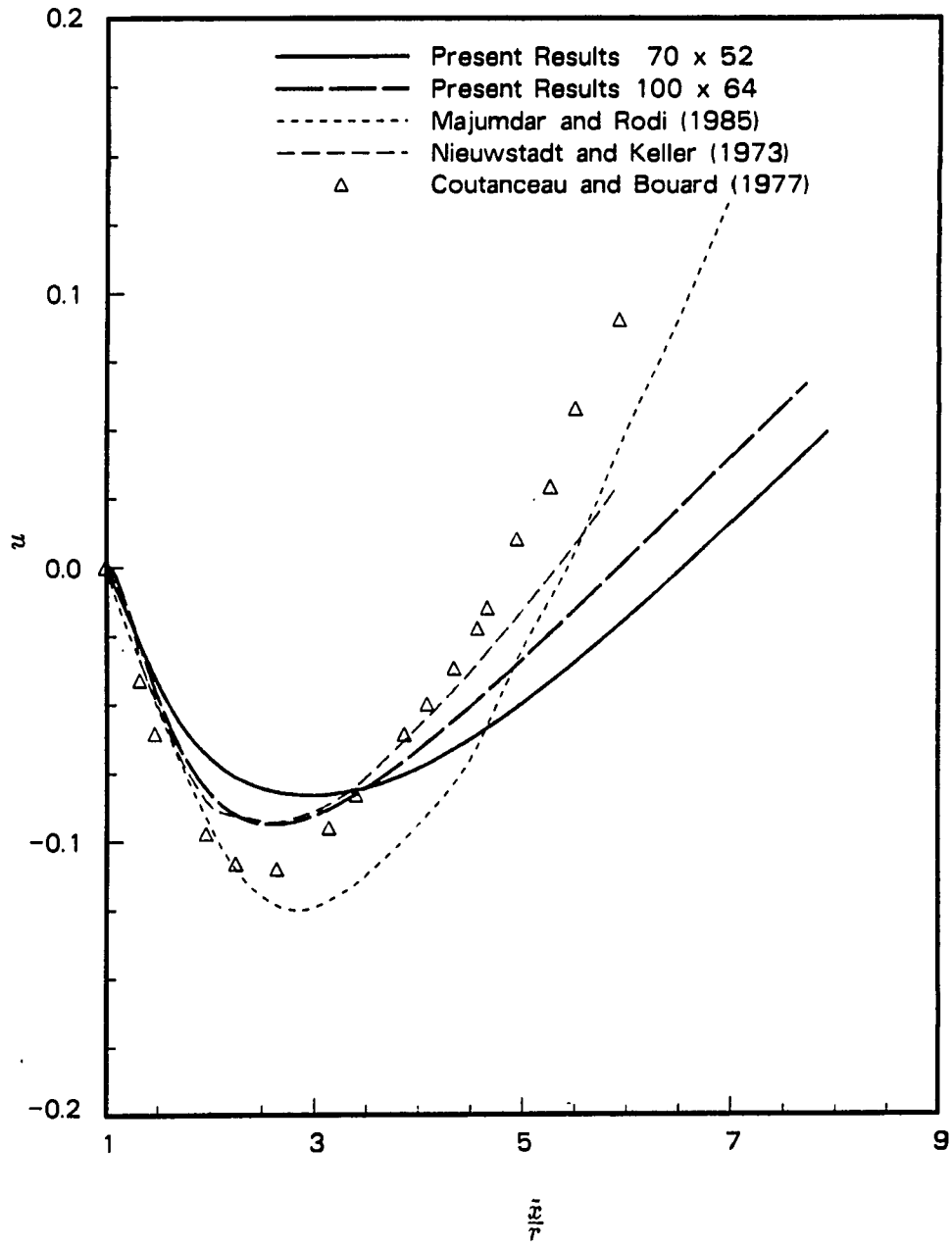

Figure 5.9: Centerline velocity downstream of the trailing edge of a cylinder at $Re = 40$

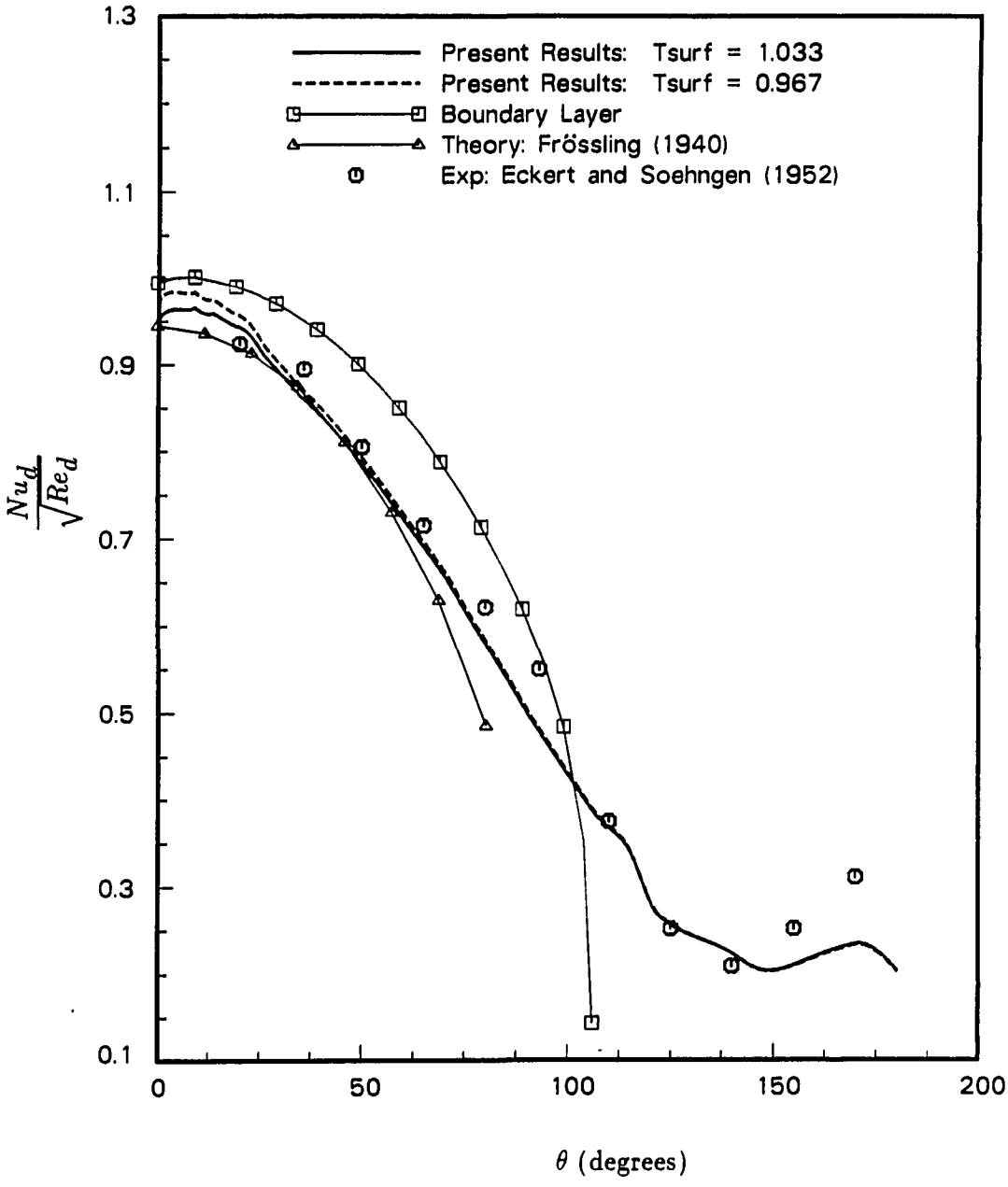

Figure 5.10: Local Nusselt number over a right circular cylinder at $Re = 40$

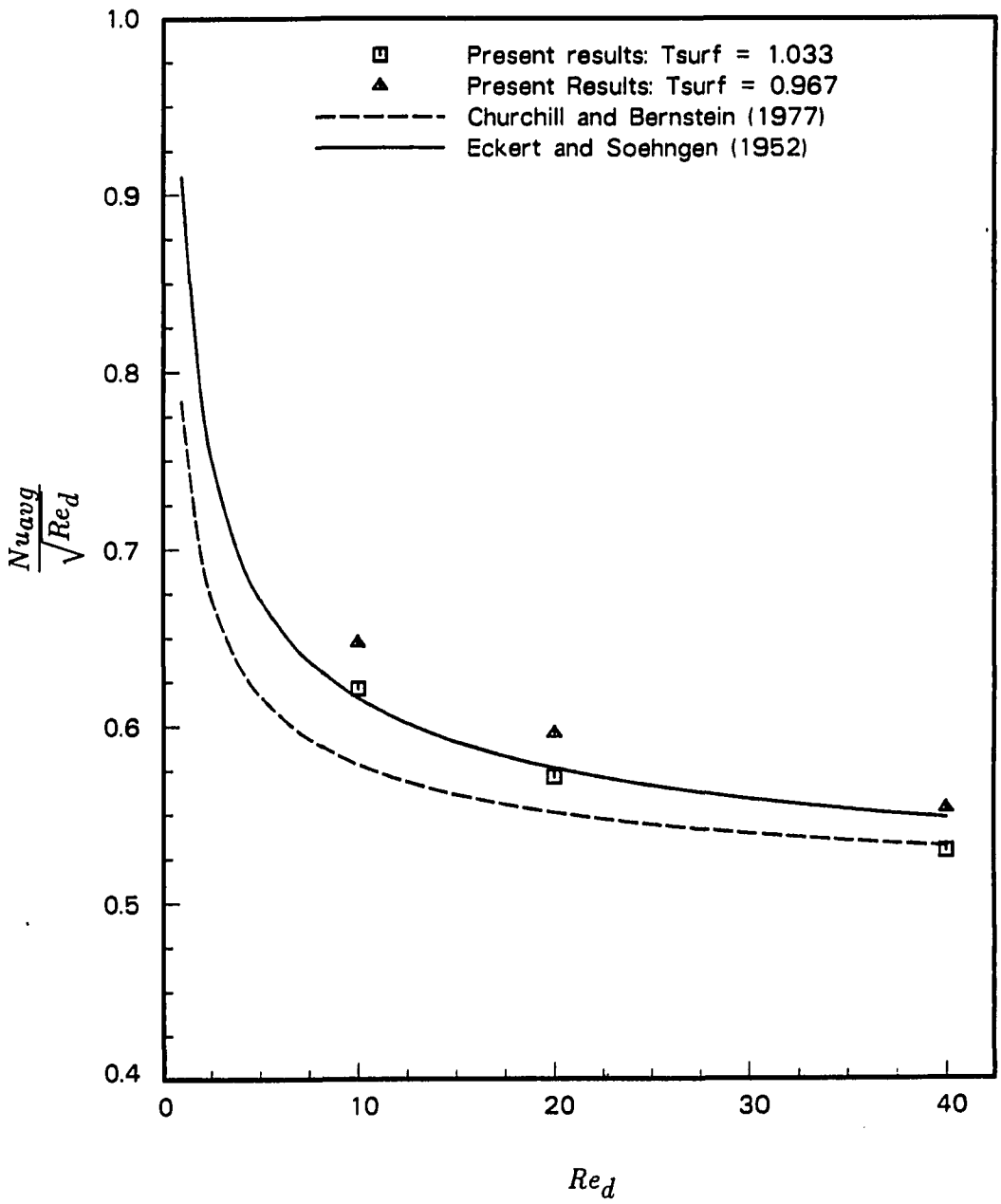

Figure 5.11: Average Nusselt number over a right circular cylinder for various Reynolds numbers

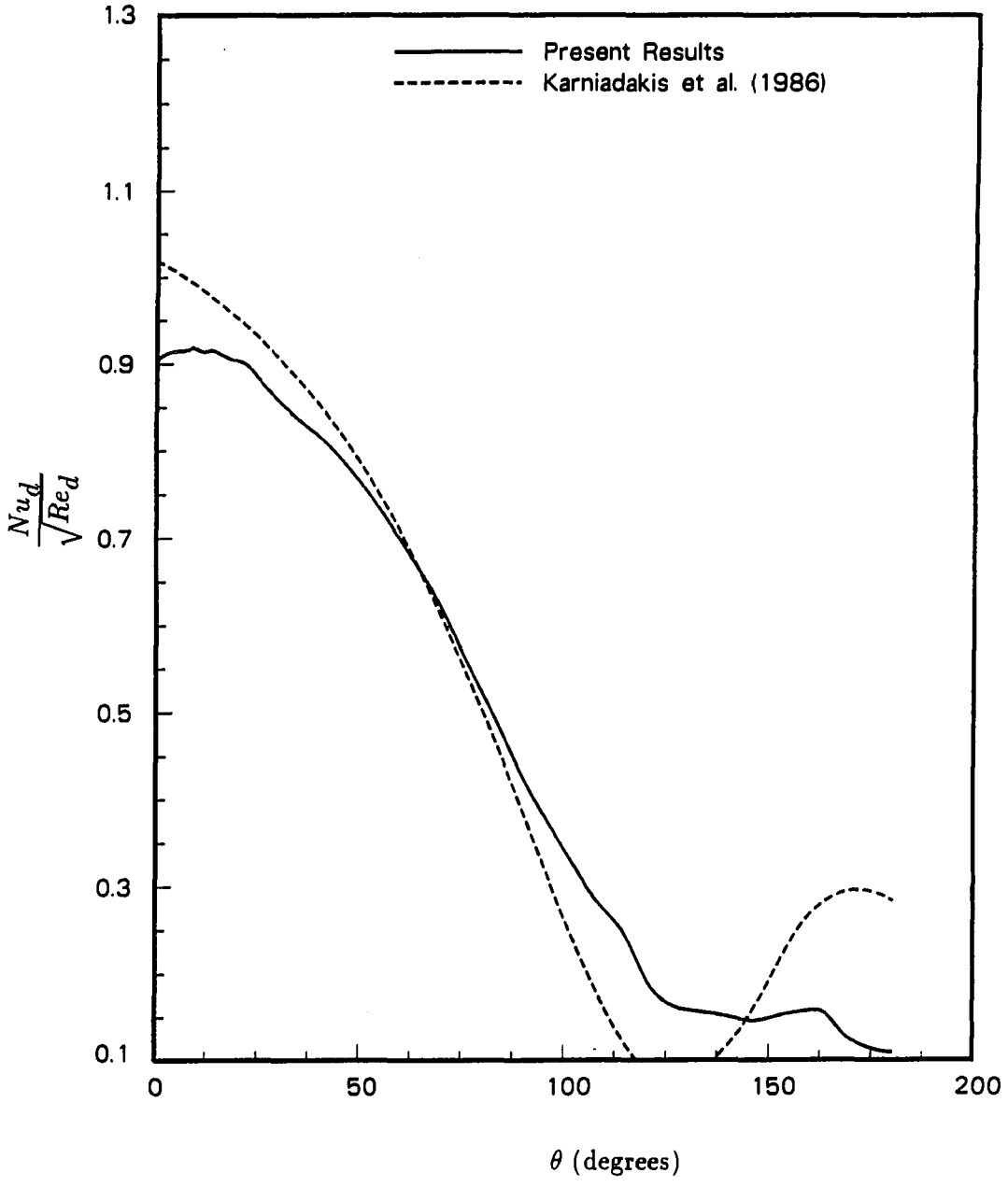

Figure 5.12: Local Nusselt number over a right circular cylinder at $Re = 100$

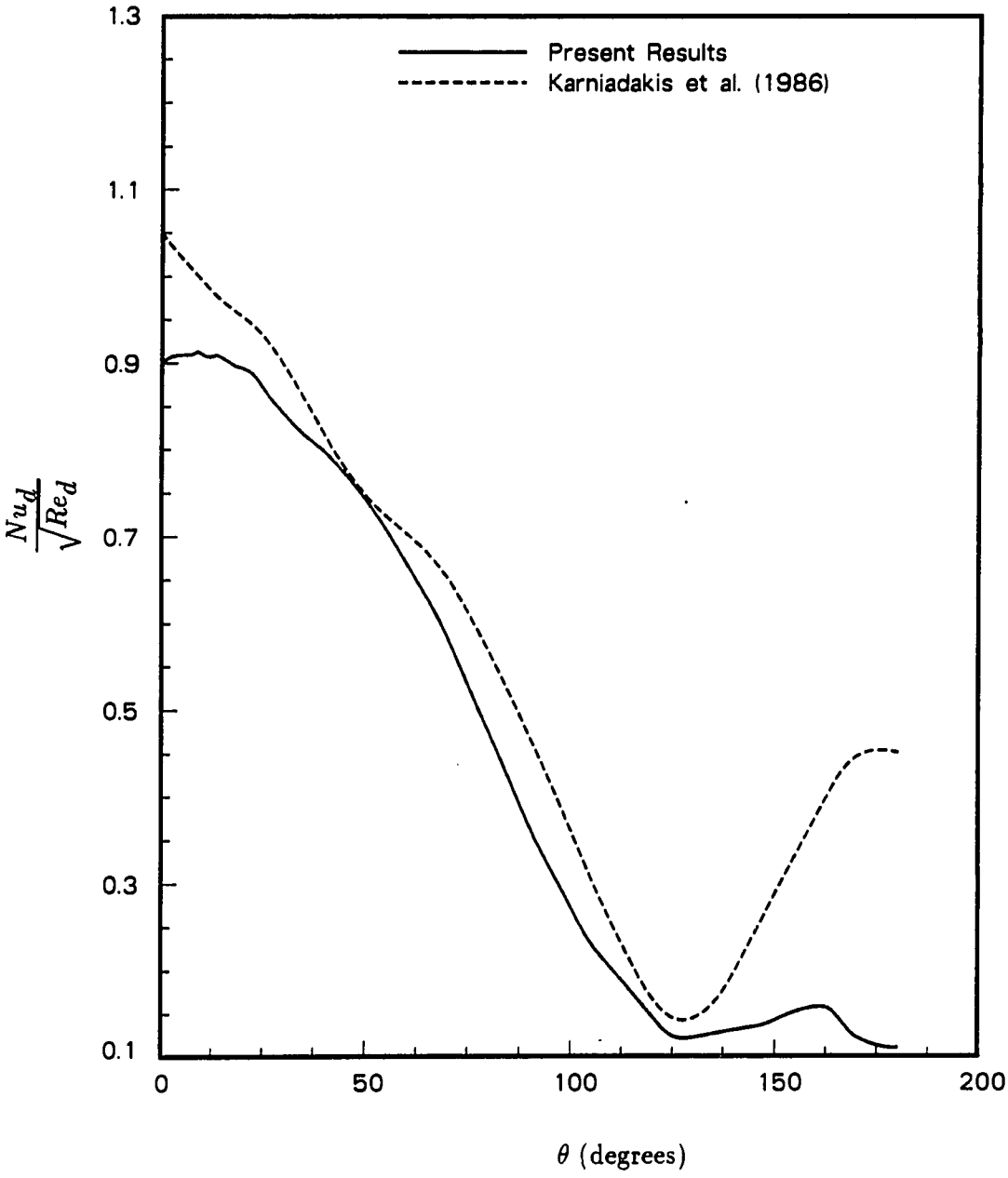

Figure 5.13: Local Nusselt number over a right circular cylinder at $Re = 200$

A summary of some interesting aspects of the solution are tabulated in Table 5.1. Comparisons are made with the results of Fornberg (1980). Results from two grids for the present work are shown for the Reynolds number of 40 case. The column headed '40c' is for a 70 × 52 grid with 41 nodal points on the cylinder surface. The '40f' column contains results for a 100 × 64 grid with 58 points located on the body surface. The separation angles compare quite favorably, as do the stagnation point pressure coefficients. Since the purpose of this run was to test the resolution of the heat transfer near the leading edge, the grid tended to be course downstream of the cylinder. The grid refinement for the Reynolds number of 40 case shows that better resolution was possible with more favorable nodal-point clustering.

Table 5.1: Summary of results for steady flow over a cylinder at various Reynolds numbers

	Present Results				Fornberg (1980)		
Reynolds number	40c	40f	100	200	40	100	200
Separation angle (degrees)	127	125	110	101	124	111	94.3
Reattachment point (radii)	6.48	5.93	16.2	23.6	5.48	13.7	28.0
Front stag. pt. pressure coeff.	1.12	1.12	1.04	1.03	1.14	1.06	1.02
Rear stag. pt. pressure coeff.	-.49	-0.49	-.38	-.28	-.46	-.34	-.24

A rigorous comparison of CPU times used by various researchers is a near-impossibility since the times from different computers cannot be compared easily. To give some idea of the times used in this study, as well as those of Son and Hanratty (1969), CPU times for two Reynolds numbers are shown in Table 5.2. Note that the calculation in the present study included the energy equation, whereas Son and Hanratty (1969) resolved the flow only.

Some indication of the effects of grid refinement are seen in Figure 5.9 and

Table 5.2: CPU times, in minutes, required to converge the steady solution of flow over a cylinder

		Re	
Researchers	Computer	40	200
Present Results	Cray X-MP	8.2	25
Son and Hanratty (1969)	IBM Model 75	40	420

Table 5.1. This is carried further in Figures 5.14 – 5.16. The Reynolds number of 40 case was run with two different grids. The fine grid was 107×64 with 63 points defining the cylinder. The course grid was 62×52 and had 29 points on the cylinder surface. The skin friction and pressure coefficient results (Figures 5.14 and 5.15) show virtually no change with grid refinement.

The heat transfer results show more of a change than the flow with grid refinement. The Nusselt number, as shown in Figure 5.16 varies most in the region of the stagnation points. The fine grid was four times finer near the front stagnation point than the course grid (points every $\frac{1}{2}$ degree, compared to every 2 degrees). More points were clustered in the wake region for the fine grid as well. This helps explain the changes observed near these stagnation points.

In general, very good results were obtainable with moderately course grids for this case. The extra computer effort required to compute the solution on a fine grid may not be justified in many instances.

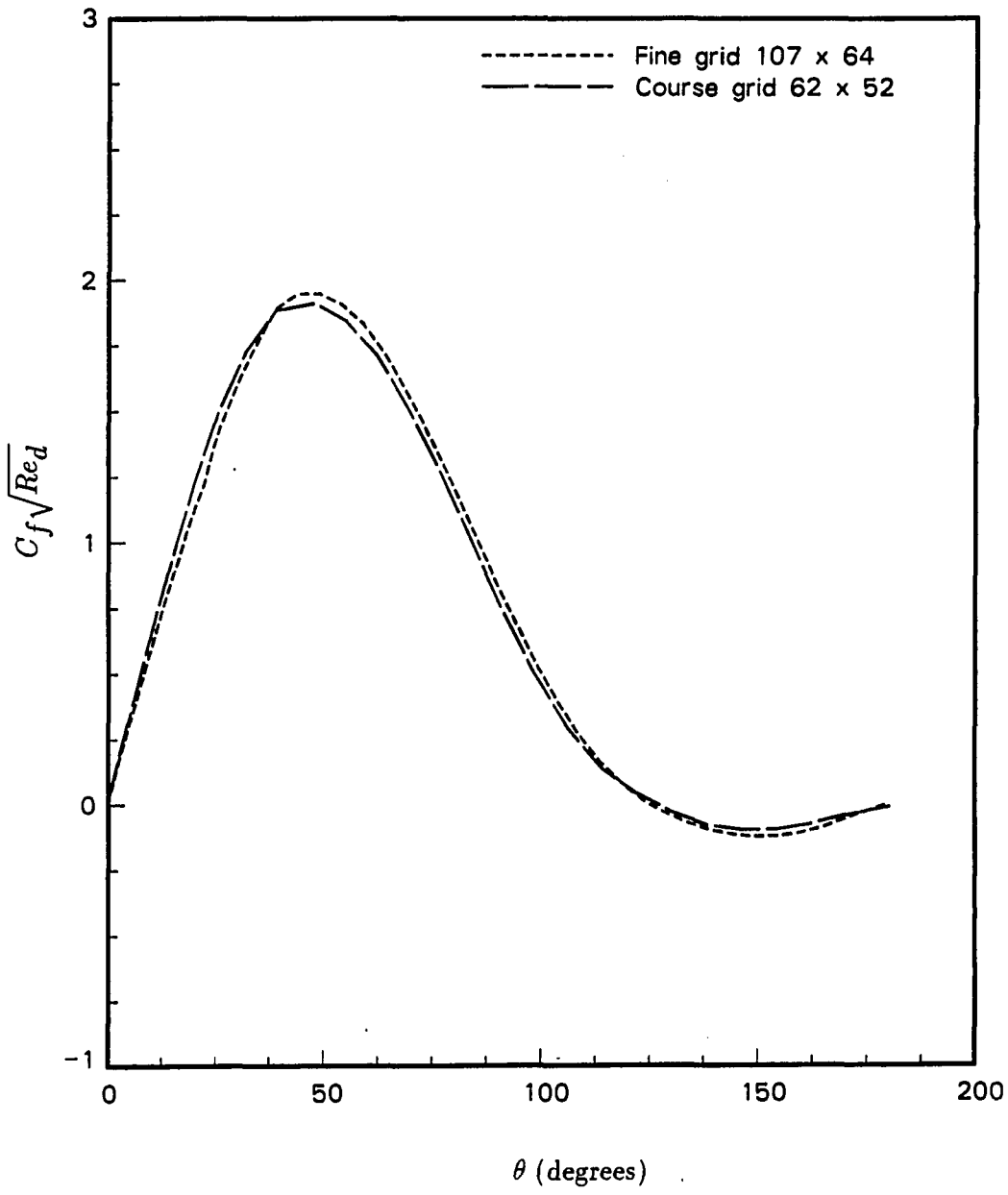

Figure 5.14: Effect of grid refinement on skin friction for a Reynolds number of 40

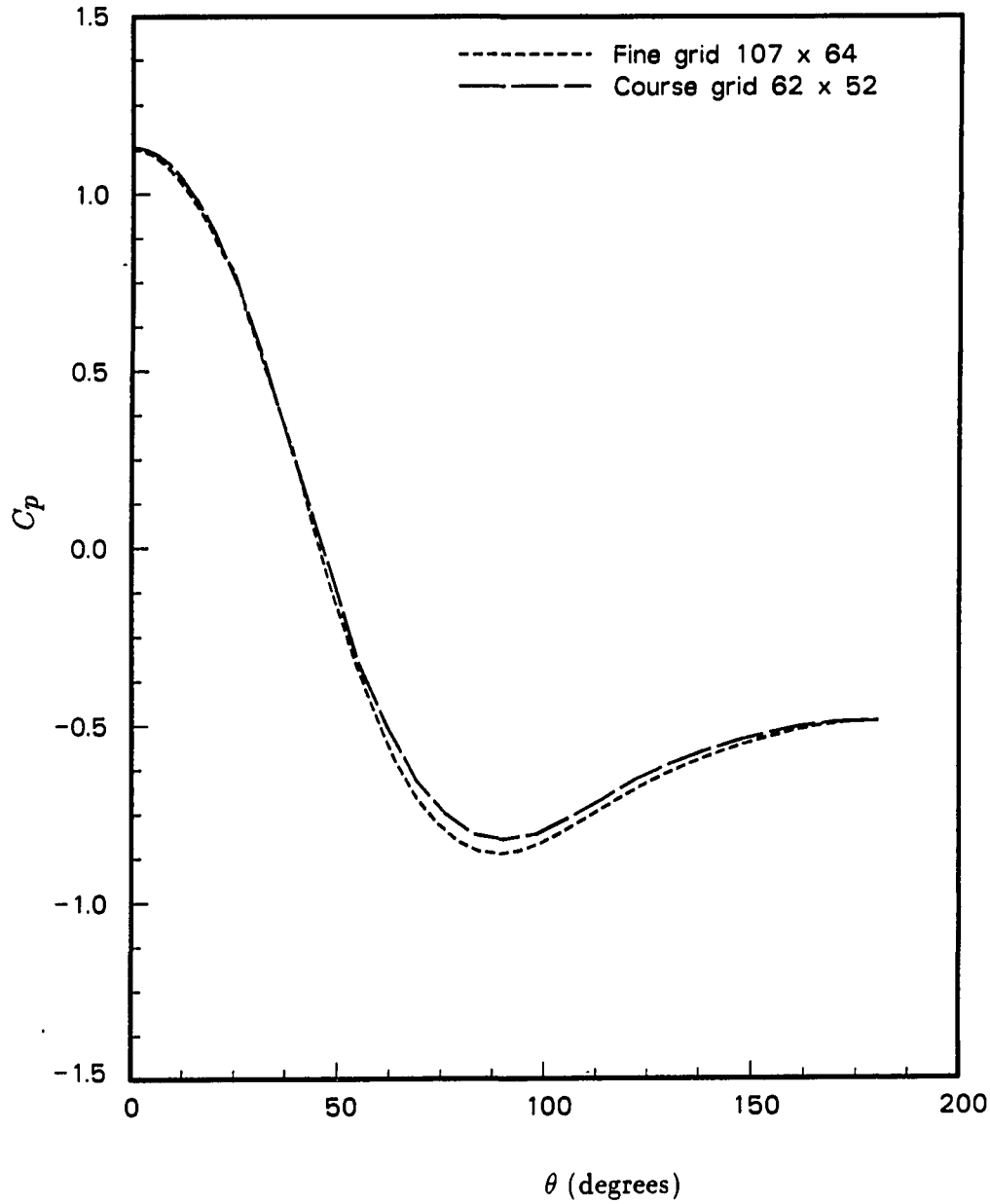

Figure 5.15: Effect of grid refinement on pressure coefficient for a Reynolds number of 40

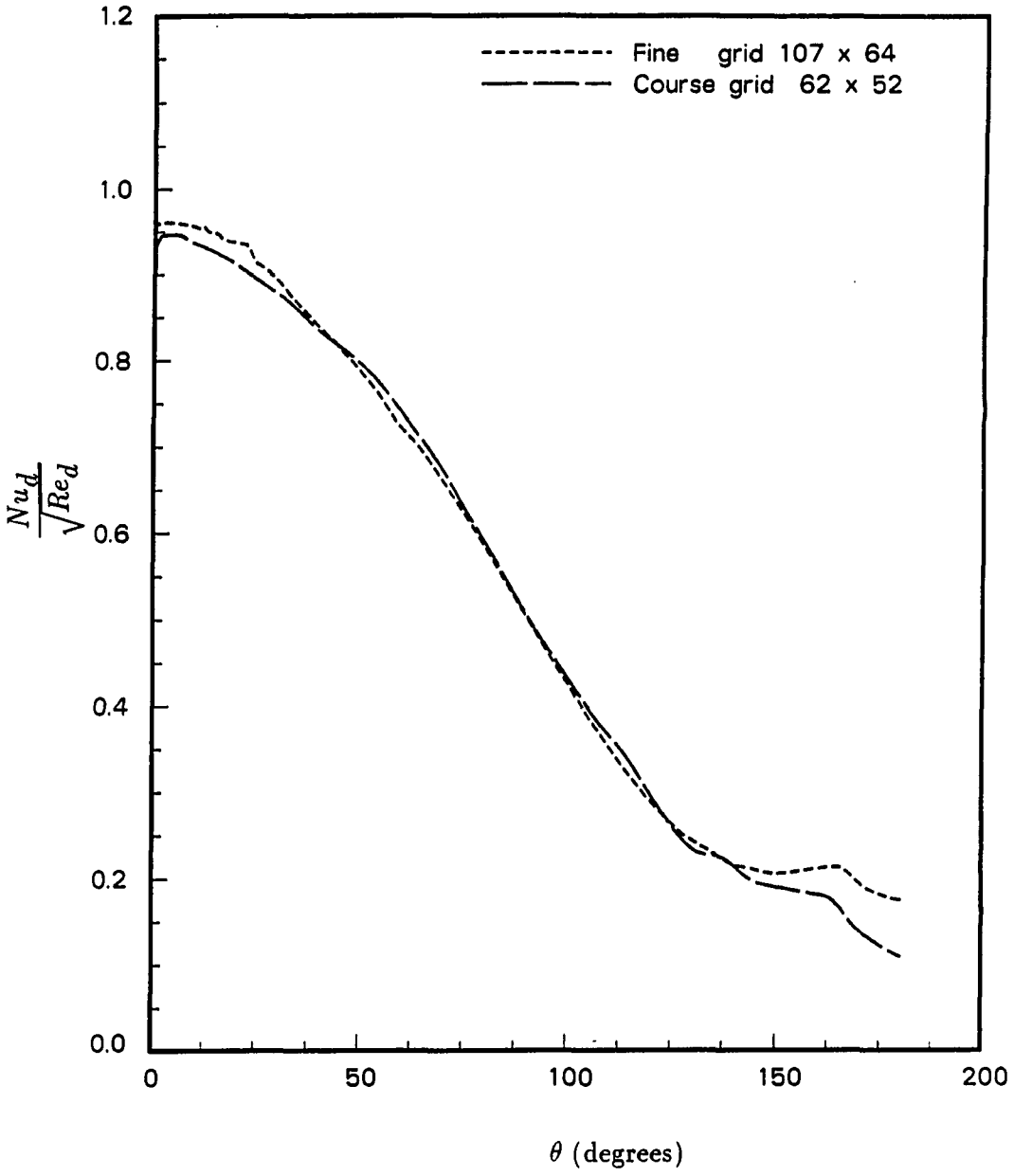

Figure 5.16: Effect of grid refinement on Nusselt number for a Reynolds number of 40

Unsteady flow

Unsteady cases are of two sorts for flows over a blunt body. In one type, the changes in time are due to changes in time of the boundary conditions. These changes may appear as a step-change, as in flows which evolve from a stagnation condition, or the boundary conditions may change continuously throughout time.

In the second case, the boundary conditions are steady. Portions of the flow are inherently unsteady. An example of this case is the vortex-shedding behind a cylinder.

Impulsively started cylinder To further validate the temporal terms, the case of a right-circular cylinder, started from potential-flow conditions was attempted. A symmetric C-grid with 109×64 node points was used. There were 41 points placed on the body surface. The grid extended 15 diameters upstream, downstream and in the transverse direction. A dimensionless time step of 0.025 was used. To compare with other numerical data, as well as experimental results, the Reynolds number based on diameter was set to 550 and the Mach number to 0.1. As above, the Prandtl number was fixed at 0.7.

The results of this case are shown in Figures 5.17 – 5.24. Figures 5.17 – 5.21 are shown for comparison with the work of other researchers. The remainder however, are believed to be new contributions for this type of flow.

In Figure 5.17, the maximum *negative* velocity on the line of symmetry, and its location are plotted. Both are dimensionless. A second-order polynomial was used to interpolate between nodal points for both values. The abscissa was nondimensionalized using the radius, r, of the cylinder, $\frac{\tilde{t}}{r/u_r}$. The experimental results of

Coutanceau and Bouard (1980) and the numerical results of Chamberlain (1987) are shown in this figure for comparison.

The upper two curves represent the dimensionless length, and are labeled in the legend as 'x'. The lower curves are the dimensionless velocities, labeled 'u' in the legend.

At large times, the quality of the results falls off. This is believed to be due to an overly course grid.

The local vorticity, ω, for integer values of the dimensionless time, $\frac{\tilde{t}}{r/u_r}$, is shown in Figure 5.18. Some comparisons to Loc's (1980) numerical data are found in Figures 5.19 - 5.21. In Figure 5.21, at a time of 5, Chamberlain's (1987) numerical data are also shown. The agreement is, in general, only fair. Loc (1980) and Chamberlain (1987) used O-grids of dimensions 61×61 and 61×65, respectively. They both found that a secondary vortex was formed at approximately 140 degrees. It was most noticeable at the later times. As seen in Figure 5.22, this structure was not resolved in the present study even at a dimensionless time of 5. Therefore, the vorticity falls short of the other researcher's values at this point.

New results for this case are found in Figures 5.23 and 5.24. The spatially averaged Nusselt number is plotted as a function of dimensionless time in Figure 5.23. The correlation of Churchill and Bernstein (1977) is also plotted for comparison. This correlation is for steady (time averaged) flow at steady state.

To illustrate the development of the temperature solution, the local Nusselt number is plotted against the angle measured from the front stagnation point in Figure 5.24. Comparison to Figure 5.18 points out the fact that the temperature field seems to develop more quickly than the flow solution. Although both quantities

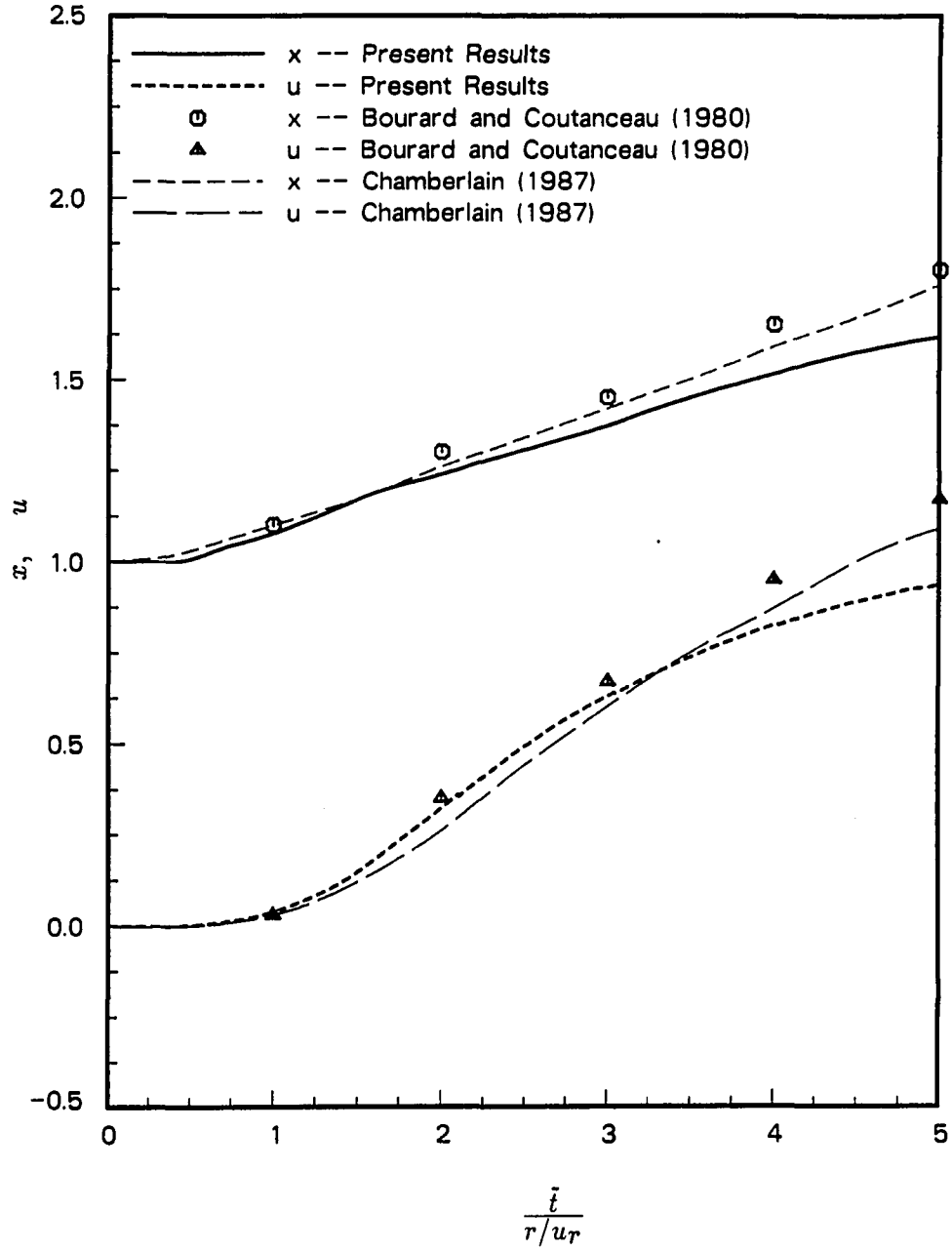

Figure 5.17: Maximum negative velocity on line of symmetry downstream of a right circular cylinder and its location

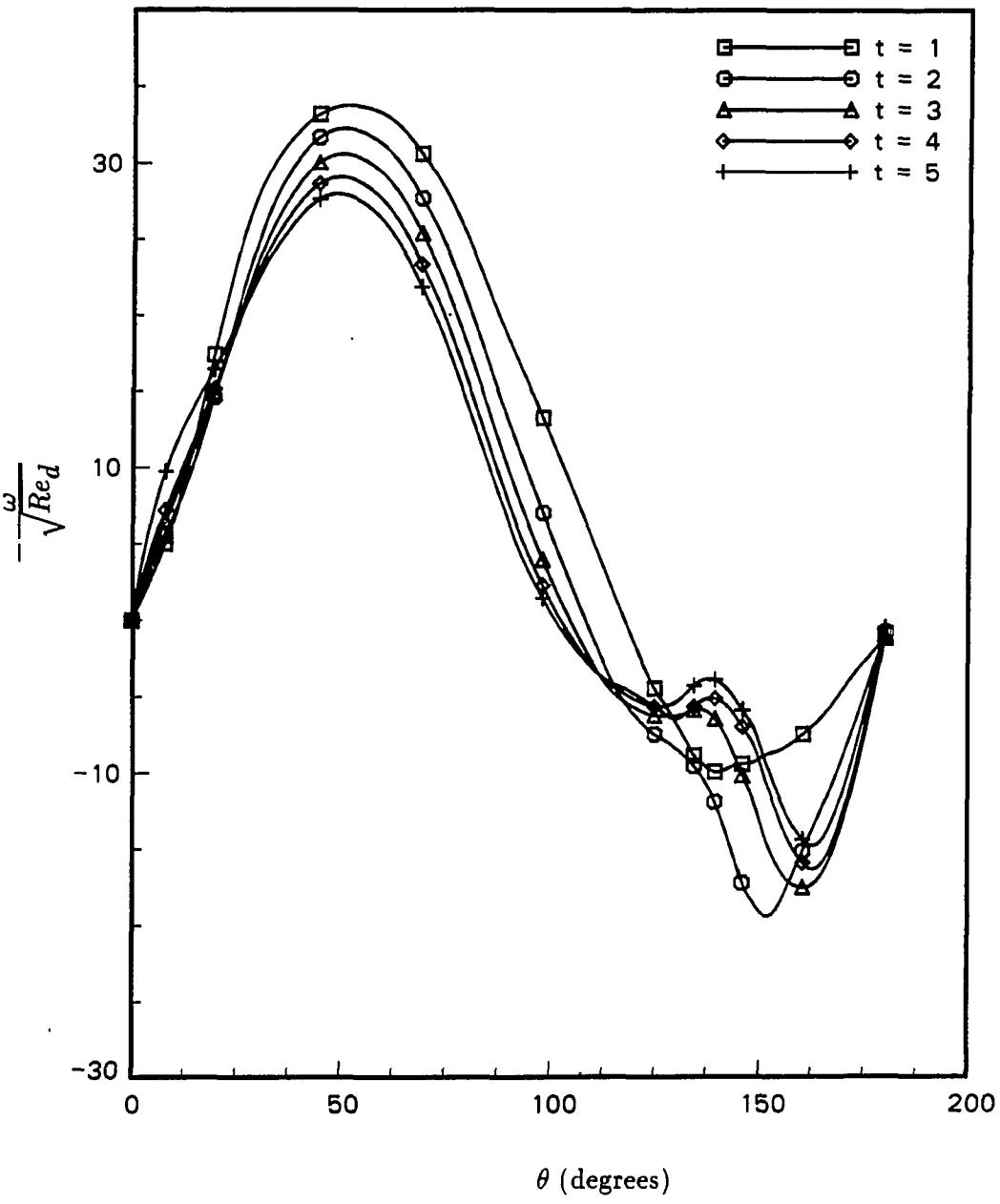

Figure 5.18: The evolution of the vorticity on an impulsively started right circular cylinder in crossflow

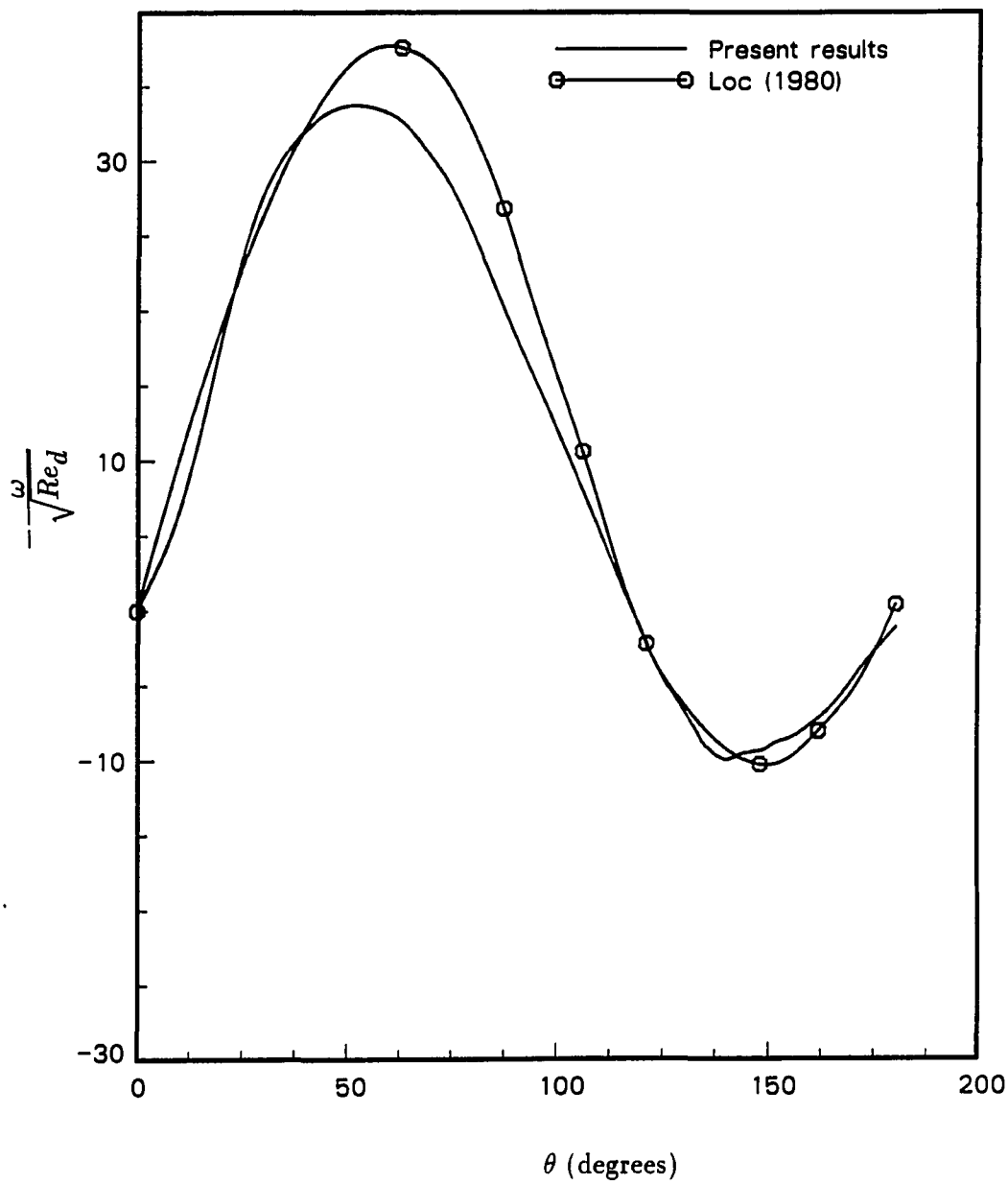

Figure 5.19: Vorticity on an impulsively started right circular cylinder in crossflow at a dimensionless time of 1

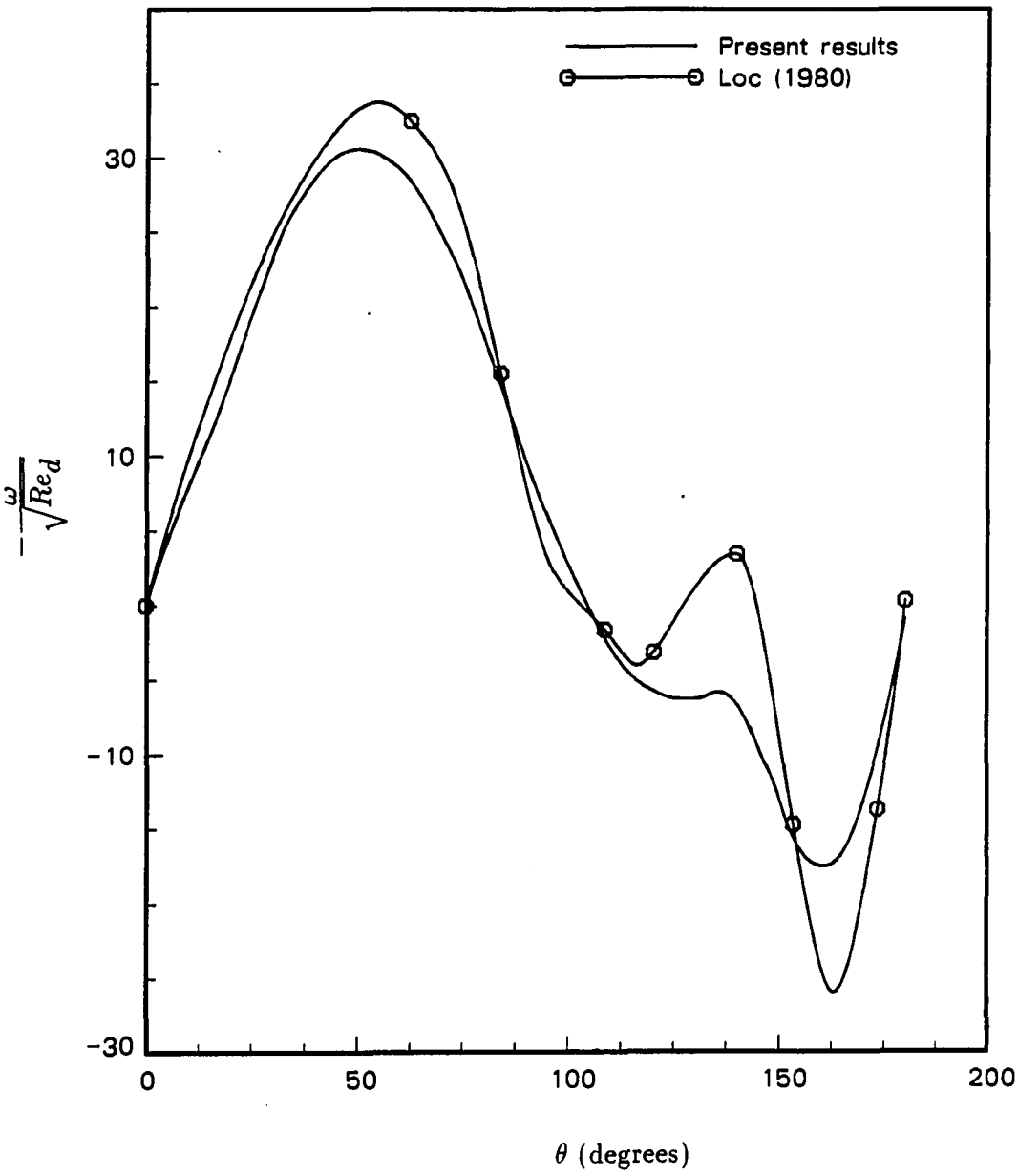

Figure 5.20: Vorticity on an impulsively started right circular cylinder in crossflow at a dimensionless time of 3

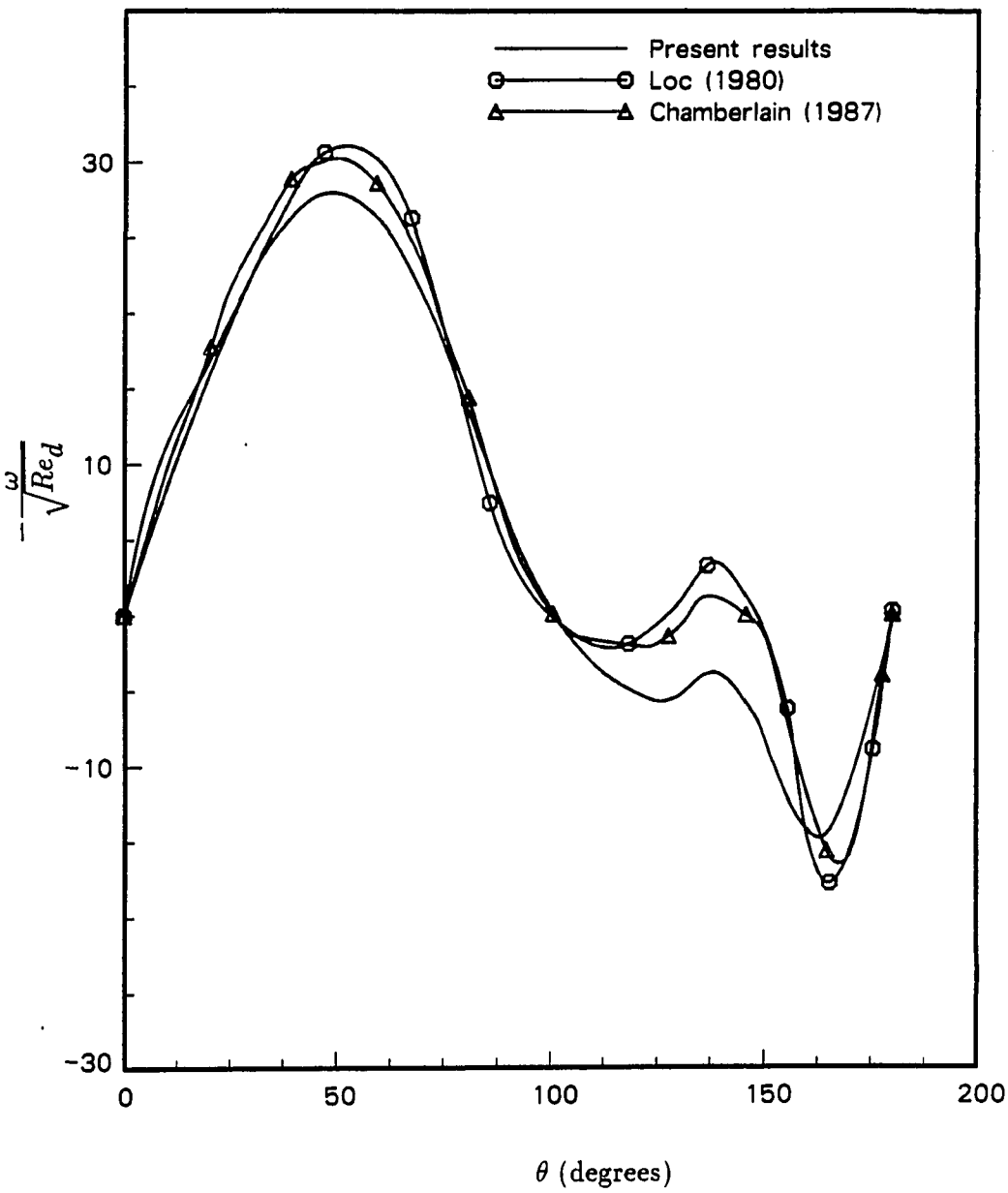

Figure 5.21: Vorticity on an impulsively started right circular cylinder in crossflow at a dimensionless time of 5

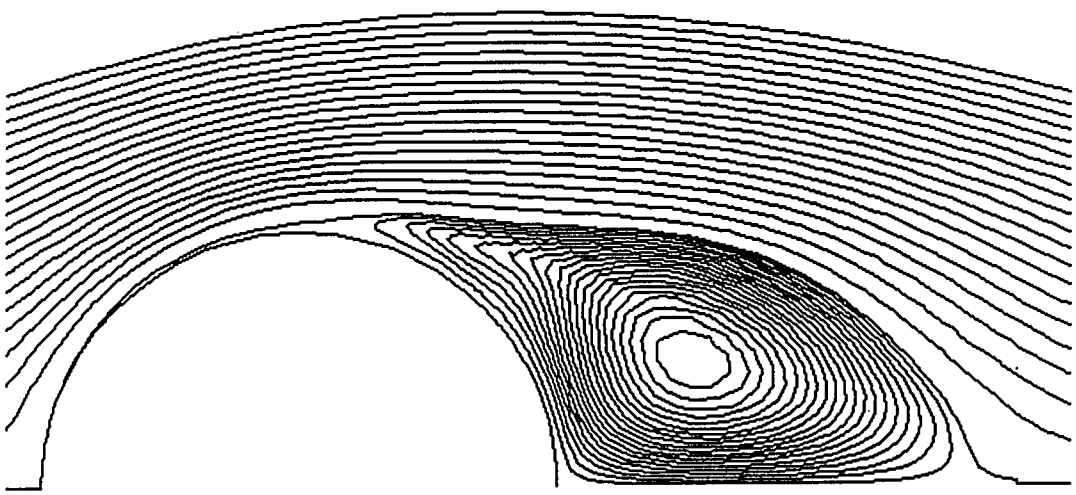

Figure 5.22: Streamlines over an impulsively started right circular cylinder in cross-flow at a dimensionless time of 5

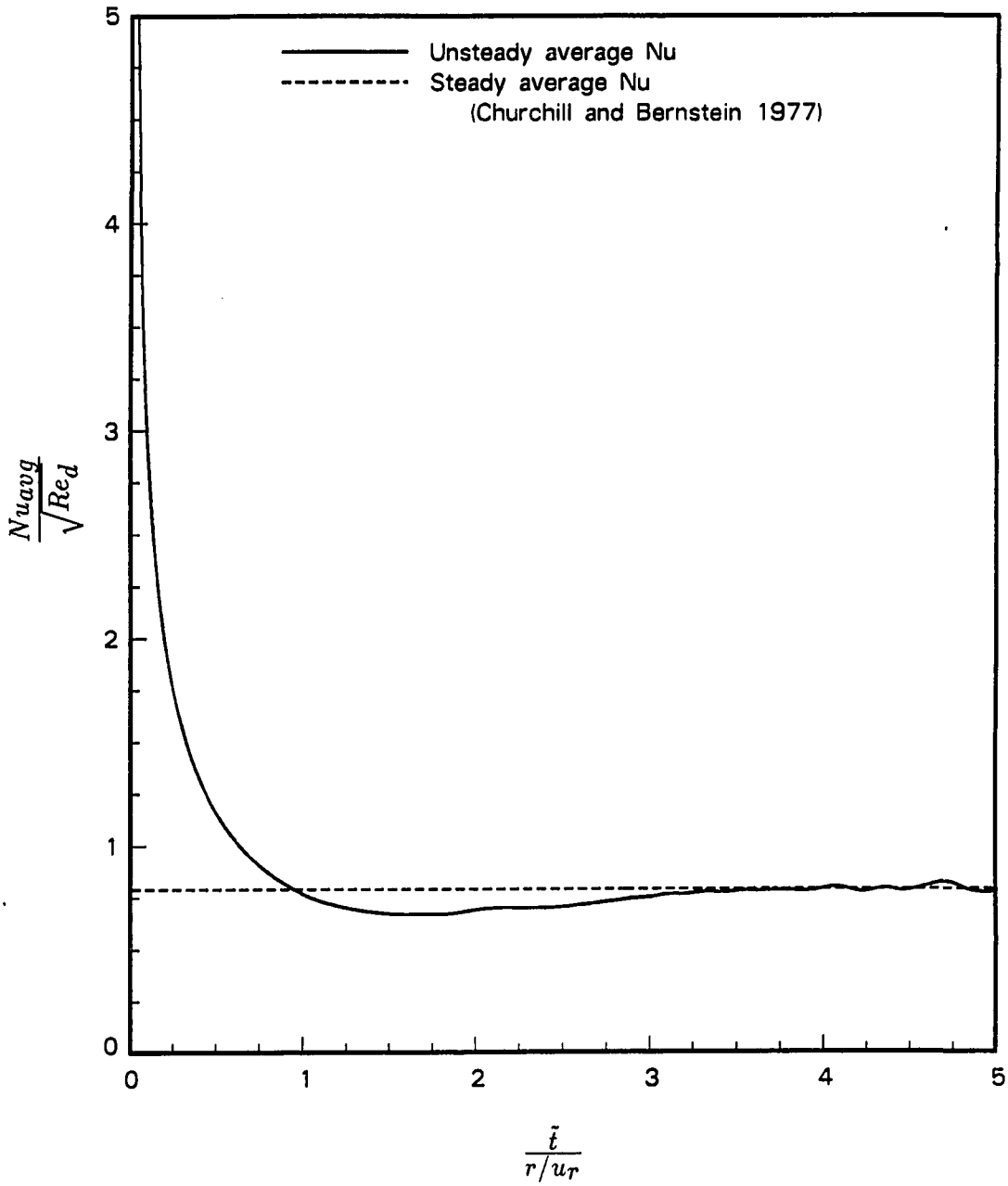

Figure 5.23: The evolution of the average Nusselt number on an impulsively started right circular cylinder in crossflow

are still evolving, even for time $t = 5$, the vorticity appears to be changing more drastically at the later times than the Nusselt number.

In order to converge the solution to $|\epsilon| \leq 5 \times 10^{-5}$ at a given time, approximately 20 iterations were needed.

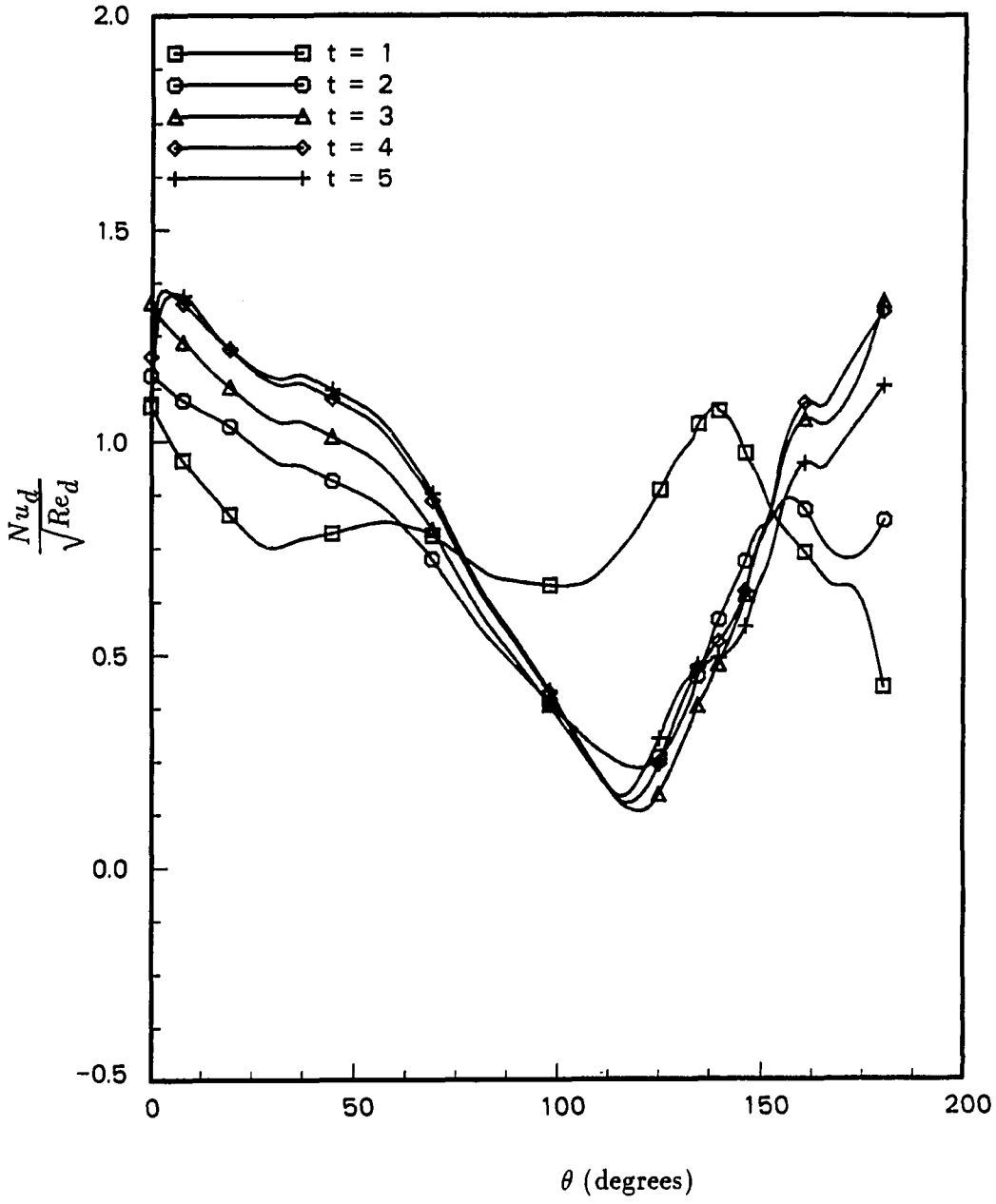

Figure 5.24: The evolution of the local Nusselt number on an impulsively started right circular cylinder in crossflow

CHAPTER 6. CONCLUSIONS AND OBSERVATIONS

The steady space-marching scheme of TenPas (1990) was extended for use on a C-grid and for unsteady flows. It was used to calculate flow and heat transfer over a flat plate and right circular cylinder in both steady and unsteady modes. New results were presented in the form of heat transfer for an impulsively started cylinder.

In terms of computational efficiency and numerical accuracy, the space-marching scheme used in this study was found to perform well for steady flows. Judging from previous work (TenPas 1990), it is best suited to flows which have a relatively small amount of downstream influence. These would include flows with little streamwise pressure gradient, and only small recirculation regions.

A measure of the efficiency of a solution procedure is the number of subiterations required to gain convergence at a given time step. Although more direct comparisons to other schemes should be made, on this basis, it is the opinion of the author that the present scheme does not handle unsteady flows efficiently. Large numbers of sub-iterations (20 to 50) were often required at each time step to resolve the flow at that instant. This compares to Chen and Pletcher (1990) who solved the flow over a full cylinder using a coupled modified strongly implicit procedure (CMSIP). They report needing only 2 sub-iterations at each time step for this complex flow. The same vortex shedding case was computed by Rogers and Kwak (1988) using a

pseudocompressibility method. They report needing 5 sub-iterations up until the flow became asymmetric and 12 - 15 following. Attempts to decrease the number of subiterations in the present work were largely unsuccessful.

Another unsatisfactory characteristic of the present scheme deals with the discretization of the physical space. In the work detailed here, and in that of TenPas (1990), the scheme was found to be sensitive to grid spacing. At times a solution on a fine grid was difficult to obtain unless severe relaxation of the pressures, or, in the present work, a false time step was employed.

The future of space-marching schemes is uncertain. For steady, internal flows, this method would be a viable option — and almost certainly superior to many others. For steady, external flows, this solution procedure should be given consideration — to what extent the flow is influenced by downstream conditions would be of primary concern. For unsteady cases, it is believed that other options should be seriously considered.

Vortex Shedding

A serious drawback of the present method was the inability to resolve the von Kármán vortex street. The reasons for this remain under investigation. Much time and effort was put into this attempt and no tangible results can be shown. The following are a few observations dealing with this flow and the solution procedure used.

As detailed before, the wake behind a right circular cylinder will become periodic in time (von Kármán vortex street) for Reynolds numbers greater than about 40. Many researchers have successfully resolved this flow (Patel 1978, Rosenfeld, Kwak,

and Vinokur 1988, Visbal 1986, Karniadakis, Mikic, and Patera 1986).

Calculation of this flow tends to be rather CPU time intensive. The solution usually evolves into a flow which resembles steady flow for that Reynolds number, then into the time periodic flow produced by the von Kármán vortex street.

Present work

An attempt was made to advance to flows with vortex shedding. A symmetric boundary condition will not allow the resolution of this phenomenon. Although the reasons why are not clear, it has not been possible to calculate this flow with the present method.

The procedure followed to solve this problem was to set up a full grid about the cylinder. The upstream, downstream and freestream boundaries were set the same as with the symmetric grid (see Figure 6.1). However, a discontinuity in the j indices occurred on the cut line. Moreover, two lines of constant η coexisted on that line. Because of this, special consideration was required for the differencing and solution of the resulting linear algebra.

Since it was desirable to march in the direction of the flow, the solution proceeded from upstream of the cylinder, beginning on the line of geometric symmetry, to the downstream boundary. It was deemed impractical to solve the regions directly above and below the body simultaneously. Therefore, each of these regions was always solved alone.

The region behind the cylinder (downstream of the trailing edge), was handled in one of two ways (refer to Figure 6.2):

1. This region was cut into upper and lower halves (regions 3a and 3b in the figure).

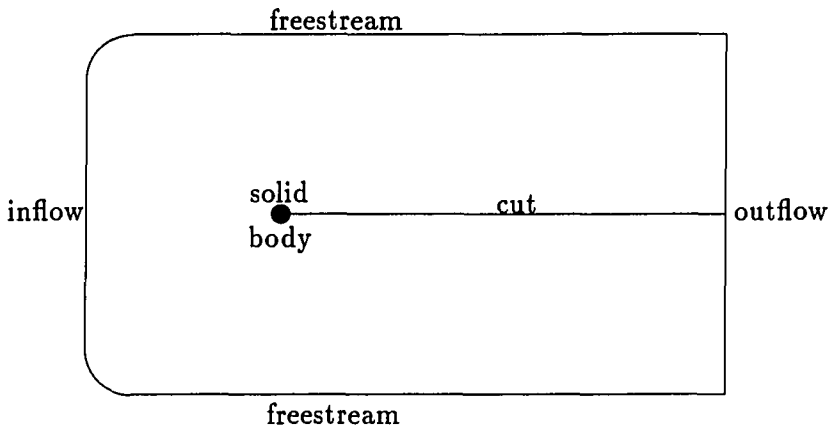

Figure 6.1: Full C-grid topology

Each half was treated as a continuation of the region directly upstream of it (regions 1 and 2). This is identical to the method outlined previously for the symmetric case, except that the grid is now like two geometrically symmetric grids.

2. This region was marched as a whole following the completion of the regions directly above and below the cylinder (regions 1 and 2). At each of these downstream stations (regions 3a and 3b), the resulting matrix was almost twice the size of the matrices solved in the other two regions.

In both of these methods, the momentum and energy equations were solved as usual. The half-continuity control volumes located directly above and below the cut were added to the adjacent full-control volumes. The pressure on the cut was taken

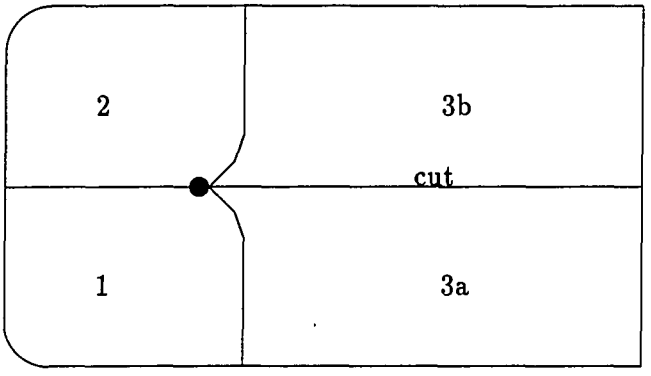

Figure 6.2: Breakdown of regions in the flow

as an average of the pressures immediately above and below.

$$p_{i+1,jcut} = \frac{p_{i+1,jcut+1} + p_{i+1,jcut-1}}{2}$$

In the first of the methods above, information required from across the cut was lagged. In the second, it was implicit. It was felt that information could pass across the cut line more easily with the second of these procedures.

Description of cases

Flows of Reynolds numbers of 100 and 200 with a Mach number of 0.1 were attempted. Time steps from 0.005 to 0.02 were tried. The finest grid generated was 219 $\times$ 64 with 82 points on the cylinder surface. It extended 15 diameters upstream and across the flow, and 20 diameters downstream.

Observations

The solution evolved into a nearly symmetric steady-like flow with the recirculation region behind the cylinder appearing much like steady flow. Following this time, the separated region evolved into an unsymmetric pattern, which seemed to cross the cut line in a smooth fashion. The lift and drag coefficients tended to be fairly constant once the flow became symmetric, and varied slowly in the early stages of the unsymmetric flow. As more time passed, the stream lines became unrealistic, showing that the flow upstream of the cylinder had large vertical components. At this point lift and drag began to oscillate sporadically. The average frequency of these oscillations was much larger than that of the correct vortex shedding. Some time after this point, the solution diverged and the scheme failed catastrophically.

REFERENCES

Achenbach, E. 1968. "Distribution of local pressure and skin friction around a circular cylinder in cross-flow up to $Re = 5 \times 10^6$." *Journal of Fluid Mechanics*, **34**, 625-639.

Acrivos, A., D. D. Snowden, A. S. Grove, and E. E. Petersen. 1965. "The steady separated flow past a circular cylinder at large Reynolds numbers." *Journal of Fluid Mechanics*, **21**, part 4, 737-760.

Acrivos, A., L. G. Leal, D. D. Snowden, and F. Pan. 1968. "Further experiments on steady separated flows past bluff objects." *Journal of Fluid Mechanics*, **34**, part 1, 25-48.

Anderson, D. A., J. C. Tannehill, and R. H. Pletcher. 1984. *Computational fluid mechanics.* Hemisphere Publishing Corporation, New York. 599 pp.

Beam, R., and R. Warming. 1978. "An implicit factored scheme for the compressible Navier-Stokes equations." *AIAA Journal* **16**, 393-401.

Bentson, B., and G. Vradis. 1987. "A two-stage pressure correction technique for the incompressible Navier-Stokes equations." AIAA Paper 87-0545.

Borthwick, A. 1986. "Comparison between two finite-difference schemes for computing the flow around a cylinder." *International Journal for Numerical Methods in Fluids*, **6**, 275-290.

Bouard, R., and M. Coutanceau. 1980. "The early stage of development of the wake behind an impulsively started cylinder for $40 < Re < 10^4$." *Journal of Fluid Mechanics*, **101**, part 3, 583-607.

Brown, J. L. 1983. "Parabolized Navier-Stokes solutions of separation and trailing edge flows." NASA TM 84378.

Cebeci, T., and P. Bradshaw. 1984. *Physical and computational aspects of convective heat transfer.* Springer-Verlag, New York. 487 pp.

Chamberlain, R. R. 1987. "Unsteady flow phenomena in the near wake of a circular cylinder." AIAA Paper 87-0371.

Chen, K. H., and R. H. Pletcher. 1990. "A primitive variable strongly implicit calculation procedure for viscous flows at all speeds." AIAA Paper 90-1521.

Chilukuri, R., and R. H. Pletcher. 1980. "Numerical solution to the partially parabolized Navier-Stokes equations for developing flow in a channel." *Numerical Heat Transfer*, **3**, 169-188.

Chun, W., and R. F. Boehm. 1989. "Calculation of forced flow and heat transfer around a cylinder in crossflow." *Numerical Heat Transfer*, **15**, 101-122.

Churchill, S. W., and M. Bernstein. 1977. "A correlating equation for forced convection from gases and liquids to a circular cylinder in cross-flow." *Transactions of the ASME, Journal of Heat Transfer, Ser. C*, **99**, part 2, 300-306.

Coutanceau, M., and R. Bouard. 1977. "Experimental determination of the main features of the viscous flow in the wake of a circular cylinder in uniform translation. Part 1. Steady flow." *Journal of Fluid Mechanics*, **79**, part 2, 231-256.

Dennis, C. R., and G. Z. Chang. 1970. "Numerical solutions for steady flow past a circular cylinder at Reynolds numbers up to 100." *Journal of Fluid Mechanics*, **42**, 471-489.

Dimopoulos, H. G., and T. J. Hanratty. 1968. "Velocity gradients at the wall for flow around a cylinder for Reynolds numbers between 60 and 360." *Journal of Fluid Mechanics*, **33**, part 2, 303-319.

Eckert, E. R. G., and E. Soehngen. 1952. "Distribution of heat-transfer coefficients around circular cylinders in crossflow at Reynolds numbers from 20 to 500." *Transactions of the ASME*, **74**, 343-347.

Fornberg, B. 1980. "A numerical study of steady viscous flow past a circular cylinder." *Journal of Fluid Mechanics*, **98**, part 4, 819-855.

Frössling, N. 1940. "Verdunstung, wärmeüberganges und geschwindigkeitsverteilung bei zweidimensionaler und rotationasimmetrischer grenzschichtströmung. *Lunds Universität Arssk. N.F. Avd.* **2**, 36(4), 25-35.

Gosman, A. D., and W. M. Pun. 1973. "Lecture notes for course entitled calculation of recirculating flows." Imperial College Report HTS/74/2.

Hall, M. G. 1968. "The boundary layer over an impulsively started flat plate." *Proceedings of the Royal Society*, A, **310**, 401-414.

Himansu, A., and S. G. Rubin. 1988. "Multigrid acceleration of a relaxation procedure for the RNS equations." *AIAA Journal*, **26**, No. 9. 1044-1051.

Hindman, R. G. 1982. "Generalized coordinate forms of governing fluid equations and associated geometrically induced errors." *AIAA Journal*, **20**, No. 10. 1359-1367.

Karniadakis, G. E., and G. S. Triantafyllou. 1989. "Frequency selection and asymptotic states in laminar wakes." *Journal of Fluid Mechanics*, **199**, 441-469.

Karniadakis, G. E., B. B. Mikic, and A. T. Patera. 1986. "Unsteady heat transfer from a cylinder in cross flow; a direct numerical simulation." Proceedings of the 8th International Heat Transfer Conference, **2**, 429-434.

Krall, K. M., and E. R. G. Eckert. 1973. "Local heat transfer around a cylinder at low Reynolds number." *Journal of Heat Transfer*, **95**, 273-275.

Kwak, D., J. L. C. Chang, S. P. Shanks, and S. R. Chakravarthy. 1984. "An incompressible Navier-Stokes flow solver in three-dimensional curvilinear coordinate system using primitive variables." AIAA Paper 84-0253.

Kwon, O. K. 1987. "Analysis of unsteady two-dimensional boundary layers." Allison Gas Turbine Division Report EDR 12353.

Liu, X., and R. H. Pletcher. (1986). "A coupled marching procedure for the partially parabolized Navier-Stokes equations." *Numerical Heat Transfer*, **10**, 539-555.

Loc, T. P. 1980. "Numerical analysis of unsteady vortices generated by an impulsively started circular cylinder." *Journal of Fluid Mechanics*, **100**, part 1,

111-128.

Loc, T. P., and R. Bouard. 1985. "Numerical solution of the early stage of the unsteady viscous flow around a circular cylinder: a comparison with experimental visualization and measurements." *Journal of Fluid Mechanics*, **160**, 93-117.

Majumdar, S., and W. Rodi. 1985. "Numerical calculations of turbulent flow past circular cylinders." Third Symposium on Numerical and Physical Aspects of Aerodynamic Flows, California.

Moore, J., and J. G. Moore. 1979. "A calculation procedure for three-dimensional viscous, compressible duct flows." *Journal of Fluids Engineering*, **101**, 415-423.

Nieuwstadt, F., and H. B. Keller. 1973. "Viscous flow past circular cylinders." *Computers and Fluids*, **1**, 59-66.

O'Brien, J. E., R. J. Simoneau, J. E. LaGraff, and K. A. Morehouse. 1986. "Unsteady heat transfer and direct comparison to steady-state measurements in a rotor-wake experiment." Proceedings of the International Heat Transfer Conference, 1243-1248.

Paolino, M. A., R. B. Kinney, and E. A. Cerutti. 1986. "Numerical analysis of the unsteady flow and heat transfer to a cylinder in crossflow." *Transactions of the ASME, Journal of Heat Transfer*, **108**, 742-748.

Patankar, S. V., and D. B. Spalding. 1972. "A calculation procedure for heat, mass and momentum transfer in three-dimensional parabolic flows." *International Journal of Heat and Mass Transfer*, **15**, 1787-1806.

Patel, V. A. 1978. "Karman Vortex Street behind a Circular Cylinder by the Series Truncation Method." *Journal of Computational Physics*, **28**, 14-42.

Pouagare, M., and B. Lakshminarayana. 1985. "A space-marching method for incompressible Navier-Stokes Equations." AIAA Paper 85-0170.

Pratråp, V. S., and D. B. Spalding. 1976. "Fluid flow and heat transfer in three dimensional duct flows." *International Journal of Heat and Mass Transfer*, **19**, 1183-1188.

Ramakrishnan, S. V., and S. G. Rubin. 1986. "Numerical solution of unsteady, compressible reduced Navier Stokes equations." AIAA Paper 86-0205.

Ramin, T. H. 1990. "An unsteady boundary-layer method for internal and external flows with applications to fortification schemes." Master's thesis, Iowa State University, Ames, IA.

Reyhner, T. A. and I. Flügge-Lotz. 1968. "The interaction of a shock wave with a laminar boundary layer." *International Journal of Non-Linear Mechanics*, **3**, 173-199.

Rhie, C. M. 1981. "A numerical study of the flow past an isolated airfoil with separation." Ph.D. dissertation, University of Illinois, Champaign, IL.

Rogers, S. E., and D. Kwak. 1988. "An upwind differencing scheme for the time-accurate incompressible Navier-Stokes equations." AIAA Paper 88-2583.

Rosenfeld, M., D. Kwak, and M. Vinokur. 1988. "A solution method for the unsteady and incompressible Navier-Stokes Equations in Generalized Coordinate Systems." AIAA Paper 88-0718.

Rubin, S. G. 1988. "RNS/Euler pressure relaxation and flux vector splitting." *Computers and Fluids*, **16**, No. 4. 485-490.

Rubin, S. G., and D. R. Reddy. 1983. "Analysis of global pressure relaxation for flows with strong interaction and separation." *Computers and Fluids*, **11**, No. 4. 281-306.

Schlichting, H. 1979. *Boundary-layer theory.* (J. Kestin, Translator.) McGraw-Hill Book Company, New York. 817 pp.

Son, J. S., and T. J. Hanratty. 1969. "Numerical solution for the flow around a circular cylinder at Reynolds numbers 40, 200 and 500." *Journal of Fluid Mechanics*, **35**, part 2, 369-386.

Sorenson, R. L. 1980. "A computer program to generate two-dimensional grids about airfoils and other shapes by the use of Poisson's equation." U.S. NASA TM 81198.

Taylor, A. C., W. Ng, and R. W. Walters. 1989. "Upwind relaxation methods for the Navier-Stokes equations." AIAA Paper 89-1954-CP.

TenPas, P. W. 1990. "Solution of the Navier- Stokes equations for subsonic flows using a coupled space-marching method." Ph.D. dissertation, Iowa State University, Ames, IA.

TenPas, P. W., and R. H. Pletcher. 1987. "Solution of the Navier-Stokes equations for subsonic flows using a coupled space-marching method." AIAA Paper 87-1173.

Thom, A. 1933. "The flow past cylinders at low speeds." *Proceedings of the Royal Society*, A, **141**, 651.

Thomas, L. J., and R. W. Walters. 1985. "Upwind relaxation algorithms for the Navier-Stokes equations." AIAA Paper 85-1501.

Thompson, J. F., Z. U. A. Warsi, and C. W. Mastin. 1985. *Numerical grid generation foundations and applications*, Elsevier Science Publishing Company, New York. 483 pp.

Van Leer, B. 1982. "Flux-vector splitting for the Euler equations." *Lecture Notes in Physics*, **170**, 507-512.

Vanfossen, G. J., and R. J. Simoneau. 1985. "Preliminary Results of the relationship between free stream turbulence and stagnation region heat transfer." ASME 85-GT-84

Vigneron, Y. C., J. V. Rakich, and J. C. Tannehill. 1978. "Calculation of supersonic viscous flow over delta wings with sharp subsonic leading edges." AIAA Paper 78-1137.

Visbal, M. R. 1986. "Evaluation of an implicit Navier-Stokes solver for some unsteady separated flows." AIAA Paper 86-1053.

Watkins, C. B. 1975. "Heat transfer in the laminar boundary layers over an impulsively started flat plate." *Journal of Heat Transfer*, **97**, 482-484.

Zukauskas, A. and J. Ziugzda. 1985. *Heat transfer of a cylinder in crossflow.* (E. Bagdonaite, Translator.) Hemisphere Publishing Corporation, Washington. 208 pp.

APPENDIX A. METRICS

The metrics which appear in the governing equations carry the geometric information of the flow. The computational domain is kept simple (Figure 2.1) despite the complexity of the physical domain.

Definitions

The metrics which are used in the governing equations are defined as follows. Since the metrics are normalized by the Jacobian, J, in the code, they are shown in this form.

$$\frac{\xi_x}{J} = \frac{\partial y}{\partial \eta} = y_\eta \qquad \frac{\xi_y}{J} = -\frac{\partial x}{\partial \eta} = -x_\eta \tag{A.1}$$

$$\frac{\eta_x}{J} = -\frac{\partial y}{\partial \xi} = -y_\xi \qquad \frac{\eta_y}{J} = \frac{\partial x}{\partial \xi} = x_\xi \tag{A.2}$$

Where

$$J = \xi_x \eta_y - \xi_y \eta_x = \frac{1}{\frac{\partial y}{\partial \eta}\frac{\partial x}{\partial \xi} - \frac{\partial x}{\partial \eta}\frac{\partial y}{\partial \xi}} = \frac{1}{x_\xi y_\eta - x_\eta y_\xi} \tag{A.3}$$

Pressure Poisson equation solver

The following derivatives of the metrics appear only in the pressure backsweep formulation.

$$\frac{\xi_{xx}}{J} = (\xi_x y_{\xi\eta} + \eta_x y_{\eta\eta}) - (\xi_x^2 (J^{-1})_\xi + \xi_x \eta_x (J^{-1})_\eta) \tag{A.4}$$

$$\frac{\xi_{yy}}{J} = -(\eta_y x_{\eta\eta} + \xi_y x_{\xi\eta}) - (\xi_y \eta_y (J^{-1})_\eta + \xi_y^2 (J^{-1})_\xi) \tag{A.5}$$

$$\frac{\eta_{xx}}{J} = -(\xi_x y_{\xi\xi} + \eta_x y_{\xi\eta}) - (\xi_x \eta_x (J^{-1})_\xi + \eta_x^2 (J^{-1})_\eta) \tag{A.6}$$

$$\frac{\eta_{yy}}{J} = (\eta_y x_{\xi\eta} + \xi_y x_{\xi\xi}) - (\xi_y \eta_y (J^{-1})_\xi + \eta_y^2 (J^{-1})_\eta) \tag{A.7}$$

The Jacobian which shows up on the right-hand-sides of these equations is inverted before taking the required derivative. Or

$$J^{-1} = \frac{1}{J} = x_\xi y_\eta - x_\eta y_\xi \tag{A.8}$$

$$(J^{-1})_\xi = (x_{\xi\xi} y_\eta + x_\xi y_{\xi\eta}) - (x_{\xi\eta} y_\xi + x_\eta y_{\xi\xi}) \tag{A.9}$$

$$(J^{-1})_\eta = (x_{\xi\eta} y_\eta + x_\xi y_{\eta\eta}) - (x_{\eta\eta} y_\xi + x_\eta y_{\xi\eta}) \tag{A.10}$$

These equations involve a mixture of derivatives of ξ and η and also x and y. The first derivatives of ξ and η are have already been defined in terms of x and y. They are calculated and stored in the program. It is a simple matter to numerically calculate the second derivatives of x and y (see below).

Contravarient Velocities

The velocities, U and V, are defined as the components normal to the lines of constant ξ and η respectively. They are:

$$U = \xi_x u + \xi_y v, \quad V = \eta_x u + \eta_y v$$

The grid is stationary in time, so this contributes nothing to these velocities.

Calculation of Metrics Using Finite Differences

The metrics are calculated and stored as one of the first steps in the code. Since the momentum and energy equations are cast in the chain-rule-conservation-law form, there are no particular restrictions on the method of differencing the metrics. The continuity equation was formulated using finite control volumes, so the metrics were calculated directly from the areas of the faces of the control volumes. Therefore, second-order central differences were used for all interior points, as well as boundaries where geometric symmetry is known to exist. First-order one-sided differences were found adequate for non-symmetric boundaries.

The particular finite differences used at an interior point, (i,j) were

$$\frac{\xi_x}{J} \approx \frac{y_{i,j+1} - y_{i,j-1}}{2\Delta\eta} \qquad \frac{\xi_y}{J} \approx -\frac{x_{i,j+1} - x_{i,j-1}}{2\Delta\eta} \tag{A.11}$$

$$\frac{\eta_x}{J} \approx -\frac{y_{i+1,j} - y_{i-1,j}}{2\Delta\xi} \qquad \frac{\eta_y}{J} \approx \frac{x_{i+1,j} - x_{i-1,j}}{2\Delta\xi} \tag{A.12}$$

At boundary points, the affected metrics appear as:

(i, j_{min}) -

$$\frac{\xi_x}{J} \approx \frac{y_{i,j+1} - y_{i,j}}{\Delta\eta} \qquad \frac{\xi_y}{J} \approx -\frac{x_{i,j+1} - x_{i,j}}{\Delta\eta} \tag{A.13}$$

(i, j_{max}) -

$$\frac{\xi_x}{J} \approx \frac{y_{i,j} - y_{i,j-1}}{\Delta\eta} \qquad \frac{\xi_y}{J} \approx -\frac{x_{i,j} - x_{i,j-1}}{\Delta\eta} \tag{A.14}$$

(i_{min}, j) -

$$\frac{\eta_x}{J} \approx -\frac{y_{i+1,j} - y_{i,j}}{\Delta\xi} \qquad \frac{\eta_y}{J} \approx \frac{x_{i+1,j} - x_{i,j}}{\Delta\xi} \tag{A.15}$$

(i_{max}, j) -

$$\frac{\eta_x}{J} \approx -\frac{y_{i,j} - y_{i-1,j}}{\Delta\xi} \qquad \frac{\eta_y}{J} \approx \frac{x_{i,j} - x_{i-1,j}}{\Delta\xi} \tag{A.16}$$

Pressure Poisson equation solver

Second derivatives of x and y appear only in the Poisson equation. Here too, central differences were used at all interior and symmetric-boundary points. These metrics are not needed at solid and free boundaries.

In practice they are calculated as follows:

$$x_{\xi\xi} \approx \frac{x_{i+1,j} - 2x_{i,j} + x_{i-1,j}}{\Delta\xi^2} \tag{A.17}$$

$$x_{\xi\eta} \approx \frac{(x_{i+1,j+1} - x_{i-1,j+1}) - (x_{i+1,j-1} - x_{i-1,j-1})}{4\Delta\xi\eta} \tag{A.18}$$

$$x_{\eta\eta} \approx \frac{x_{i,j+1} - 2x_{i,j} + x_{i,j-1}}{\Delta\eta^2} \tag{A.19}$$

$$y_{\xi\xi} \approx \frac{y_{i+1,j} - 2y_{i,j} + y_{i-1,j}}{\Delta\xi^2} \tag{A.20}$$

$$y_{\xi\eta} \approx \frac{(y_{i+1,j+1} - y_{i-1,j+1}) - (y_{i+1,j-1} - y_{i-1,j-1})}{4\Delta\xi\eta} \tag{A.21}$$

$$y_{\eta\eta} \approx \frac{y_{i,j+1} - 2y_{i,j} + y_{i,j-1}}{\Delta\eta^2} \tag{A.22}$$

APPENDIX B. SIMPLE TRANSFORMATIONS FOR GRID GENERATION

For the case of the semi-infinite flat plate, an H-grid was deemed most appropriate. For the best resolution, grids should be fine in regions where high gradients occur. For this reason, it was felt that a uniformly spaced grid would be inefficient since it would be as fine everywhere as the finest required. Therefore, grid packing schemes were employed in both the x and y directions. The transformations are found in Anderson et al. (1984) and are repeated here for completeness.

Transformation 1

A transformation which packs points close to a body surface — in this case the flat plate (see Figure B.1) — is as follows:

$$\xi = x, \quad \eta = 1 - \frac{\ln\left[\frac{\beta+1-\frac{y}{h}}{\beta-1+\frac{y}{h}}\right]}{\ln\left[\frac{\beta+1}{\beta-1}\right]} \tag{B.1}$$

Here, h is shown in Figure B.1, and β is the stretching (or packing) parameter such that $1 < \beta < \infty$. As β approaches 1, more points are clustered near $y = 0$.

The metrics for this transformation are

$$\xi_x = 1, \quad \eta_x = 0 \tag{B.2}$$

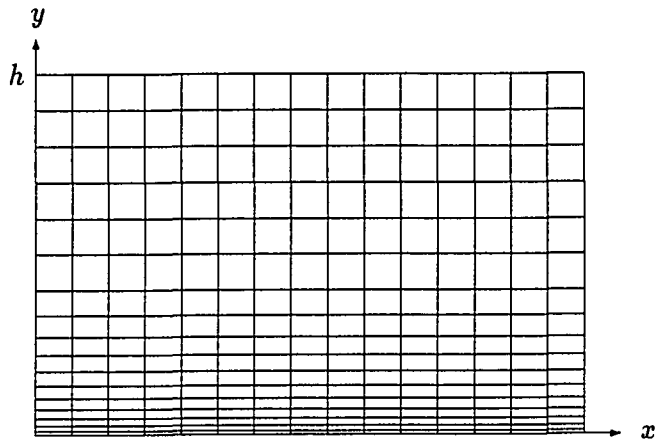

Figure B.1: Grid clustering used for the flat plate case

$$\xi_y = 0, \quad \eta_y = \frac{2\beta}{h\left[\beta^2 - \left(1 - \frac{y}{h}\right)^2\right] \ln\left(\frac{\beta+1}{\beta-1}\right)} \tag{B.3}$$

The inverse of Equations B.1 are found as

$$x = \xi, \quad y = h\frac{(\beta+1) - (\beta-1)\left[\frac{\beta+1}{\beta-1}\right]^{1-\eta}}{\left[\frac{\beta+1}{\beta-1}\right]^{1-\eta} + 1} \tag{B.4}$$

Transformation 2

The second transformation used clusters points in the region of the leading edge (see Figure B.2). It is given by

$$\xi = B + \frac{1}{\tau}\sinh^{-1}\left[\left(\frac{x}{x_c} - 1\right)\sinh(\tau B)\right], \quad \eta = y \tag{B.5}$$

Where

$$B = \frac{1}{2\tau} \ln \left[\frac{1 + (e^{\tau} - 1)\frac{x_c}{L}}{1 + (e^{-\tau} - 1)\frac{x_c}{L}} \right] \tag{B.6}$$

Here, L is shown in Figure B.2, and τ is the stretching (or packing) parameter such that $0 < \tau < \infty$. As τ approaches ∞, more points are clustered near $x = x_c$.

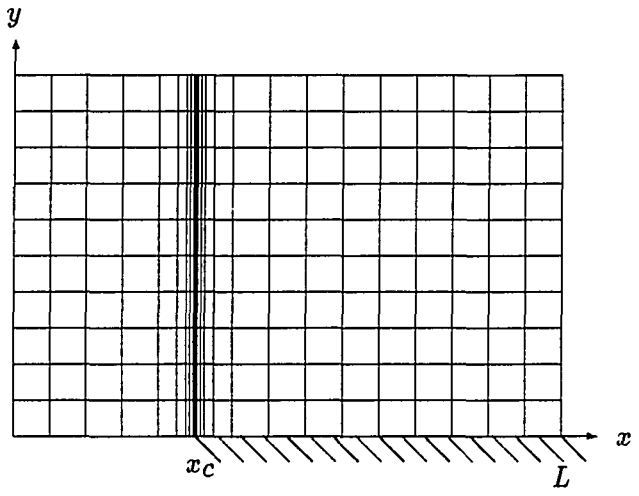

Figure B.2: Grid clustering of points near the leading edge of the flat plate

For this transformation, the metric terms appear as

$$\xi_x = \frac{\sinh(B\tau)}{\tau x_c \sqrt{1 + \left(\frac{x}{x_c} - 1\right)^2 \sinh^2(B\tau)}}, \quad \eta_x = 0 \tag{B.7}$$

$$\xi_y = 0, \quad \eta_y = 1 \tag{B.8}$$

The inverse transformation of Equations B.5 are as follows

$$x = x_c \left[1 + \frac{\sinh[\tau(\xi - B)]}{\sinh(B\tau)} \right], \quad y = \eta \tag{B.9}$$

APPENDIX C. LINEARIZATION OF THE FLUX AND TEMPORAL TERMS

The solution procedure outlined in this work ultimately solves a set of linear equations at each marching station using Gauss elimination. The nonlinear flux and temporal terms must be linearized to conform to this method. Newton linearization was utilized to accomplish this.

The linearized coefficient values were computed iteratively on at each station until sufficient convergence had been achieved. Usually, the rate of convergence was rapid, requiring only 1 or 2 iterations.

The derivation of the linearized coefficients is as follows. The values of the primitive variables at the newest sub-iteration level (within a given time step) can be represented by their values at the previous sub-iteration plus an incremental change:

$$u = \hat{u} + \Delta u, \quad v = \hat{v} + \Delta v, \quad p = \hat{p} + \Delta p, \quad S = \hat{S} + \Delta S \tag{C.1}$$

Thus the nonlinear terms, f, can be represented by a truncated Taylor series expanded about the value at the known state point (the previous iteration level):

$$f(u, v, p, S) \approx f(\hat{u}, \hat{v}, \hat{p}, \hat{S}) + \Delta f \tag{C.2}$$

where

$$\Delta f = f_u \Delta u + f_v \Delta v + f_p \Delta p + f_S \Delta S \tag{C.3}$$

and the changes in the primitive variables can be evaluated using Equation C.1. The partial derivatives (denoted above using subscripts) are evaluated at the known state.

Equation C.2 is a linear function of the variables at the new time level. This is more easily seen by rewriting it as

$$f(u,v,p,S) \approx f_u u + f_v v + f_p p + f_S S + C \tag{C.4}$$

where

$$C = f(\hat{u},\hat{v},\hat{p},\hat{S}) - (f_u \hat{u} + f_v \hat{v} + f_p \hat{p} + f_S \hat{S}) \tag{C.5}$$

This procedure was followed to linearize all of the nonlinear terms found in the equations. Exceptions include:

1. The temperature was lagged from the previous iteration level in the coefficients for the momentum and continuity equations

2. The density was lagged in the temporal terms, $c_p \rho u S$ and $c_p \rho v S$, in the energy equation

3. The temperature was lagged in the temporal terms involving kinetic energy in the energy equation

4. The dissipation terms in the energy equation were treated explicitly

The following table lists the coefficients used in this study.

Table C.1: Coefficients resulting from the Newton linearization

Flux (f)	f_u	f_v	f_p	f_S	C
ρu	$\hat{\rho}$	0	$\frac{\hat{u}}{R\hat{T}}$	0	$-\hat{\rho}\hat{u}$
ρv	0	$\hat{\rho}$	$\frac{\hat{v}}{R\hat{T}}$	0	$-\hat{\rho}\hat{v}$
ρu^2	$2\hat{\rho}\hat{u}$	0	$\frac{\hat{u}^2}{R\hat{T}}$	0	$-2\hat{\rho}\hat{u}^2$
ρuv	$\hat{\rho}\hat{v}$	$\hat{\rho}\hat{u}$	$\frac{\hat{u}\hat{v}}{R\hat{T}}$	0	$-2\hat{\rho}\hat{u}\hat{v}$
ρv^2	0	$2\hat{\rho}\hat{v}$	$\frac{\hat{v}^2}{R\hat{T}}$	0	$-2\hat{\rho}\hat{v}^2$
ρuT	$\hat{\rho}\hat{T}$	0	0	$\hat{\rho}\hat{u}(T_r - T_{surf})$	$-\hat{\rho}\hat{u}\hat{T} + \hat{\rho}\hat{u}T_{surf}$
ρvT	0	$\hat{\rho}\hat{T}$	0	$\hat{\rho}\hat{v}(T_r - T_{surf})$	$-\hat{\rho}\hat{v}\hat{T} + \hat{\rho}\hat{v}T_{surf}$
ρu^3	$3\hat{\rho}\hat{u}^2$	0	$\frac{\hat{u}^3}{R\hat{T}}$	0	$-3\hat{\rho}\hat{u}^3$
$\rho u^2 v$	$2\hat{\rho}\hat{u}\hat{v}$	$\hat{\rho}\hat{u}^2$	$\frac{\hat{u}^2\hat{v}}{R\hat{T}}$	0	$-3\hat{\rho}\hat{u}^2\hat{v}$
ρuv^2	$\hat{\rho}\hat{v}^2$	$2\hat{\rho}\hat{u}\hat{v}$	$\frac{\hat{u}\hat{v}^2}{R\hat{T}}$	0	$-3\hat{\rho}\hat{u}\hat{v}^2$
ρv^3	0	$3\hat{\rho}\hat{v}^2$	$\frac{\hat{v}^3}{R\hat{T}}$	0	$-3\hat{\rho}\hat{v}^3$

APPENDIX D. DIFFUSION OF MOMENTUM TERMS

This appendix deals with the diffusion terms, as found in the momentum equations. These terms contain viscosity-metric products within the derivatives. The product-rule is applied, which results is derivatives of metrics and second derivatives of velocities.

The x-momentum equation viscous stress terms are:

$$-\xi_x(\tau_{xx})_\xi - \xi_y(\tau_{xy})_\xi - \eta_x(\tau_{xx})_\eta - \eta_y(\tau_{xy})_\eta \tag{D.1}$$

Each of these terms, in the order shown above, is expanded as follows.

$$\begin{aligned}
-\xi_x(\tau_{xx})_\xi &= -\left[\frac{2}{3}\mu[2(u_\xi\xi_x + u_\eta\eta_x) - (v_\xi\xi_y + v_\eta\eta_y)]\right]_\xi \xi_x \\
&= -\left[\frac{4}{3}\mu\xi_x u_{\xi\xi} + \frac{4}{3}\mu\eta_x u_{\xi\eta} - \frac{2}{3}\mu\xi_y v_{\xi\xi} - \frac{2}{3}\mu\eta_y v_{\xi\eta}\right. \\
&+ \left.\frac{4}{3}(\mu\xi_x)_\xi u_\xi + \frac{4}{3}(\mu\eta_x)_\xi u_\eta - \frac{2}{3}(\mu\xi_y)_\xi v_\xi - \frac{2}{3}(\mu\eta_y)_\xi v_\eta\right]\xi_x
\end{aligned}$$

$$\begin{aligned}
-\xi_y(\tau_{xy})_\xi &= -\left[\mu[(u_\xi\xi_y + u_\eta\eta_y) + (v_\xi\xi_x + v_\eta\eta_x)]\right]_\xi \xi_y \\
&= -\left[\mu\xi_y u_{\xi\xi} + \mu\eta_y u_{\xi\eta} + \mu\xi_x v_{\xi\xi} + \mu\eta_x v_{\xi\eta}\right. \\
&+ \left.(\mu\xi_y)_\xi u_\xi + (\mu\eta_y)_\xi u_\eta + (\mu\xi_x)_\xi v_\xi + (\mu\eta_x)_\xi v_\eta\right]\xi_y
\end{aligned}$$

$$-\eta_x(\tau_{xx})_\xi = -\left[\frac{2}{3}\mu[2(u_\xi\xi_x + u_\eta\eta_x) - (v_\xi\xi_y + v_\eta\eta_y)]\right]_\eta \eta_x$$

$$
\begin{aligned}
&= -\Big[\frac{4}{3}\mu\xi_x u_{\xi\eta} + \frac{4}{3}\mu\eta_x u_{\eta\eta} - \frac{2}{3}\mu\xi_y v_{\xi\eta} - \frac{2}{3}\mu\eta_y v_{\eta\eta} \\
&+ \frac{4}{3}(\mu\xi_x)_\eta u_\xi + \frac{4}{3}(\mu\eta_x)_\eta u_\eta - \frac{2}{3}(\mu\xi_y)_\eta v_\xi - \frac{2}{3}(\mu\eta_y)_\eta v_\eta\Big]\eta_x
\end{aligned}
$$

$$
\begin{aligned}
-\eta_y(\tau_{xy})_\eta &= -\Big[\mu[(u_\xi\xi_y + u_\eta\eta_y) + (v_\xi\xi_x + v_\eta\eta_x)]\Big]_\eta \eta_y \\
&= -\Big[\mu\xi_y u_{\xi\eta} + \mu\eta_y u_{\eta\eta} + \mu\xi_x v_{\xi\eta} + \mu\eta_x v_{\eta\eta} \\
&+ (\mu\xi_y)_\eta u_\xi + (\mu\eta_y)_\eta u_\eta + (\mu\xi_x)_\eta v_\xi + (\mu\eta_x)_\eta v_\eta\Big]\eta_y
\end{aligned}
$$

The corresponding terms from the y-momentum equation are:

$$
-\xi_x(\tau_{xy})_\xi - \xi_y(\tau_{yy})_\xi - \eta_x(\tau_{xy})_\eta - \eta_y(\tau_{yy})_\eta \tag{D.2}
$$

Again, expanding yields the following.

$$
\begin{aligned}
-\xi_x(\tau_{xy})_\xi &= -\Big[\mu[(u_\xi\xi_y + u_\eta\eta_y) + (v_\xi\xi_x + v_\eta\eta_x)]\Big]_\xi \xi_x \\
&= -\Big[\mu\xi_y u_{\xi\xi} + \mu\eta_y u_{\xi\eta} + \mu\xi_x v_{\xi\xi} + \mu\eta_x v_{\xi\eta} \\
&+ (\mu\xi_y)_\xi u_\xi + (\mu\eta_y)_\xi u_\eta + (\mu\xi_x)_\xi v_\xi + (\mu\eta_x)_\xi v_\eta\Big]\xi_x
\end{aligned}
$$

$$
\begin{aligned}
-\xi_y(\tau_{yy})_\xi &= -\Big[\frac{2}{3}\mu[-(u_\xi\xi_x + u_\eta\eta_x) + 2(v_\xi\xi_y + v_\eta\eta_y)]\Big]_\xi \xi_y \\
&= -\Big[-\frac{2}{3}\mu\xi_x u_{\xi\xi} - \frac{2}{3}\mu\eta_x u_{\xi\eta} + \frac{4}{3}\mu\xi_y v_{\xi\xi} + \frac{4}{3}\mu\eta_y v_{\xi\eta} \\
&- \frac{2}{3}(\mu\xi_x)_\xi u_\xi - \frac{2}{3}(\mu\eta_x)_\xi u_\eta + \frac{4}{3}(\mu\xi_y)_\xi v_\xi + \frac{4}{3}(\mu\eta_y)_\xi v_\eta\Big]\xi_y
\end{aligned}
$$

$$
\begin{aligned}
-\eta_x(\tau_{xy})_\eta &= -\Big[\mu[(u_\xi\xi_y + u_\eta\eta_y) + (v_\xi\xi_x + v_\eta\eta_x)]\Big]_\eta \eta_y \\
&= -\Big[\mu\xi_y u_{\xi\eta} + \mu\eta_y u_{\eta\eta} + \mu\xi_x v_{\xi\eta} + \mu\eta_x v_{\eta\eta} \\
&+ (\mu\xi_y)_\eta u_\xi + (\mu\eta_y)_\eta u_\eta + (\mu\xi_x)_\eta v_\xi + (\mu\eta_x)_\eta v_\eta\Big]\eta_x
\end{aligned}
$$

$$
\begin{aligned}
-\eta_y(\tau_{yy})_\eta &= -\left[\frac{2}{3}\mu[2(u_\xi\xi_x + u_\eta\eta_x) - (v_\xi\xi_y + v_\eta\eta_y)]\right]_\eta \eta_y \\
&= -\left[-\frac{2}{3}\mu\xi_x u_{\xi\eta} - \frac{2}{3}\mu\eta_x u_{\eta\eta} + \frac{4}{3}\mu\xi_y v_{\xi\eta} + \frac{4}{3}\mu\eta_y v_{\eta\eta}\right. \\
&- \left.\frac{2}{3}(\mu\xi_x)_\eta u_\xi - \frac{2}{3}(\mu\eta_x)_\eta u_\eta + \frac{4}{3}(\mu\xi_y)_\eta v_\xi + \frac{4}{3}(\mu\eta_y)_\eta v_\eta\right]\eta_y
\end{aligned}
$$

Despite the similarities between the diffusion terms in the momentum and energy equations, the product-rule for differentiation was not applied to the energy diffusion terms before differencing. The differencing of the momentum equations was carried out by TenPas (1990) while the differencing of the energy equation was done by the author. For the present work, it was felt that differencing the diffusion terms without the extra step of the product-rule was consistent with the differencing of the other terms. Since the viscous terms in the momentum equation were already differenced, and no apparent problems arose due to the form of this difference, they were not changed. The diffusion terms tend to be quite stable, and it is believed that accurate results are obtainable using either form.